KWAME NKRUMAH UNIVERSITY OF SCIENCE AND TECHNOLOGY, KUMASI

COLLEGE OF SCIENCE

FACULTY OF PHYSICAL AND COMPUTATIONAL SCIENCES

DEPARTMENT OF CHEMISTRY

TRANSITION METAL OXIDES AS ACCELERANTS FOR DIRECT INTERSPECIES ELECTRON TRANSFER IN SYNTROPHIC-METHANOGENIC ASSOCIATIONS: A DFT HSE STUDY

A thesis submitted to the Department of Chemistry, Kwame Nkrumah University of Science and Technology, Kumasi, in partial fulfilment of the requirements for the award of an M.Phil. degree in Physical Chemistry

BY

AMA KONADU AGYEMANG

SUPERVISORS:

DR. CAROLINE R. KWAWU

DR. FRANCIS OPOKU

PROF. JOHANNES AWUDZA

DECLARATION

I hereby declare that this thesis is my work towards the M.Phil. and that, to the best of my knowledge, it contains no material that has been accepted for the award of any other degree in any educational institution nor previously published or written by another person, except where due reference is made in the text of the thesis.

Ama Konadu Agyemang	……	…….
(Candidate)	Signature	Date
Dr. Caroline R. Kwawu	……	…….
(Supervisor)	Signature	Date
Dr. Francis Opoku	……	…….
(Supervisor)	Signature	Date
Prof. Johannes Awudza	….……...	….……
(Supervisor)	Signature	Date
Prof. Godfred Darko	……..	……
(Head of Department)	Signature	Date

DEDICATION

This research work is dedicated to my mother, Mrs Patricia Enstua-Mensah, for the sacrifices, the love, and the guidance she has given me.

ACKNOWLEDGEMENT

I am immensely grateful to Jesus Christ for his abundant grace and mercies towards me for this entire project. Completing this thesis would not have been possible without his incredible love, guidance, and protection.

In making this project meaningful, I would like to acknowledge my supervisors, Dr Caroline R. Kwawu, Dr Francis Opoku, Prof. Richard Tia (of blessed memory), and Prof. Johannes Awudza, for their patience, guidance, and suggestions.

Additionally, I acknowledge Prof. Nelson Dzade of Penn State University and Prof. Evans Adei of the Theoretical and Computational Chemistry Centre, who contributed their insight to the development of this work. I am also grateful to Dr Elliot Menkah, Dr Cecil Botchway and everyone who contributed to this work. I am hugely indebted to the Brew Hammond Energy Center, headed by Prof. Francis Kemausuor and Dr Mizpah Rockson, for their guidance and funding of this work. The project was funded by the Ministry of Education and Research (BMBF) in Germany and with the supervision of the Ministry of Environment, Science, Technology, and Innovation (MESTI).

ABSTRACT

In biogas production, ineffective charge shuttling in the bio-digestion process leads to the accumulation of fatty acids over methane. Research into the understanding and engineering of the direct interspecies electron transfer (DIET) based syntrophic process has emerged to improve methanogenesis kinetics in anaerobic digestion by reducing fatty acid accumulation. Although oxides help in this regard, they have been identified to play either a catalytic or inhibitory role in biogas production. Previous experimental investigations show that transition metal oxides like tungsten oxide and hafnium oxide accelerate DIET, whiles zinc oxide and copper oxide inhibit DIET and, thus, methanation. The density functional theory (DFT) method at the Heyd-Scuseria-Ernzerhof (HSE) hybrid exchange-correlation functional level of theory has been employed in this work to elucidate the microscopic phenomena and to understand the role of the metal oxide chemistry on the initial mechanisms of the DIET. The electronic properties, the quantity of charge shuttled from the acetogen into the methanogen at transition metal oxide surfaces, and the effect of conductivity of the cost-effective transition metal oxides (i.e., ZnO, CuO, HfO_2 and WO_2) on the anaerobic digestion process have been studied. The results show that an enhanced DIET process can be ascribed to the superior electron transmission ability of HfO_2 and WO_2 in anaerobic digestion systems. It is also found that the Meso-diaminopimelic acid, N-acetylglucosamine and N-acetylmuramic acid form more stable complexes in all cases.

TABLE OF CONTENTS

LIST OF TABLES

LIST OF FIGURES

CHAPTER ONE

1.0 INTRODUCTION

1.1 Background

As the world hurtles toward its urban future, the amount of municipal solid waste (MSW), an unavoidable byproduct of an urban lifestyle, is growing even faster than the rate of urbanisation (Chen, 2018). The biggest global challenge in this regard remains the issue of the constant generation of MSW (Singh *et al.*, 2011), their improper processing (Montejo *et al.*, 2010), and the unsanitary disposal of MSW (Tenodi *et al.*, 2020). Due to the enormous environmental and economic impacts of poorly managed MSW, efforts are being made to manage and curb the problem. Waste-to-energy technologies are among the notable municipal solid waste management processes practised. These technologies include pyrolysis of waste (Velghe *et al.*, 2011a), incineration (Silva *et al.*, 2020), gasification (Munir *et al.*, 2019), and anaerobic digestion of the organic fraction of MSW (Lei *et al.*, 2016). In pyrolysis, organic material is thermochemically degraded in an anoxic atmosphere into non-condensable gases, condensable liquids, and solid residue byproducts called biochar or charcoal (Buah *et al.*, 2007; Velghe *et al.*, 2011b). Incineration and gasification involve using MSW as a fuel source: it entails burning it in high volumes of air to generate carbon dioxide and heat. In most modern waste-to-energy plants that employ incineration, these hot gases are used to power steam turbines that generate electricity. Lastly, gasification is collectively defined as a chemical process that involves heating waste in a low-oxygen environment until it disintegrates into smaller units of bulky macromolecular components (Arena, 2012). Amongst these techniques, organic municipal solid waste's anaerobic digestion (AD) has generated much more attention in sustainable municipal waste management due to its numerous advantages (Jain *et al.*, 2015). This process can indirectly lead to a significant reduction in the emission of greenhouse gases through the

production of renewable natural gas, requiring no energy inputs. Other byproducts are raw materials for manufacturing fertilisers and other soil-enriching additives (Nazerifard *et al.*, 2021). Despite the exceptionally positive features of AD, low conversion rates of volatile fatty acids to acetate, low quantities of biogas, and an unstable digestion environment hinder the maximum product yield. These drawbacks can be observed in converting some complex organic compounds into methane via AD. These steps are hydrolysis, acidogenesis, acetogenesis, and methanogenesis, as shown in **Figure 1.1**. The reactions for each step are performed by four major functionally different microbial groups: hydrolytic bacteria (Zheng *et al.*, 2021), acidogenic bacteria (Singh and Harvey, 2010), syntrophic acetogenic bacteria (Manyi-Loh *et al.*, 2013), and methanogenic archaea (Gottlieb *et al.*, 2016), respectively. First, the solid organic waste, composed of macromolecular organic compounds (De Leeuw, 1993) formed from degraded organic material, is selectively fragmented by hydrolytic bacteria into monomers of carbohydrates, amino, and fatty acids.

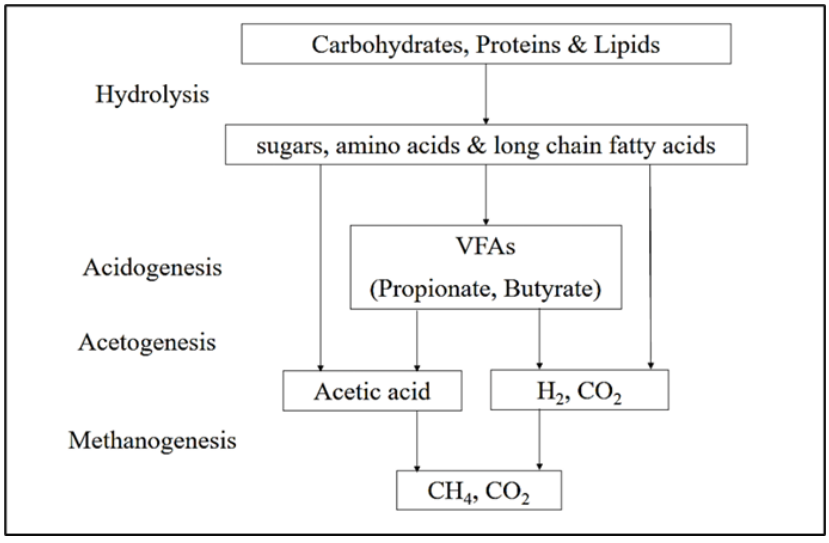

Figure 1.1: Process flow of the degradation of organic material through anaerobic

Acidogenic bacteria ferment these hydrolytic products into organic acids and alcohols, including volatile fatty acids and ethanol, with hydrogen produced as a byproduct (Ren *et al.*, 2007). The Stickland reaction is a prime illustration of an acidogenic process. This reaction involves a pair of amino acids broken down to form NH_3, CO_2 and acetate, as illustrated below.

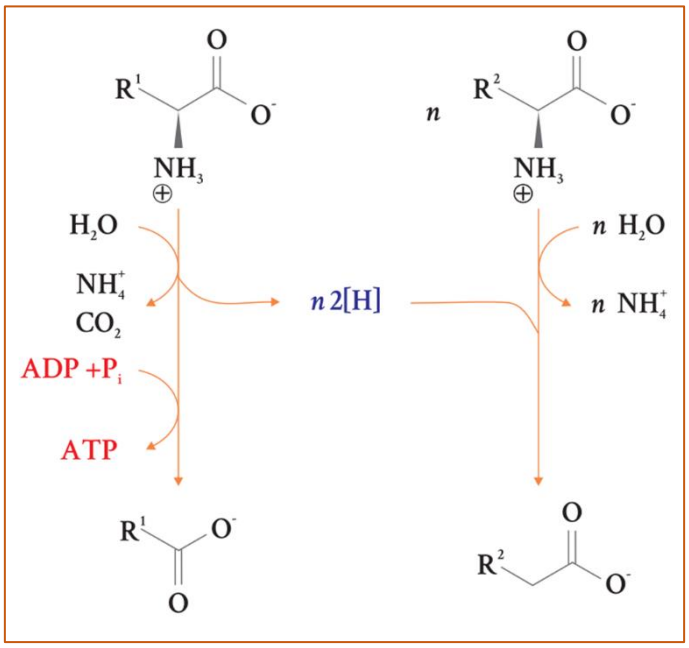

Figure 1.2 Stickland reaction for forming NH_3, CO_2 and acetate from amino acids.

Acetogenic bacteria oxidise more-reduced intermediates, such as lactate, ethanol, propionate, and butyrate, to acetate. Acetate is then converted into CO_2 and CH_4 by methanogens.

The acetate and methane formation steps should constitute a syntrophic relationship. The need for such a relationship can be attributed to acetogenesis being an endergonic reaction. Thus, hydrogen, an acetogenic product, is effectively removed by hydrogen consumers, especially methanogens, before the reaction occurs. It has been established that high hydrogen partial pressure inhibits the regeneration of the cytoplasmic pool of oxidised coenzymes in acetogenic bacteria (Agne *et al.*, 2022).

Interspecies electron transfer is the key to the stability of syntrophic methanogenesis as it determines whether the organic matter degradation and methanogenesis process can be carried out efficiently and orderly. Therefore, an in-depth understanding of interspecies electron transfer during AD contributes to the rational use of energy. There are three pathways for interspecies electron transfer: interspecies hydrogen transfer (Feng *et al.*, 2020), interspecies formate transfer (Rotaru et al., 2014), and direct interspecies electron transfer (DIET) (Rotaru et al., 2014)

1.1.1 Interspecies Electron Transfer (Indirect)

Indirect interspecies electron transfer is the type of electron transfer that requires mediators like H_2 and formate that facilitate the electron transfer. Generally, H_2 is a vital substrate to produce CH_4 by acting as an electron shuttle to transfer electrons from volatile fatty acids or alcohol to CO_2 (Zhang and Zang, 2019). This process is termed interspecies hydrogen transfer (IHT) and is the most standard form of electron transfer in anaerobic digestion. The conjugate bases of propionic acid and butyric acid serve as the primary sources of H_2, and their degradation is thermodynamically feasible only at low partial pressures of H_2, as shown below.

$$CH_3CH_2COO^- + 3H_2O \rightarrow CH_3COO^- + HCO_3^- + H^+ + 3H_2,\ \Delta G = +76.1\ kJ/mol$$
$$CH_3CH_2CH_2COO^- + 2H_2O \rightarrow 2CH_3COO^- + H^+ + 2H_2,\ \Delta G = +48.1\ kJ/mol$$

These thermodynamic limitations encountered with using H_2 as an electron shuttle inhibit anaerobic digestion. Since these fall under syntrophic metabolism, the methanogens slow down the rate of utilising H_2, and the acetogens will also slow the use of propionate and butyrate (Cruz et al., 2014). As a result of the buildup of volatile fatty acids, the anaerobic digestion system fails. The alternative to hydrogen is using formate, which also presents the same limitations.

$$CH_3CH_2COO^- + 2H_2O + 2CO_2 \rightarrow CH_3COO^- + 3HCOO^- + 3H^+,\ \Delta G = +65.3\ kJ/mol$$

$$CH_3CH_2CH_2COO^- + 2H_2O + 2CO_2 \rightarrow 2CH_3COO^- + 3HCOO^- + 3H^+,\ \Delta G = +38.5\ kJ/mol$$

Aside from the above reactions, electron transfer has been observed to occur via extracellular compounds of the methanogens, like humic acids present in humus (Hernandez and Newman, 2001; Hobbie *et al.*, 2012a). Insoluble substances do not permeate the cell membrane of these methanogens and acetogens, unlike soluble electron shuttles that can diffuse in and out of the cell, such as hydrogen or formate molecules. A 2012 study revealed that humus could facilitate the passage of electrons between humic acid-reducing and humic acid-oxidising microorganisms (Hobbie *et al.*, 2012b). The redox-active quinone moieties in humic compounds have been primarily known to exhibit electron-acceptor characteristics. Several microbes, such as the halo-respiring bacterium Desulfitobacterium PCE1, the sulfate-reducing bacterium Desulfovibrio G11, and the methanogenic archaea Methanospirillum hungatei JF1, were observed to reduce humic acids or anthraquinone-2,6-disulphonate (AQDS) (Cervantes *et al.*, 2002; Wu *et al.*, 2011) using hydrogen as an electron donor (Desulfitobacterium dehalogenans and Desulfitobacterium PCE1) (Gerritse *et al.*, 1996). Humus also shows its unique ability to deoxidise as humic acid, for example, acts as a redox mediator in the oxidation of anaerobic substrates coupled with the abiotic reduction of metal oxides like Fe(III) and Mn(IV) (Martinez *et al.*, 2013). However, other microorganisms possess this ability, including Shewanella, Desulfitobacterium, Desulphuromonas, Geospirillum, Wolinella, Geothrix, and the methanogenic archaea Methanopyrus kandleri. Some bacteria of the genus Geobacter have been reported to be quinone-reducing microorganisms using Fe (III) as the terminal electron acceptor.

For many years, H_2 and formate transfer between methanogens and their syntrophic partners were thought to be the most sustainable mechanisms for interspecies electron transfer between methanogens and fermentative bacteria (Wang et al., 2021). Recent discoveries revealed that some bacteria could directly transfer electrons to methanogens instead of interspecies H_2/formate transfer. This unique cell-to-cell electron transfer mechanism allows methane production from the reduced organic compounds to occur more thermodynamically efficiently(Barua and Dhar, 2017). This discovery ultimately provides rapid conversion of organic wastes to methane. This newly discovered electron transfer mechanism between species has been recognised in the literature as DIET (Liu *et al.*, 2012; Wang and Lee, 2021).

1.1.2 Direct Interspecies Electron Transfer

The phenomenon of the acetogens and methanogens transmitting electrons without carriers was first observed in an AD system containing ethanol oxidising fumarate (Baek *et al.*, 2018). This direct transfer between volatile fatty acids oxidising bacteria and methanogens has been noted to reduce CO_2 to CH_4 with lower energy. It has been confirmed in co-cultures of Geobacter metallireducens (Aklujkar *et al.*, 2009) and Methanosaeta (Chen and He, 2015) or Methanosarcina (Conklin *et al.*, 2006). Three types of DIET reactions have been identified: membrane-bound proteins DIET, DIET via conductive Pilli (Kataky and Knowles, 2018) and then DIET via abiotic conductive materials. DIET is considered more energy efficient due to the absence of electron shuttles like H_2 and formate. DIET by membrane-bound electron transport proteins such as OmcZ is a means of electron transfer via direct channels. Research has shown that Prosthecochloris aestaurii (Ha *et al.*, 2017) can accept electrons generated by G. sulfurreducens (Wang et al., 2021), despite the absence of significant tight connections of conductive pili between the two strains, as seen in transmission electron microscopy pictures. The transmission of electrons to the electrodes is carried out by the multiheme outer-surface

cytochrome OmcZ, which was once thought to be related to this kind of DIET. The co-culture of sulfate-reducing bacteria and methanogens archaea revealed a similar physical connection. DIET can also occur when the conductive pili directly transmit electrons between the methanogenic bacteria and acetogens. Conductive pili are protein filaments microorganisms produce for long-range electron transfer under suitable conditions. These pili have been observed in many studies by atomic force microscopy (Touhami *et al.*, 2006), scanning electron microscopy (SEM) (Kraus and Glassman, 1974), scanning tunnelling microscopy (STM) (Thirumurthy *et al.*, 2020) and transmission electron microscopy (TEM) (Gong and Makowski, 1992). Through pili, longer-range electron transfer can occur without a direct contact mechanism to insoluble minerals, solid electrodes, other microorganisms, and electrically conductive biofilm.

DIET between bacteria and methanogenic archaea in anaerobic digestion can accelerate the syntrophic conversion of various reduced organic compounds to methane with lower energy requirements than the other electron transfer pathways. Although DIET-based syntrophy can naturally occur in some anaerobic digesters via conductive pili and membrane-bound proteins, it can be engineered by adding various non-biological conductive materials (Cruz et al., 2017).

1.1.3 Conductive and Semi-conductive Materials such as DIET Accelerants

Numerous studies have established that adding conductive materials like magnetite, granular activated carbon (GAC) (Lee *et al.*, 2020), carbon nanotubes (CNT) (Xia *et al.*, 2019), and biochar to anaerobic reactors (Qiu *et al.*, 2019) enhances the production of methane. Generally, the ability of these materials to enhance methane production has been attributed to some intrinsic properties they exhibit, like their high stability, large surface area, good adsorption capacity and high electric conductivity. Materials like the multiple rolled layers of concentric

graphene nanotubes inside other nanotubes (multi-walled CNT) and single-walled CNTS have been noted to boost general biogas yields 17 times, thereby doubling methane production compared to the control setup (Choi *et al.*, 2014) .

Many of these materials may function as redox mediators in the microbial catalysis of electrophilic groups, such as dyes. The ability of conductive materials to act as direct inter-species electron transfer accelerants were verified in co-cultures of pilA-deficient strains of G. metallireducens with Methanosarcian barkeri (Maeder *et al.*, 2006). The work had shown that these pilA-deficient strains could not convert ethanol to methane unless in the presence of biochar. That notwithstanding, methanogenic co-culture could use 86 % of the electrons released from ethanol oxidation for methane generation (Martins *et al.*, 2018). In a study by Liu and his team, magnetite has been noted to accelerate DIET in Geobacter species without the pilin-associated c-type cytochrome (OmcS) (Liu *et al.*, 2015) initially thought to be necessary for extracellular electron transfer.

1.1.4 Transition Metal Oxides as DIET Accelerants

Like magnetite, other transition metal oxides have been noted to accelerate DIET in syntrophic-methanogenic associations. Reports show that the addition of transition metal oxides like tungsten oxide (WOx) (Yun *et al.*, 2021a), tantalum oxide (TaOx) (Ishihara *et al.*, 2014), hafnium oxide (HfO_2) (Sales *et al.*, 2021) et cetera to anaerobic digesters can increase biogas yield by accelerating DIET. Transition metal compounds, especially transition metal oxides, possess unique Pt-like electronic structures and electrocatalytic properties, which are widely applied in solar cells (Li *et al.*, 2011), supercapacitors (Lin *et al.*, 2014), lithium-ion batteries (Liu *et al.*, 2021), purification systems for wastewater treatment (Shen *et al.*, 2020) and anaerobic digestion (AD) (Fernandez *et al.*, 2022).

In 2017, the Abdelsalam group observed a 95 % increase in biogas yield upon adding magnetite (Fe_3O_4) (Abdelsalam *et al.*, 2017; Liang *et al.*, 2017). These findings have led to exploring other transition metal oxides as accelerants for anaerobic digestion. Notable trends from the literature show that varying crystal structures exhibit different accelerating abilities in anaerobic digestion. For instance, a study by Chen and his coworkers shows that adding 100 mg Ni L–1 Fe_2NiO_4 enhances biogas production by 30 %, while Fe_4NiO_4Zn with the same concentration inhibits AD performance (Chen *et al.*, 2018). According to them, this change could be ascribed to the difference in the crystal structure and the concentration of released metal ions between the two systems. Also, the doping of Zn^{2+} into the Fe_2NiO_4 material could have resulted in the lysis of the microbes, which would inhibit microbial activity and therefore inhibit the A.D. performance (Mahdy *et al.*, 2020). Before this, Mu et al. had shown that the addition of SiO_2 does not correspond with any significant change to the biogas yield, while the addition of ZnO and CuO decreased the yield by 70 % and 30 % respectively (Luna-delRisco *et al.*, 2011a).

Despite the significant amount of literature showing that the type and composition of oxides impact its effect on the syntrophic methanogenesis of biomass waste, there is no existing systematic study into the factors that influence the reactivity of the oxides towards DIET.

1.2 Problem Statement

Transition metal oxides have been widely used to enhance AD performance by accelerating direct interspecies electron transfer in syntrophic-methanogenic associations. However, the composition of the oxides has been seen to either act as inhibitors or accelerants for the methanogenic process. Knowledge of the factors that control the behaviour of the oxide and

the charge shuttling ability of novel materials is vital to improving the DIET and AD. In this regard, the mechanisms of DIET via different transition metal oxides remain unclear.

1.3 Objectives

1) Study the electronic properties and structural/activity descriptors of the bulk and surface structures of some active transition metal oxides, i.e., HfO_2, and WO_2, that could enable them to act as potential accelerants for DIET.
2) Study the electronic properties and structural/activity descriptors of known inhibitors' bulk and surface structures (ZnO, CuO) that contribute to their inhibition potential for DIET.
3) Quantify the charge transfer or shuttling ability of metal oxides from the acetogen bacteria using the basic units of the peptide bonds and glycan chains in the peptidoglycan layer of Pelotomaculum thermopropionicum as a model of the acetogen.

1.4 Justification

The findings from this work will improve the knowledge of DIET reactions and contribute to providing novel abiotic accelerants for AD systems. These findings can also provide a new perspective on microbial extracellular electron transfer and its application in bioremediation, biosensing, electricity generation, waste treatment, et cetera.

CHAPTER TWO

2.0 LITERATURE REVIEW

2.1 Theoretical Background

Computational Chemistry is a tool for investigating molecules' and materials' structure, energetics and dynamics. With the quest to solve relevant chemical problems, computational chemistry is the branch of chemistry where solid-state physics theories and mathematical equations are combined into computer algorithms as reaction simulation packages (Cramer 2004). Since biochemistry and biology are inter-disciplinary fields, it necessitates a collective understanding of statistical, classical, and quantum mechanics (Greeley et al. 2002). Computational chemistry is a supplemental tool that aids in comprehending experiments and, in some situations, can be used in place of them when they are not feasible. Applications for computational chemistry include:

1. When the fleeting nature of transition states makes it difficult for the experiment to examine the mechanistic specifics of a reaction, it is impossible to isolate transition states and study them experimentally (Hoz, 1982).
2. Surface energies are exceedingly challenging to investigate and quantify in an experiment. To study strain in materials, it is possible to easily change and observe parameters like lattice constants through computational calculations without worrying about the issues posed by straining an actual crystal (Gilman, 1960).
3. Computational calculations are sometimes less expensive than an experiment. Suppose the experiment is accurately simulated on computers. In that case, the cost of the chemicals and equipment and the time (again dependent on the experiment) can be significantly minimised (Morris, 1991).
4. They are another option for the validation of some experimental results.

Considering the advancements in algorithmic design and technological innovation in computing hardware, the discipline of computational chemistry is a constantly expanding field. It is not restricted to micro-molecular systems but has become particularly relevant to bigger systems such as surface reactions, bulk or dense materials, and macro-molecular interfaces (VanGessel *et al.*, 2018). The main goal of computational chemistry, a relatively new branch of condensed matter physics, is to identify characteristics such as structural phase transitions, bond lengths, and crystal lattice constants.

Studying materials on an antagonistic scale now heavily relies on computational material science. It is a beneficial tool for catalysis and surface science researchers and is designed to provide information for manufacturing more effective materials with specific applications (Giri and Hopkins, 2020). Utilising computer modelling, specific characteristics of materials, such as flaws, can be duplicated and simulated. Most natural crystalline materials have flaws that can now be simulated by software.

2.2 Computational Chemistry Methods

Computational methods fall into two categories namely, the quantum mechanical based methods and the non quantum mechanical based methods. In force field based methods (non quantum mechanical),

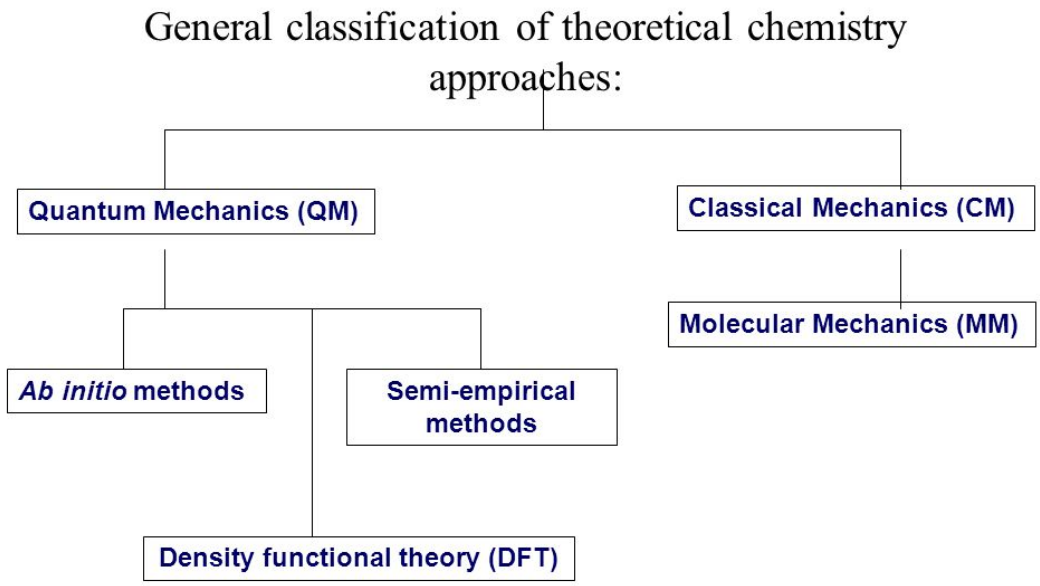

Figure 2.1: Flow chart showing the different branches of computational chemistry

It is assumed that the electronic parts of the atoms can be neglected and thus the molecules are considered as balls with the bonds represented as strings (Giri and Hopkins, 2020). Computational quantum chemistry methods calculate energy and electronic structure, whereas non-quantum chemistry methods only calculate energy and ignore the electronic structure of the system (Van Mourik, 2004).

2.2.1 Electronic Structure Methods

The non-relativistic time-independent Schrödinger equation (Reginatto, 1998) is solved using electronic structure approaches.

$$\hat{\mathrm{H}}\Psi(\{R_A\},\{r_i,\sigma_i\}) = E\Psi(\{R_A\},\{r_i,\sigma_i\}) \qquad (2.1)$$

The many-body wavefunction (Ψ) of an M nuclei system with N electrons is a function of all the spatial coordinates of the nuclei ($\{R_A\}$, A = 1,…, M) and the spatial and spin coordinates of the electrons ({r_i,σ_i }, i=1,…, N). Then, all potential relationships between the nuclei and the electrons are described by the Hamiltonian operator ($\hat{\mathrm{H}}$). The expression is represented by:

$$\hat{\mathrm{H}} = -\sum_{i=1}^{N}\frac{\nabla_i^2}{2} + \sum_{A=1}^{M}\frac{\nabla_A^2}{2M_A} + \sum_{i=1}^{N}\sum_{j>i}^{N}\frac{1}{|r_i - r_j|} + \sum_{i=1}^{N}\sum_{A=1}^{M}\frac{Z_A}{|r_i - R_A|} - \sum_{A=1}^{M}\sum_{B>A}^{M}\frac{Z_A Z_B}{|R_A - R_B|} \qquad (2.2)$$

M_A The equation above represents the nuclei's mass as a percentage of the electron's mass—the atomic number. Z_A stands for the nucleus A. The kinetic energy of the electron and the nuclei are represented by the first two terms in equation 2.2. The Laplacian operators are ∇_i^2 and ∇_A^2 equation 2.1 appears straightforward, but it requires much work to solve, necessitating many approximations to address the many-body problem in existing systems.

The equation's nuclear and electronic components were separated in the early approximations, with the nuclear component being treated as a constant. The Born-Oppenheimer approximation is the name given to this estimate (Combes, 1977). This approximation exists since the electrons travel far more quickly than the nuclei, and the difference is so vast that the nuclei might as well not be moving. In the equation for the nuclei, this implies that the kinetic energy terms are disregarded. The ground state of the electron is immediate. The electronic Hamiltonian ($\hat{\mathrm{H}}_e$) is composed of the terms remaining in equation 2.2.

$$\hat{\mathrm{H}}_e = -\sum_{i=1}^{N}\frac{\nabla_i^2}{2} + \sum_{i=1}^{N}\sum_{j>i}^{N}\frac{1}{|r_i - r_j|} - \sum_{i=1}^{N}\sum_{A=1}^{M}\frac{Z_A}{|r_i - R_A|} \qquad (2.3)$$

2.2.2 Wavefunction Methods

The Hartree-Fock self-consistent field (HFSCF) approximation is the foundation for wavefunction approaches (Desclaux, 1970). The Hartree-Fock methods are variational methods. The many-electron wave function is usually determined as the initial step by making a straightforward "informed" prediction before relying on the variational principle. This results in the mean values of the electronic Hamiltonian (Balian *et al.*, 1981; Kramer, 2008). The expectation value is always in the upper bound state concerning the electronic ground state energy $E_0[\Psi_0]$ for any wavefunction that has been hypothesised. Only when the estimated wavefunction matches the actual wavefunction does the ground state energy equal the expected value. Ψ_0, i.e., (E[Ψ] ≥ $E_0[\Psi_0]$). By optimising the trial or guess wavefunction, one can slowly approach the ground state energy thanks to the variational principle.

A slater function is the linear combination of the independent electron wavefunctions' product with all possible coordinate conformations. The Slater determinant likewise considers the electronic wavefunction's anti-symmetric quality(Coester and Kümmel, 1960). This is tremendously significant since the electrons are fermions and follow Pauli's exclusion principle(Reines and Sobel, 1974).

For the N-electrons system, the Hartree-Fock wavefunction is

$$\Psi(\{x_i\}) \approx \Psi^{HF}(\{x_i\}) = \frac{1}{\sqrt{N!}} \begin{bmatrix} \varphi_i(x_i)\varphi_j(x_i) & \cdots & \varphi_N(x_i) \\ \vdots & \ddots & \vdots \\ \varphi_i(x_N)\varphi_j(x_N) & \cdots & \varphi_N(\varphi_N) \end{bmatrix} \tag{2.7}$$

The slater determinant anti-symmetric criterion is met by substituting electron coordinates for spin-orbital labels in the columns marked by spin orbitals. When thinking about a two-electron situation, the anti-symmetric characteristic becomes apparent.

$$E^{HF} = < \Psi^{HF} \left| \hat{\mathrm{H}}_e \right| \Psi^{HF} >$$

$$= \sum_{i=1}^{N} \int \varphi_i^* (x_i) \left[\frac{-\nabla_i^2}{2} + V^{ext}(x_i) \right] \varphi_i(x_i) dx_i$$

$$+ \frac{1}{2} \sum_{i=1}^{N} \sum_{j=1}^{N} \int \int \varphi_i^* (x_i) \varphi_j^*(x_j) \frac{1}{|r_i - r_j|} \varphi_j(x_j) \varphi_i(x_i) dx_i dx_j$$

$$- \frac{1}{2} \sum_{i=1}^{N} \sum_{j=1}^{N} \int \int \varphi_i^* (x_i) \varphi_j^*(x_j) \frac{1}{|r_i - r_j|} \varphi_j(x_i) \varphi_i(x_j) dx_i dx_j \quad (2.9)$$

This demonstrates the conversion of a complex N-electron Schrödinger equation into a far more straightforward 1-electron Schrödinger equation.

$$\hat{F}_i \varphi_i(x_i) = \epsilon_i \varphi_i(x_i),$$

$$\hat{F}_i = \frac{-\nabla^2}{2} + V^{ext}(x_i) + V^{Hartree}(x_i) + V_i^{Exchange}(x_i) \quad (2.10)$$

Fock operator is another name for the one-electron Hamiltonian, $\hat{F}_i$. Its eigenvalues and eigenfunctions are, respectively, ϵ_i and φ_i. The external potential $V^{ext}(x_i)$ and the kinetic energy $\frac{-\nabla^2}{2}$ are the first two terms of the Fock operator. The coulomb electron-nucleus interactions to the i^{th} phrase are what make up the external potential. The final two terms explain the electron-electron interactions. The i^{th} electron is chosen via a Hartree potential that considers the repulsion between that particular electron and the system's total electron density.

$$V^{Hartree}(x_i) = \int \frac{n(x_j)}{|r_i - r_j|} dx_j,$$

$$n(x_j) = \sum_{j=1}^{N} |\varphi_j(x_j)|^2 \quad (2.11)$$

The fourth term, exchange potential ($\overset{x}{V_i^{Exchange}(i)}$), is exclusively accountable for the wavefunction's antisymmetric character.

Since $V^{Hartree}(x_i)$ has no classical counterpart, it must be expressed as an integral operator.

$$V_i^{Exchange}(x_i)\varphi_i(x_i) = \left[\sum_{j=1}^{N} \int \varphi_j^*(x_j) \frac{1}{|r_i - r_j|} \varphi_j(x_i) dx_j\right] \varphi_i(x_j) \tag{2.12}$$

The variable in the two spin orbitals is exchanged by $V_i^{Exchange}(x_i)$, as is clear from the equation above. Self-consistence field can resolve the pseudo-eigen value problem in equation 2.10.

Due to the coulomb repulsion of the mean-field Hamiltonian, the H.F. approach fails to predict the spatial organisation of the electrons. Many people agree that the electron correlation is what the H.F. equation needs. The correlation energy distinguishes the exact ground state energy from the ground state H.F. Despite making up a minor portion of all energy; it is crucial to many systems of interest in physics and chemistry.

When the energy term for the electron-electron interaction is added to equation 2.4, a better one-electron orbital is produced. Until self-consistency is reached, the cycle continues. However, HFSCF provides incredibly erroneous molecular energies. Since the method only focuses on the correlation effects and ignores the electron correlation effects, the modelling of chemical systems may be inaccurate. To solve intriguing physical and chemical issues, HFSCF is still crucial. While connected cluster (CC) (Reines and Sobel, 1974) and configuration interaction (CI) (Talmi, 1962), two alternative approaches, can address HFSCF's shortcomings, they typically require greater computational resources. The only difference between the CI's dynamics and the HFSCF approach is an extra one-electron wavefunction left empty during the construction of the overall wavefunction. The process makes room for the excited electron

configuration. The CI provides a precise way of solving the Time Independent Schrodinger equation. However, it has a high computational overhead. At the triple excitation level, the procedure can be terminated.

In addition to CI methods, there are quantum Monte Carlo (QMC) techniques. The energies for the many-body electron system are determined using QMC methods using random sampling (Talmi, 1962). The Schrödinger equation is transformed using the diffusion Monte Carlo approach into the integral Green's function, which is then roughly approximated by subsequent sampling. Although QMC approaches can be used with realistic solid-state systems, they can also have very high processing needs depending on the system. For systems with van der Waals dispersion, superconductors, and materials with significant low-temperature specific heat coefficients, QMC approaches may help obtain precise solutions to the TISE. Adopting an approximation scheme for evaluating these effects is desirable to the computing overhead of precisely estimating the correlation effects (Greeley *et al.*, 2002).

Density Functional Theory Methods

There are two different approaches to calculating the electronic structure and total energies of molecules and solids; the wavefunction-based methods (Salotto and Burnelle, 1970) and the density functional theory (DFT) methods. The former, which can be accurate if configuration interactions are included, is currently limited to 10 – 100 atoms. These techniques are often undesirable for the routine modelling complicated systems (Hammer & Norskov, 2000). Since electron density is utilised to determine a system's attributes rather than the wavefunction, DFT can handle systems with more electrons (100 and above). Due to the lower dimensionality, the electron density is preferable to the wavefunction. The dimensions (three) in DFT remain the same and is not dependent on the total number if electrons present in the system being calculated. This suggests that DFT applies to much larger macromolecular systems with many

electrons and is not limited to small systems. DFT is the most popular method for calculating electronic structure properties, especially in condensed matter physics (Ziegler 1991; Geerlings et al. 2003; Jones & Gunnarsson 1989; Miehlich et al. 1989)

First, the electron density is defined as

$$n(r) = N \int \dots \int |\varphi(x_1, x_2 \dots . . x_N|^2 d\sigma_1 dx_2 \dots . dx_N) \quad (2.13)$$

where the coordinates $\{x_i\}$ are both spatial and spin-related, while the other N-1 electrons have random locations and spin in the state described by ψ, n(r) calculates the likelihood of locating any N-electrons in the volume r. This is a non-negative, three-variable simple function that integrates the total amount of electrons,

$$N = \int n(r) dr \quad (2.14)$$

The hybrid functionals

These functionals possess the exchange-correlation that is known to exist between the H.F. functional and several broader approaches to the DFT exchange and correlation energy. The "adiabatic connection" equation, a rigorous *ab-initio* equation for the exchange-correlation energy of DFT, forms the foundation of the theory underlying the hybrid functional. The mathematic representation of this theory is written as

$$E_{xc} = \int_0^1 U_{xc}^{\lambda} d\lambda,$$

(2.24)

where $U_{xc}^{\lambda}$is the potential energy of exchange and correlation at λ which is also an interelectronic coupling strength parameter that activates the $\frac{1}{|r_i - r_j|}$ coulomb repulsion between electrons. The non-interacting electron and the interacting electrons at density n(r) are

connected by this equation (r). Exchange and correlation functionals from G.G.A. and LDA are combined with some mixing with H.F. exchange.

This is predicated on the simple H.F. exchange at the non-interacting λ=0 border. The B3LYP functional is one of the most prevalent examples, if not the most. Three factors, designated as a_{1-3}, are necessary for the B3LYP functionals (Becke, 1993) to control the mixing with the H.F. exchange, density exchange, and correlation functional. It can be expressed as

$$E_{xc} = E_{xc}^{LDA} + a_1(E_x^{HF} - E_x^{LDA}) + a_2\Delta E_x^{GGA} + a_3\Delta E_c^{GGA}.$$

(2.25)

Again, B88 (Becke, 1988) and L.Y.P. (Lee *et al.*, 1988) are applied to G.G.A. exchange and correlation functionals. The equation can be written with two parameters less as;

$$E_{xc} = E_x^{GGA} + a(E_x^{HF} - E_x^{GGA})$$

(2.26)

A class of functionals with the same number of parameters as their originating G.G.A.s is suggested by setting a=1/4 (using the bases from perturbation theory). For instance, its hybrid PBE0 (Adamo and Barone, 1999) is generated when P.B.E. is the G.G.A. utilised in equation (2.26). Another popular hybrid functional that contains 50% H.F. exchange is BH&HLYP (Perdew *et al.*, 1996). When examining the gas phase properties of solids and molecules, these functionals have significantly outperformed G.G.A.s and LDAs.

The hybrid meta G.G.A. functional, a combination of meta G.G.A.s and hybrid functionals that have been parameterised to suit certain systems, is found in the fourth rung (molecular database). The lot includes PW6B95 and MPWB1K (Zhao *et al.*, 2005). On Jacob's ladder, the functionals get increasingly complicated above the rungs. The additional mathematical

complexity does not necessarily improve the effectiveness or precision of the total energies(Moroni *et al.*, 1997).

Poor estimations of binding energies and molecular structures are frequently the result of LDA computations. Modern G.G.A. computations, however, can produce substantially superior results when combined with adequate models for the surface structure (basis sets). For instance, vibrational frequencies are estimated with a 5% accuracy, and bond lengths and solid lattice constants are recreated within a few hundredths of an angstrom. Calculated adsorption energies can be determined to be within 0.15 eV when compared to experimental values, which are most precisely obtained using Single-Crystal Adsorption Calorimetry (Borroni-Bird and King, 1991).

2.2.3 Basis Sets

Most electronic structure strategies to comprehend microscopic systems call for expanding the wave function regarding the basis functions (Sumpter *et al.*, 1998). Localised basis sets, such as Gaussian, atomic orbitals, linearised muffin-tin orbitals (LMTOs) (Bose, 1998), et cetera, and delocalised basis sets, such as plane waves (including augmented plane waves (LAPWs) (Farquhar and Inglesfield, 1989), et cetera), are the two different forms of basis sets. The option is determined by preference and the type of problem being researched. While localised (LMTOs), and plane waves are employed in slab-type calculations; localised functions are typically the preferred option in cluster-type models.

2.2.4 The plane wave pseudopotential method

One of the most popular DFT implementations is the plane wave pseudopotential (PWPP) approach (Ordejn *et al.*, 1995; Troullier and Martins, 1991). The electronic wave functions and pseudopotentials are expanded in the PWPP approach using the plane wave basis set, which

also models the interactions between electrons and ions. There are several appealing qualities of plane waves. They are straightforward, built orthogonally, and unbiased by atomic locations. Theoretically, the PW basis set can only be finished with unlimited plane waves. However, in actual calculations, we only consider plane waves contained within an E_{cut} sphere because there are only a finite number of them.

$$\frac{-1}{2}\nabla^2|K+G|^2 \leq E_{cut}$$

(2.27)

In contrast to calculations using localised (atomic-like) basis sets, computations using plane waves can be verified for convergence by expanding the basis set's size, as dictated by the kinetic energy cut-off. The sole factor in the theory that affects how accurately our system is described is the energy cut-off. We can increase the computational accuracy by increasing the energy cut-off value and examining the convergence of the desired attributes. The PW basis set significantly benefits the Pulay set (Broqvist *et al.*, 2009; Tapavicza *et al.*, 2007). The energy derivatives are computed without the inclusion of these terms. As a result, there is no need for adjustment of the Hellmann-Feynman formulas for force and force constants (Baroni *et al.*, 2001).

Pseudopotentials, when combined with plane waves, make them an efficient potential designed to replace the atomic all-electron potentials. This eliminates the core states and allows nodeless pseudo-wavefunctions to represent the valence electrons (Chelikowsky, 2000). The pseudopotential approximation sees each nucleus and its core electrons as a frozen core that does not change in reaction to changes in its environment. There is an assumption that a system's most important physical attributes are directly linked to this system's valence electrons (Bonačić-Koutecký *et al.*, 1991). Thus, the valence electrons move in the external

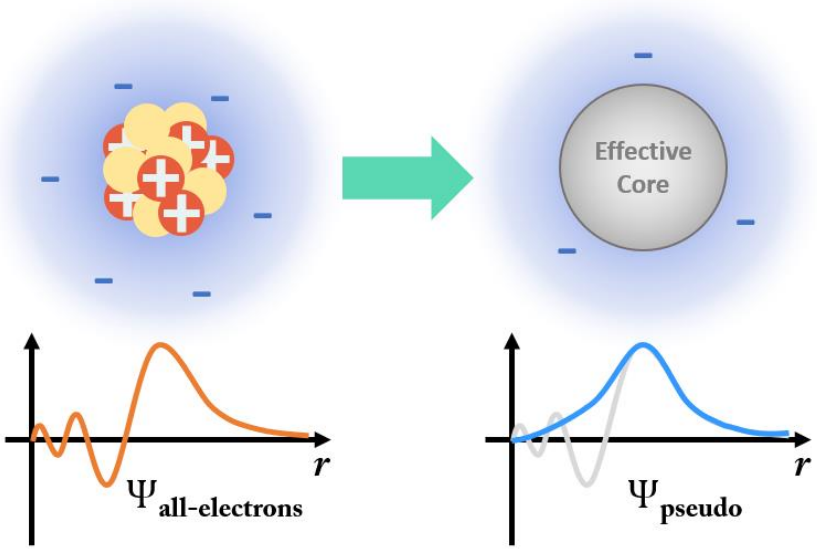

Figure 2.1 Image depicting the potential created when the core electrons of a system are considered chemically inert

field these inert ionic cores generate. The pseudopotential attempts to mimic how the true atomic potential interacts with the valence states without explicitly accounting for the core states. This offers a logical approach to separating the central function of electrons in the electrical structure problem (Bartlett, 1981).

2.2.5 Van der Waals forces

Depending on the degree of distortion after the polarization of orbitals in a covalent interaction, attracting or repelling forces are produced in the electron cloud or atom density. Their proximity to one another brings on two atoms' deformation. A force of attraction is produced by an induced dipole that strengthens as the atoms come closer to one another. The Londons' dispersion is the name of the attraction force (Fowkes, 1980).

Owing to the electron cloud overlap, atoms repel one another when they are very close. The sum of their Van der Waals radii prevents the formation of a covalent bond known as Pauli's repulsion (Zefirov, 2001) is the name for this aversion. As the atoms draw closer together,

Pauli's repulsion becomes greater. The Leonard Jones potential is the most widely utilised, primarily due to its computational benefit, even though other potentials may be used to explain the behaviour of neutral atoms and molecules.

$$U_{vdW} = U_{LJ}(r_{ij}) = 4\varepsilon_{ij}\left[\left(\frac{\sigma_{ij}}{r_{ij}}\right)^{12} - \left(\frac{\sigma_{ij}}{r_{ij}}\right)^{6}\right]. \qquad (2.28)$$

Pauli's repulsion term is roughly represented by the first portion in the brackets. The induced dipole term is the second one. In other words, the force field repels at close ranges while attracting at a farther distance. $\varepsilon_{ij} = \sqrt{\varepsilon_{ii}\varepsilon_{jj}}$ and $\sigma_{ij} = \frac{\sigma_{ii} + \sigma_{jj}}{2}$

To do a molecular mechanics calculation, the parameters ε and σ must be determined because they are unique to each element. The parameter σ denotes the separation between atoms at which repulsion and attraction are equal, and the total energy of the interaction is zero. The distance between particles i and j, denoted by the parameter r_{ij}, corresponds to the depth of the minimum energy.

In the next chapter, we will examine the specific computational methods used and state the justification for employing them in this work.

CHAPTER THREE

3.0 MATERIALS AND METHODS

3.1 Computational Methods

The Density functional theory (DFT) was employed with the plane wave basis sets for all calculations. The Quantum ESPRESSO (Giannozzi *et al.*, 2009) package utilised in all simulations performs fully self-consistent DFT calculations to solve the Kohn-Sham equations (Kohn and Sham, 1965). The ionic cores were represented by norm-conserving pseudopotentials (Hamann *et al.*, 1979) for the Hf, W, Zn, Cu and O atoms. Pure DFT band structures fail to give reliable quantitative values for the band gaps of strongly correlated systems like insulators and semiconductors (Hybertsen and Louie, 1986). The band gap values are often underestimated by as much as 1.0 eV or more (Hybertsen and Louie, 1985). To remedy this, the Heyd-Scuseria-Ernzerhof (HSE06) exchange-correlation functional (Heyd *et al.*, 2003), a correction which uses an error-function screened Coulomb potential to calculate the exchange portion of the energy to improve the computational efficiency of such systems is used. Hence, the band structures and density of states of the various systems, except for m-WO_2, were studied using the DFT with the HSE06 functional. The Fermi-surface effects were treated by the smearing technique of Fermi-Dirac and a smearing parameter of 0.003 Ry. An energy convergence threshold defining self-consistency of the electron density was set to 10^{-6} eV and a beta-defining mixing factor for self-consistency of 0.2. The slab modelling technique was used in describing the various surfaces m-HfO_2(100), m-WO_2(100), w-ZnO(01-10) and m-CuO(111) studied in this work. Periodic boundary conditions were set to avoid the reproducibility of the central super-cell. A 12 Å vacuum region was set perpendicular to each surface. This was aimed at avoiding interactions between the periodic slabs. The kinetic energy cut-off and charge density cut-offs were set at 40 Ry (544 eV) and 320 Ry (4354 eV),

respectively, for the basis set's expansion. These parameters were sufficient for expanding the plane-wave basis set while allowing the convergence of the total energy of the systems studied. The Monkhorst-Pack mesh k-point grid (Monkhorst and Pack, 1976) was employed in sampling the Brillioun zone of the crystals. These were set at (7 x 7 x 7) and (2 x 2 x1) for the bulk and surface systems. The graphics of the atomic structures and the iso-surfaces of the differential electron density plots have been prepared with the Gnuplot (Williams and Kelley, 1998), Vesta (Momma and Izumi, 2008) and XCrysDen software (Kokalj, 1999).

A peptidoglycan layer was adsorbed onto the various surfaces to simulate the interaction between the metal oxides and bacteria. Adsorption was done using the peptidoglycan layer's simplest peptide bonds and glycan chains. Models were produced using Avogadro software (Hanwell *et al.*, 2012) for amino acid structures (d-alanine, meso-diaminopimelic acid and d-isoglutamic acid) and glycan strands (n-acetylglucosamine and n-acetylmuramic acid).

CHAPTER FOUR

4.0 RESULTS AND DISCUSSION

4.1 Structural and Electronic Properties of Transition Metal Oxides

4.1.1 Bulk and Surface Properties of Hafnium Oxide (HfO_2) and HfO_2 (100)

Like zirconium dioxide (ZrO_2) and titanium dioxide (TiO_2), hafnium oxide, better known as hafnia, is a high-k material with a dielectric constant, k, that ranges between ~20 to 25. A significant characteristic of this material is its large band gap (~5.8 eV) and excellent thermal and chemical stability. Based on this, hafnia has been utilized as a material in optical coating and as a dielectric in capacitors like DRAM capacitors and advanced semiconductor devices. In the solid state, this material crystallizes in four forms: the monoclinic, orthorhombic, cubic, and tetragonal phases. The orthorhombic, cubic, and tetragonal phases have *Pca21*, *Fm3m*, and *P42/nmc* space groups, respectively. However, the most stable crystal form is the monoclinic form with the space group *P21/c* and thus would be an ideal candidate in a practical AD setting. The bulk monoclinic HfO_2 has four formula units in the unit cell, as shown in Figure 4.1.

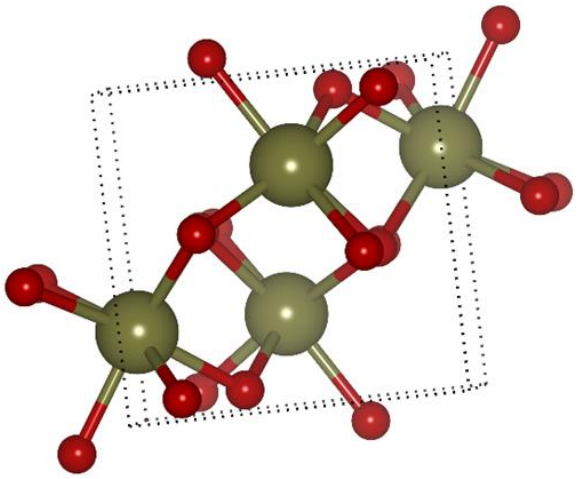

Figure 4.1: The unit cell of the bulk crystal structure of monoclinic hafnium oxide (m-HfO_2) showing the hafnium (Hf) atoms in green and the oxygen atoms in red

A generalized gradient approximation Perdew-Burke-Erzenhof exchange-correlation functional is applied for optimizing the bulk crystal structure. The lattice constant calculated is 5.14 Å, close to the experimental value of 5.12 Å (Zhao and Vanderbilt, 2002), as shown in **Table 4.1.** It is well-known that GGA overestimates the lattice constant of systems by approximately 1.8 %, which may have accounted for the difference in values for the experimental and computed structural parameters. This level of theory severely underestimates the band gaps of strongly correlated systems. Thus, significant improvements in band gap prediction are achieved with hybrid functionals like the Heyd-Scuseria-Erzenhof (HSE) screened hybrid functional. The partial density of states of the monoclinic HfO_2 is studied using the HSE-screened hybrid functional (Figure 4.2).

Table 4:1 Lattice constant and Bulk modulus of HfO_2

System (Monoclinic HfO_2)	**Space Group**	**Experiment**	**Calculated (PBE-GGA)**	**Calculated (HSE)**
Lattice Constant / Å	*P21/c*	a = 5.07 b = 5.14 c = 5.29	a = 5.07 b = 5.14 c = 5.30	a = 5.21 b = 5.33 c = 5.43
Band Gap Energy/eV		5.00	4.02	4.96

The band gap of the bulk system using the HSE hybrid functionals is determined as 4.96 eV, which is in close agreement with the experimental value of 5.0 eV (Toyoda *et al.*, 2004). The plot shows that the unoccupied orbitals in the conduction band region are located on the Hf d orbitals, whiles the valence band region shows high occupancies of electrons in the O p orbitals, which get excited to the conduction bands. The same applies to the system's conduction band

maximum (CBM) and valence band minimum (VBM), offering a p-type semiconducting material. This indicates that Hf-O bonding in the system is highly ionic and weakly covalent. The bonding characteristics in the monoclinic structure are known to have the oxygen atoms either threefold or fourfold coordinated, while all the Hf atoms are in a sevenfold-coordinated configuration. The above characteristics confirm previous experimental data (Mostefai *et al.*, 2018). The electronic properties of the system are also studied by calculating the band structure of the system.

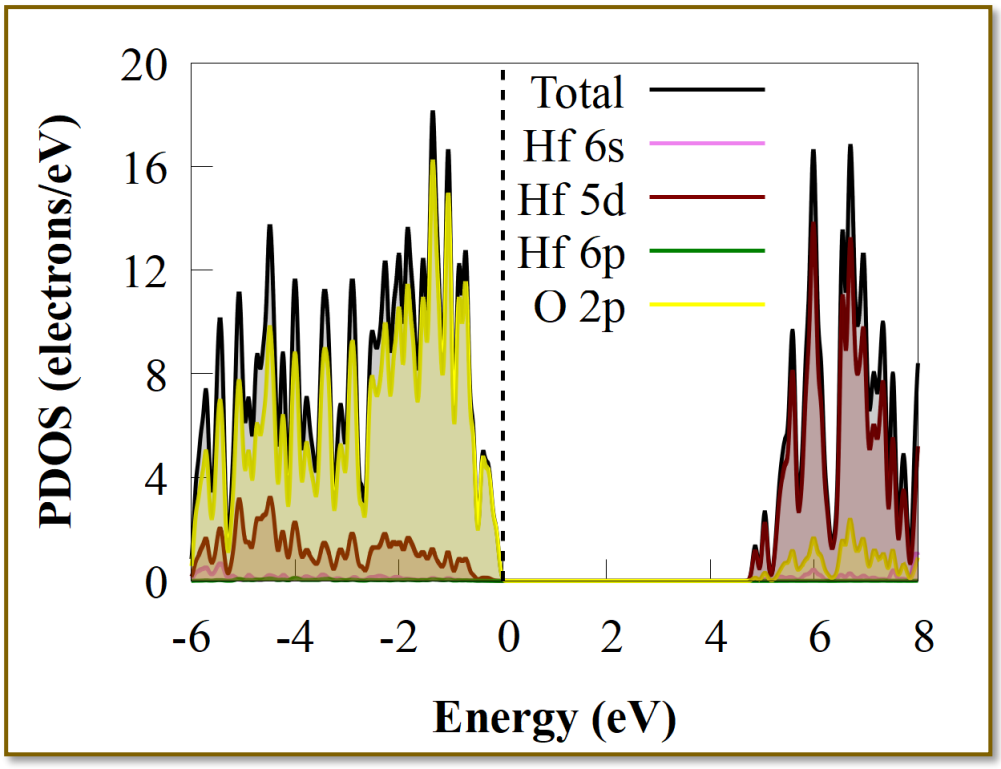

Figure 4.2 Projected density of states of the bulk monoclinic HfO_2 system.

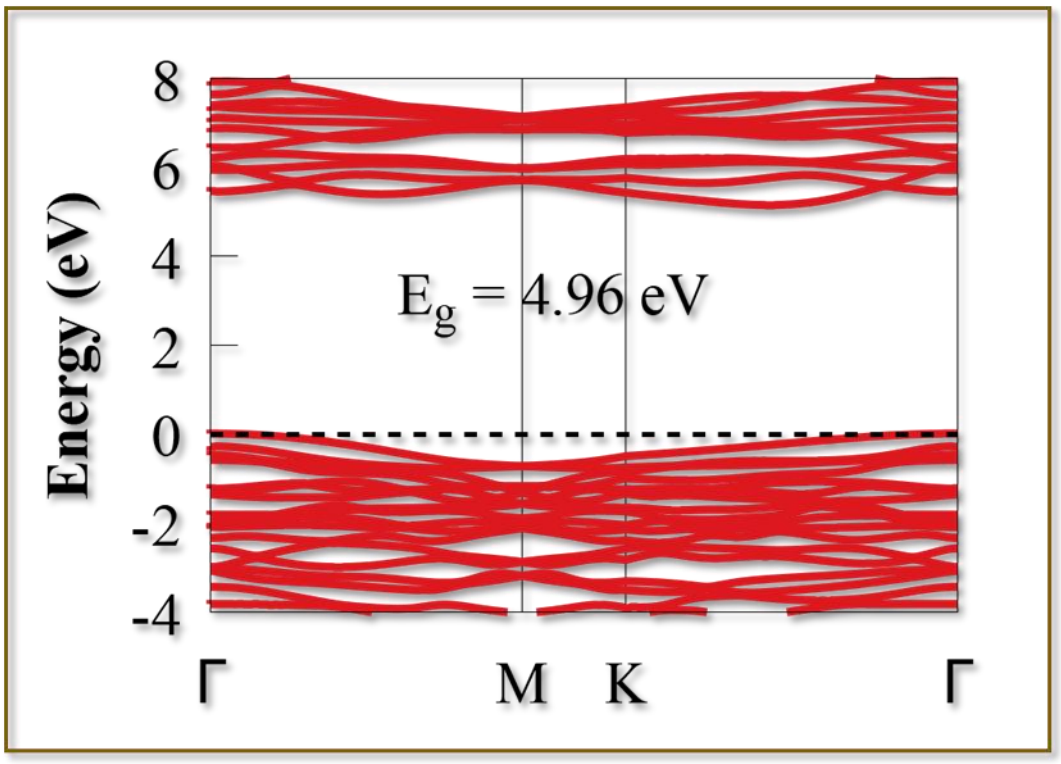

Figure 4.3 Projected band structure of the bulk monoclinic HfO_2 system

Previous experimental work has shown that the (100) surface of hafnium oxide increases the biogas yield of an AD system by 83.04 % (Yun *et al.*, 2021b). This work cleaved the bulk crystal system along the (100) Miller indices, and a 48-atom supercell was built (Figure 4.4). Along the (100) plane, two terminations are observed. The Hf-terminated and O-terminated surfaces were both studied in this work. It is worth noting that the Hf-terminated (100) surface is observed to have occupied electronic states within the band gap of the system. This shows that the Hf-terminated (100) surface can show metallic properties; thus, its use as a candidate for diet can be ascribed to that. However, the (100)-O surface has an energy gap, and the Fermi level is in the valence band region. The electronic structure of the Hf- terminated (100) surface (Figure 4.5) shows that the structure is more conductive and hence would easily donate and transmit electrons from the acetogens to the methanogens. Our calculated surface electronic

structures of HfO_2 suggest that the experimentally probed HfO_2 surfaces could be the ones terminated by Hf atom layers. However, the charge transfer plots would confirm the extent of electron transmission between the metal oxide and the peptidoglycan layer.

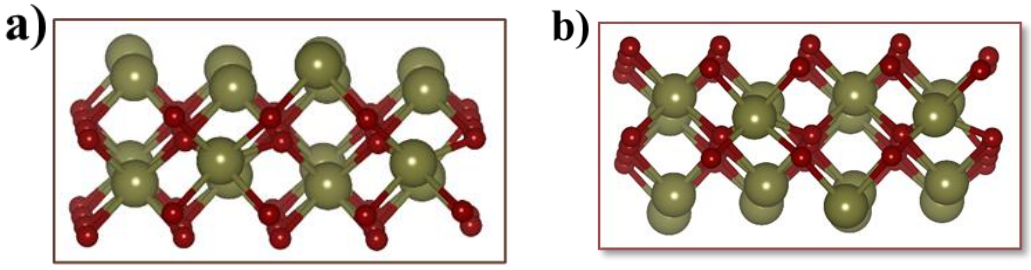

Figure 4.4 Surface (100) of the hafnium oxide crystal a) Hf-terminated and b) O-terminated

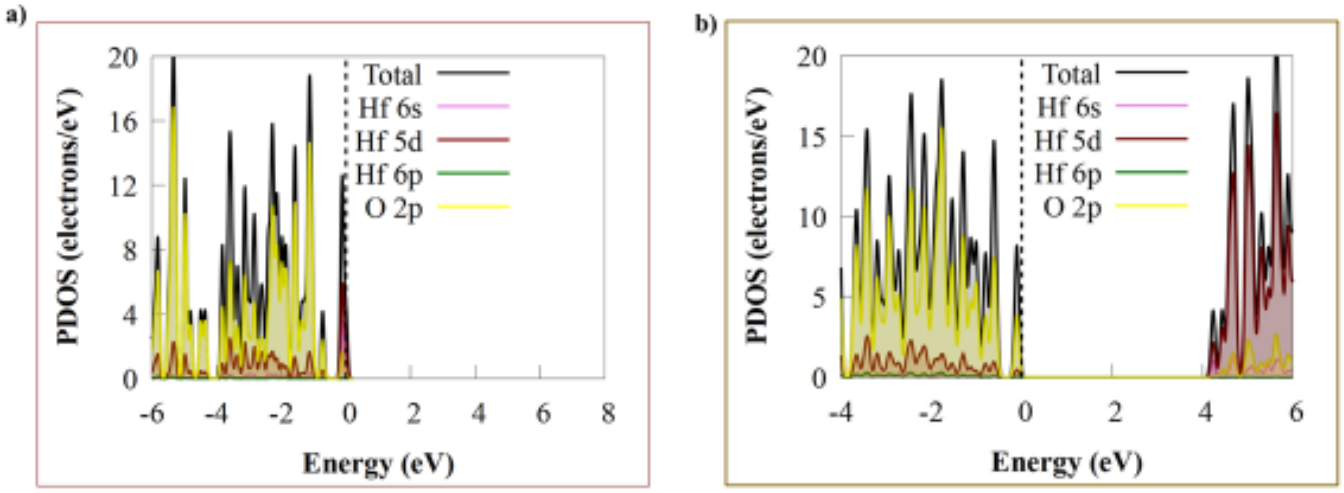

Figure 4.5 Projected Density of States of a) Hf-terminated and b) O-terminated surfaces of the (100) m-HfO_2 surface

4.1.2 Bulk and Surface Properties of Tungsten (IV) oxide (WO_2)

Formed from reducing tungsten trioxide with tungsten powder, tungsten (IV) oxide (WO_2) is usually oxidised in metastable intermolecular composites. The metal oxide crystallizes in the stable monoclinic crystal system and the high-temperature metastable orthorhombic phase. The metastable phase is a semiconductor with a band gap energy of 6.67 eV. However, the monoclinic (stable phase) exhibits metallic properties. Based on this, the stable crystal form used in this study is the monoclinic WO_2 system. A P121/c1 space group characterizes this system, and its Pearson symbol is mP12. Figure 4.6 illustrates the 12-atom bulk crystal system. The lattice constants, bulk modulus and band gap energies, determined using the GGA PBE exchange-correlation functionals, are compared to experimental data (Table 4.2).

The lattice constants of the bulk monoclinic WO_2 system are determined as a = 5.22 Å, b = 4.79 Å and c = 5.65 Å and are in close agreement to experiment (Palmer and Dickens, 1979). As opposed to other functionals, PBE underestimates the bulk modulus of materials (He *et al.*, 2014), resulting in a bulk modulus of 169.9 GPa as opposed to 189.06 GPa (Shofner *et al.*, 2016) as determined by previous experiments.

In 2021, it was observed that adding m-WO_2 in an AD system containing dairy manure with sludge yielded exciting results, as biogas production increased by 78.30% (Yun et al., 2021b).

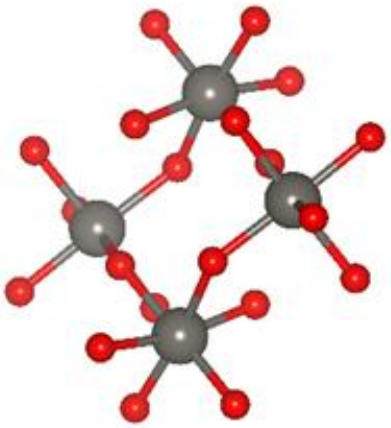

Figure 4.6 Bulk crystal structure of WO_2 showing the tungsten atoms in grey and the oxygen atoms in red.

The electronic properties of the bulk monoclinic crystal were studied using the generalized gradient approximation Perdew-Burke-Erzenhof (GGA-PBE) exchange-correlation functional. A zero-band gap energy was recorded for this material, and the band structure shows overlapping bands at the Fermi level, thus confirming its metallic properties, as shown in Figure 4.7.

Table 4:2 Lattice constant and Bulk modulus of WO_2

System (Monoclinic WO_2)	**Space Group**	**Experiment**	**Calculated (PBE-GGA)**
Lattice Constant / Å	P121/c1 (14)	**a = 5.56** **b = 4.89** **c = 5.66**	**a = 5.22** **b = 4.79** **c = 5.65**
Bulk Modulus (Bo)/ GPa		189.06	**169.90**

The plot shows that the W 5d orbitals primarily occupy the conduction band region states through the Fermi region. In contrast, the valence band region shows high occupancies of the

O p states. The above characteristics also confirm previous experimental data (Wells, 1984). The electronic properties of the system are also studied by calculating the band structure of the system. The bulk crystal's projected band structure confirmed the bands overlapping at the Fermi level.

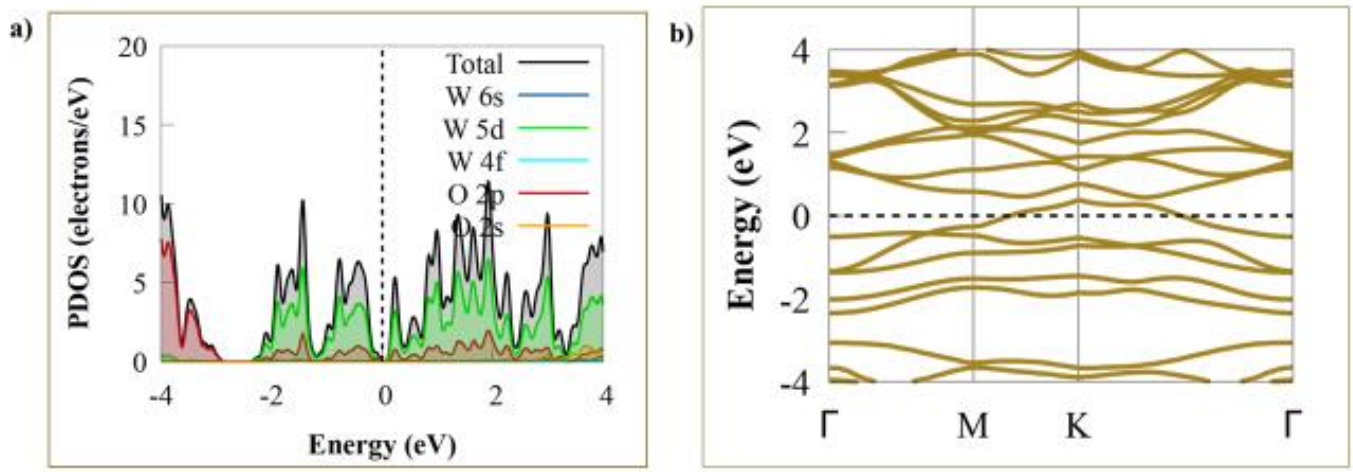

Figure 4.7 Electronic Structure a) Projected density of states b) Projected band structure of the bulk monoclinic WO_2 system

To obtain the surface slabs for the adsorption, the bulk crystal system was cleaved along the (100) Miller indices, and a 48-atom supercell was built. The W-terminated and O-terminated surfaces were studied in this work, as shown in Figure 4.8. From the electronic structure study, it has been observed that both surfaces exhibit metallic properties and thus could transmit electrons easily. However, the extent of transmission remains unclear, and thus the charge transfer plots could provide insight into that. A projection of the density of states for each surface can be seen below in Figure 4.9 and Figure 4.10

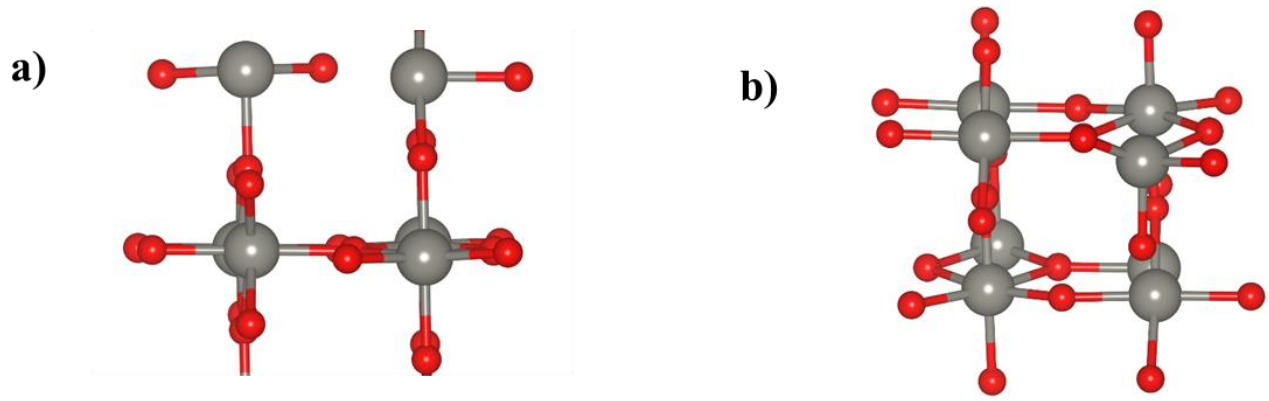

Figure 4.8 Surface (100) of the monoclinic tungsten oxide crystal a) W-terminated and b) O-terminated

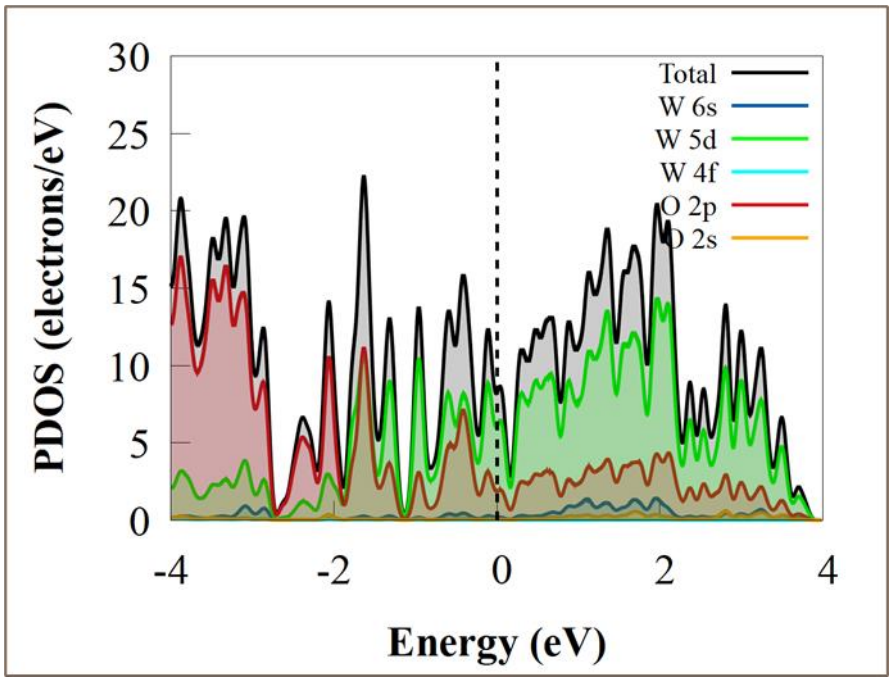

Figure 4.9 PDOS of the W-terminated 100 surface

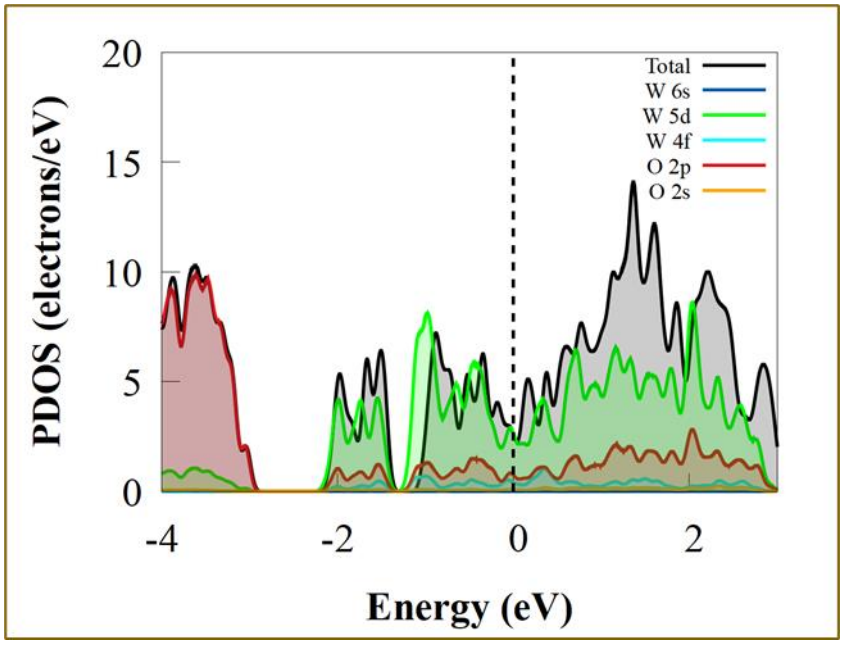

Figure 4.10 PDOS of O-terminated Surface

4.1.3 Bulk and Surface Properties of Zinc Oxide (ZnO)

Sourced from zincite, the zinc oxide system crystallizes in hexagonal wurtzite form, cubic zincblende, and rocksalt phase. The wurtzite phase, however, has been noted to be the most stable thermodynamic phase at ambient conditions with the $P6_3mc$ *(189)* space group (Hermann–Mauguin notation). The unit cell of the wurtzite structure presents a system with every zinc atom tetrahedrally coordinated with four oxygen atoms, as shown in Figure 4.11. The calculated lattice constants of a = 3.25 Å and c = 5.21 Å and the calculated bulk modulus of 113 GPa have been captured in Table 4.3. These values agreed with the experimental values of a = 3.25 Å and c = 5.21 Å (Guo *et al.*, 2002) and 186.0 GPa (Karzel *et al.*, 1996) for the bulk modulus.

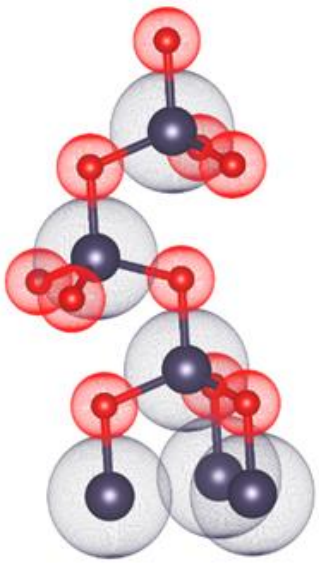

Figure 4.11 Bulk crystal structure of ZnO shows the dark blue zinc atoms and the red oxygen atoms.

Table 4:3 Lattice constant and Bulk modulus of ZnO

System (Wurtzite Phase ZnO)	**Space Group**	**Experiment**	**Calculated (PBE-GGA)**	**Calculated (HSE)**
Lattice Constant / Å	$P6_3mc$ *(189)*	a = 3.25 c = 5.21	a = 3.41 c = 5.22	a = 3.253 c = 5.254
Bulk Modulus(Bo)/ GPa		183.0 139.6	130.0	229.7
Band Gap Energy /eV		3.30	0.74	3.40

Wurtzite zinc oxide is a wide band gap semiconductor with a band gap energy of 3.3 eV (Bashyal *et al.*, 2018). In this work, we recorded a band gap of 3.4 eV and illustrated the

projected density of states plot (Figure 4.11). The plot shows that the Zn 4s highly occupy the conduction band region states, whiles the valence band region shows high occupancies of the O p states. However, shallow peaks were observed for the Zn 4s orbital at the CBM. The Zn outer states are split into two groups above the Fermi level between 2 to 4 eV. The electronic band structure shows a direct band gap of 3.4 eV at the Gamma-point. The w-ZnO system has a tetrahedral condonation characteristic of a sp^3 covalent bonding, but it is worth noting that an ionic character also exists in this system.

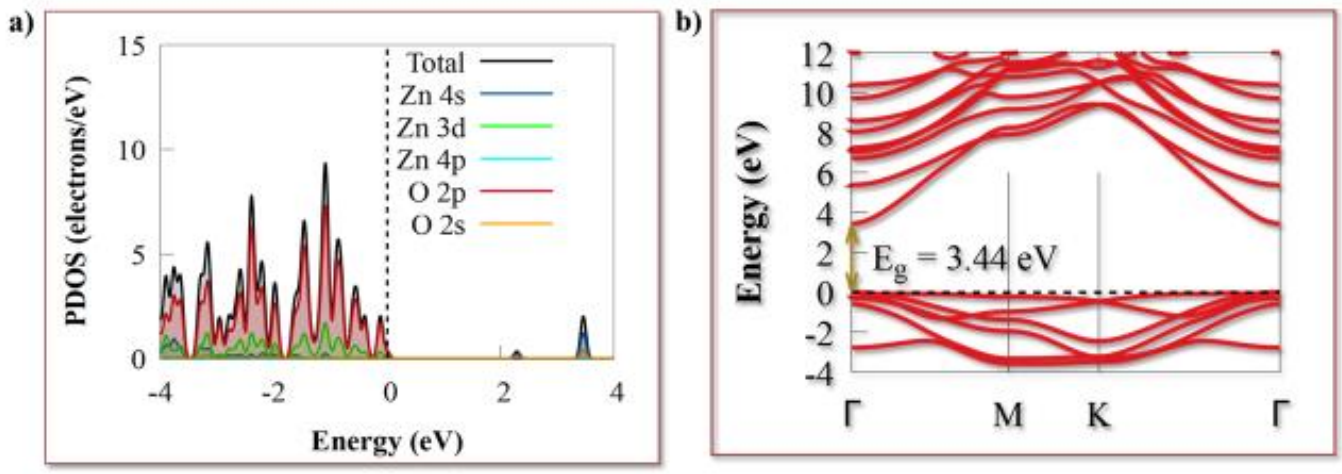

Figure 4.12 Electronic structures: a) projected density of states and b) band structure of the bulk w-ZnO studied using the HSE hybrid functional

Researchers employed ZnO nanoparticles to enhance methanation, and data shows that they acted as inhibitors, reducing production by up to 74 % (Luna-delRisco *et al.*, 2011b). To obtain the surface sheets used in their work, the w-ZnO system was cleaved along the $(10^{-}10)$ (most accessible surface to treat theoretically), and a 32-atom supercell was built and is shown in Figure 4.13. In the Pdos plot (shown in Figure 4.14), it is observed that w-ZnO is a semiconducting material with Zn s states occupying the conduction band region and the O p states dominating the valance band region.

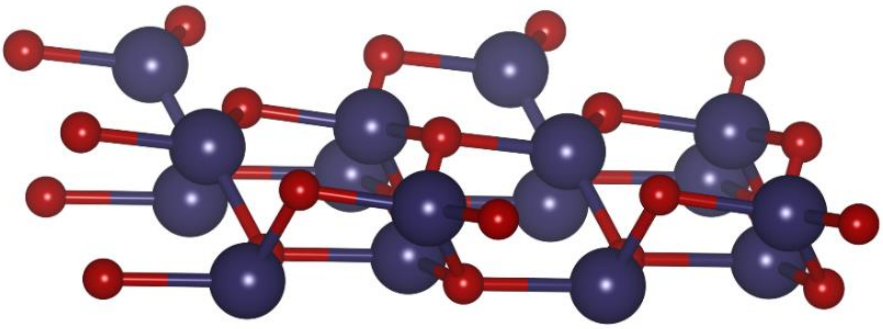

Figure 4.13 The 10-10 surface of the w-ZnO structure

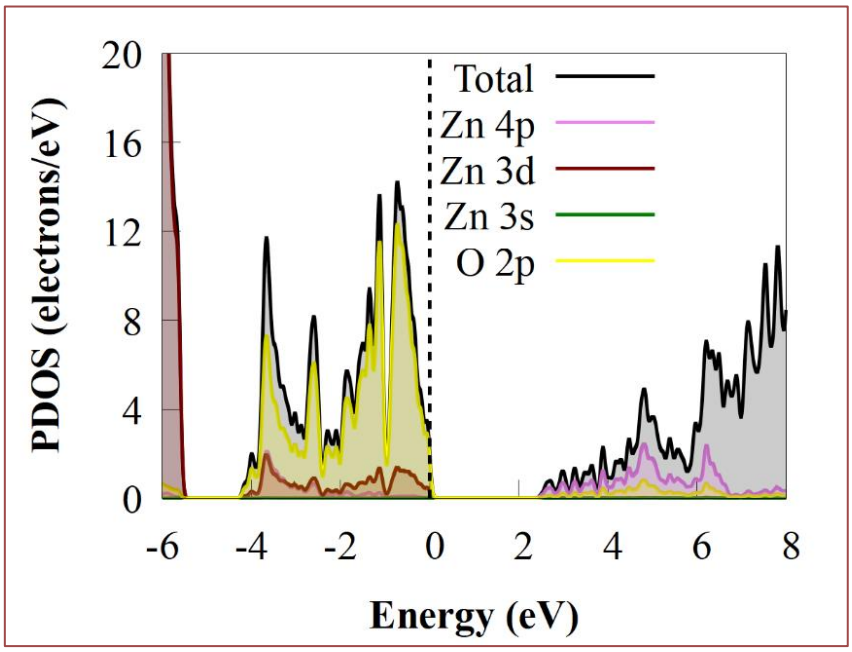

Figure 4.14 Projected density of states of the 10-10 surface of w-ZnO showing the Zn s occupancies and the O p states at the conduction and valence regions, respectively.

4.1.4 Bulk and Surface Properties of Copper Oxide (CuO)

The copper oxide crystal is a semiconducting material with two different metal oxidation states, the first of which is Cu (I) and the second of which is Cu (II). The former (Cu I) has band gap energies between 1.4-1.9 eV and is a monoclinic crystal system with the C12/c1 [15] space group, whiles the latter has band gap energies between 2.2-2.4 eV and has a cubic structure. Previous experimental studies have explored the use of CuO in AD systems (Luna-delRisco *et al.*, 2011c; Tetteh and Rathilal, 2021). Particularly in an anaerobic digester treating sludge, this material was noted to reduce biogas production by 30% (Luna-delRisco *et al.*, 2011c). The monoclinic crystal form is known to be the most stable form and thus was employed in this study to investigate how the material acts as an inhibitor in AD systems. Based on this, an 8-atom unit cell was optimized using the GGA PBE exchange-correlation functional (Figure 4.15). The calculated lattice constant for the bulk m-CuO material obtained is a = 4.65 Å. A bulk modulus of 138 GPa is also determined using the same level of theory as shown in Table 4.4. These parameters are compared to experimental data and seem to agree (Allmann *et al.*, 2009).

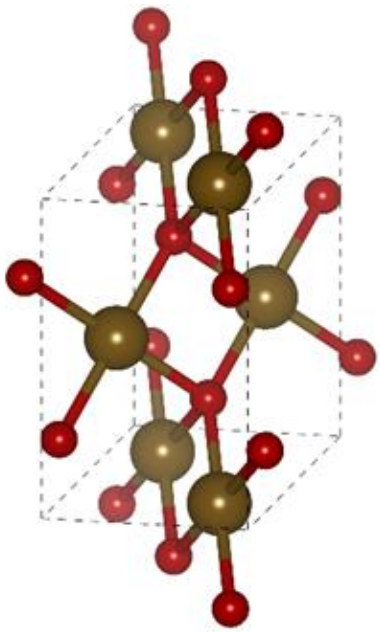

Figure 4.15 Bulk crystal structure of CuO shows the brown copper and red oxygen atoms

Table 4:4 Lattice Constant and Bulk modulus of bulk monoclinic CuO

System (Monoclinic CuO)	Space Group	Experiment	Calculated (PBE-GGA)	Calculated (HSE)
Lattice Constant / Å	C12/c1 [15]	a = 4.68 b = 3.42 c = 5.13	a = 4.25 b = 4.06 c = 5.16	a = 4.65 b = 3.42 c = 5.12
Bulk Modulus(Bo)/ GPa		146		138
Band Gap Energy/ eV		1.20		0.96

The electronic properties of the bulk monoclinic CuO systems are obtained by studying the projected density of states and the projected band structure of the system. These studies were conducted using the HSE hybrid functionals, which help describe the electronic properties of

strongly correlated systems like CuO. From the pdos plot, it is observed that there is a formation of midgap states with high peaks from the O p states. This could be helpful in processes like photocatalysis as it can reduce the recombination rate. It is worth noting that there is significant Cu-d and O-p hybridization of the states close to the Fermi energy. A direct band gap is observed from the projected band structure plot. The band gap energy is underestimated even with the HSE hybrid functionals, and an energy gap of 0.9 eV is recorded in this work compared to the bulk band gap range between 1.1 - 1.9 eV (Ray, 2001; Tahir and Tougaard, 2012). These plots are shown in Figure 4.16.

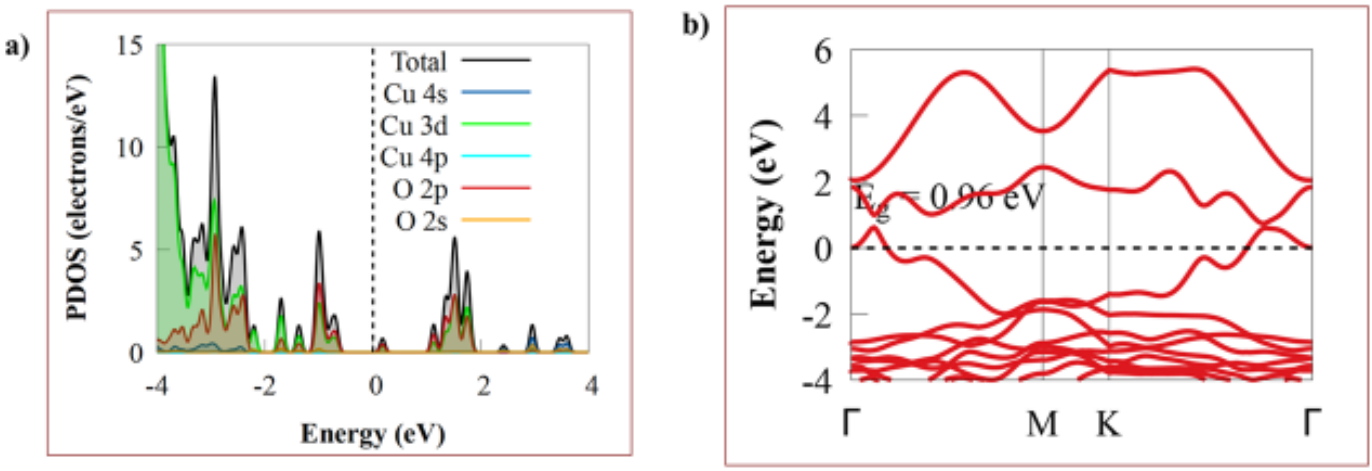

Figure 4.16 Projected Density of states and Band structure of the bulk monoclinic CuO system

CuO(111) is the most stable surface and thus was used in this study, shown in Figure 4.17. A 96-atom supercell was built and optimized using the GGA PBE exchange-correlation functional. The electronic properties of the surface were studied by employing the HSE hybrid functionals. From the pdos plot (Figure 4.18), it is observed that the electronic structure of the (111) surface is quite similar to the electronic structure of the bulk system. The formation of mid-gap states is observed at the Fermi level by O p states. The O p midgap states are formed

at the valence band region in the bulk system. The extent of charge transfer is studied to investigate the reason behind CuO's inhibitory properties, and the results are discussed below.

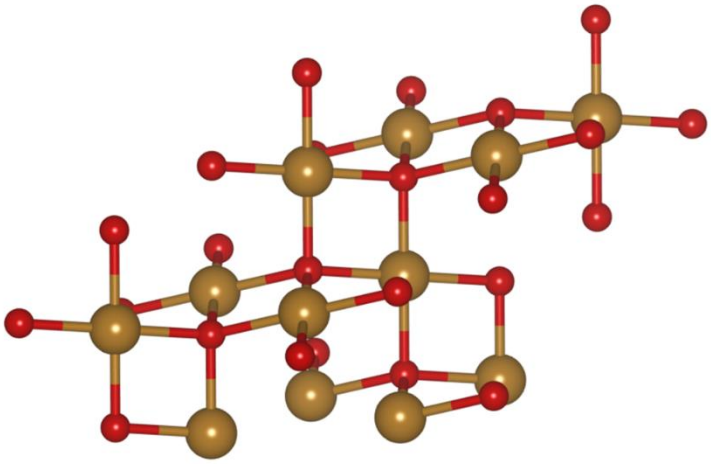

Figure 4.17 CuO (111) surface optimized using the GGA PBE exchange-correlation functional.

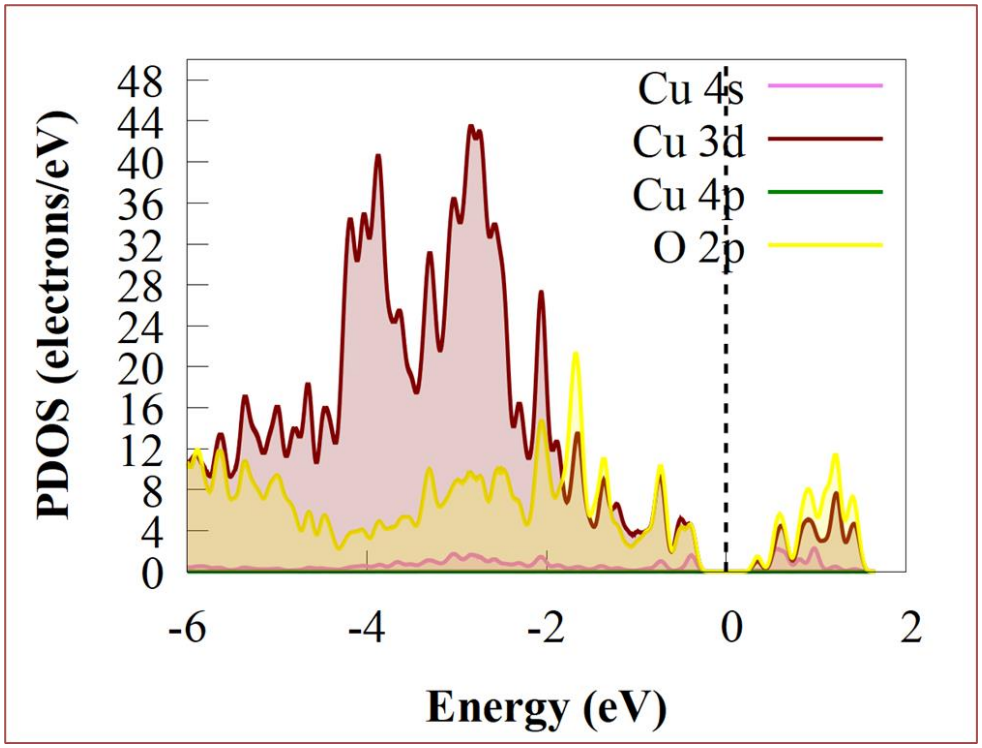

Figure 4.18 The projected density of states of the CuO (111) surface studied using the HSE hybrid functionals

4.2 Peptidoglycan

Generally, the acetogenic bacteria's cell envelope comprises the cell wall and the cell membrane. Among the various macromolecules that make up bacteria, the peptidoglycan, or murein, is a unique large polysaccharide containing sugars and amino acids that form a cloth-like layer outside the plasma membrane, thus making up the cell wall. This layer maintains the structural integrity of the bacterial cell by resisting turgor pressure and is responsible for transporting proteins, et cetera, across the cell. It has been established from previous research that in microbial electrosynthesis, bacteria (specifically gram-positive bacteria with thick cell walls composed of peptidoglycan, teichoic acids, and sometimes a glycoprotein S layer) can undergo extracellular electron transfer to electrodes (like metal oxide semiconductors) (Choi *et al.*, 2014; Sasaki *et al.*, 2014). This work explores the role of peptidoglycan in extracellular

electron transfer by studying the interactions between the peptidoglycan layer and transition metal oxides involved in the AD process.

The scope of this study is limited to acetogens that undergo diet, such as the Pelotomaculum thermopropionicum and the interaction of its peptidoglycan layer with the metal oxides. Suppose one wants to study the nature of these interactions within the present knowledge of experimental and computational surface science, model systems are employed due to the complexity of macromolecules such as proteins and carbohydrates. In Pelotomaculum thermopropionicum, the peptidoglycan layer comprises the linear glycan strands (alternating N-acetylglucosamine, GLcNAc and N-acetyl muramic acid, MurNAc residues), cross-linked by peptides (D-alanine, D-isoglutamic acid and Diaminopimelic acid) as shown in Figure 4.19.

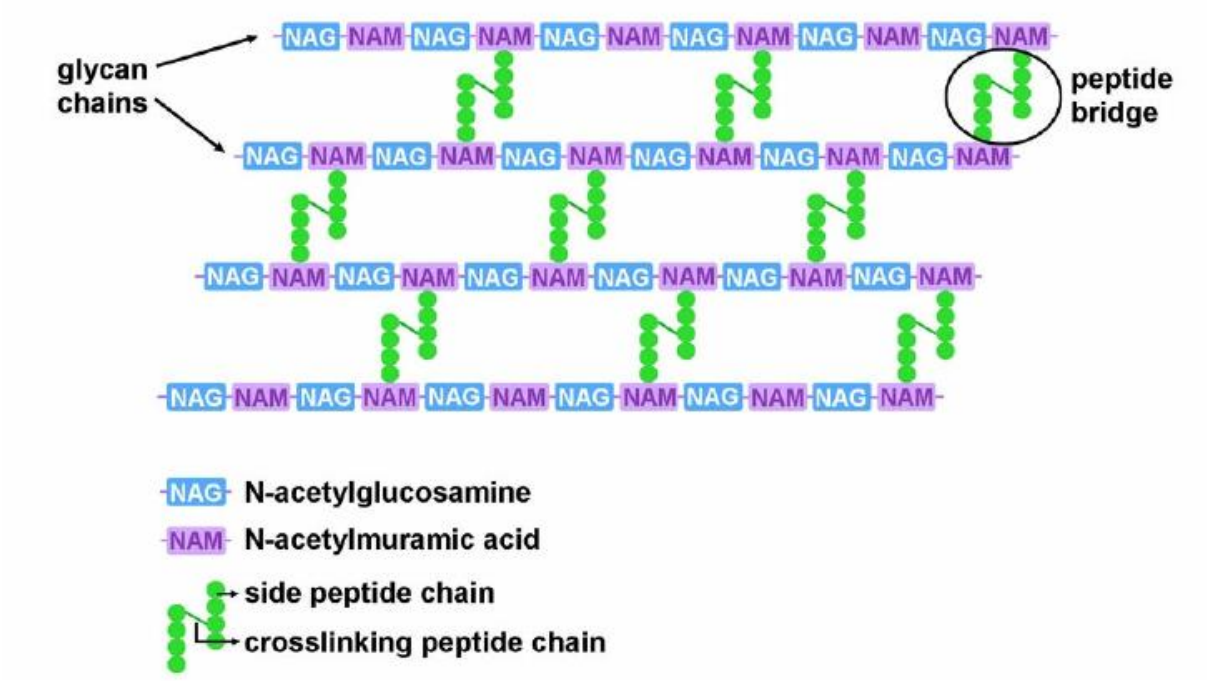

Figure 4.19 Schematic diagram of the peptidoglycan structure showing the peptide bonds and the glycan chains (Maliničová *et al.*, 2010)

4.2.1 Peptide Bonds

D-alanine

- In a single amino acid, D-alanine (symbol D-ala), as shown in Figure 4.20, consists of two groups: an amine group and a carboxylic acid group with a methyl group attached to the central carbon atom. This amino acid exists as a zwitterion under biological conditions. The amine group is protonated as $-NH_3^{+,}$ whiles the carboxyl group is deprotonated as $-CO_2^-$. It is worth noting that rarely are methyl groups directly involved in protein function due to their non-reactivity.

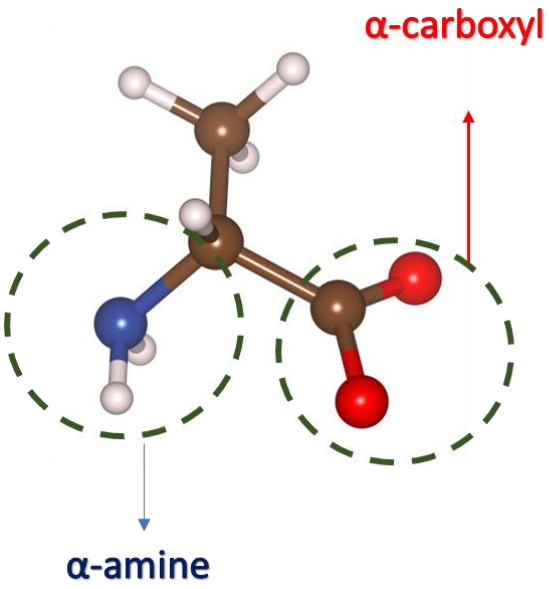

Figure 4.20 The model of the D-alanine amino acid, modeled with the Avogadro Software and visualized in Vesta with the carbon atoms in brown, nitrogen atoms in blue, oxygen atoms in red and the hydrogen atoms in white.

D-isoglutamic acid

- D- isoglutamine or D-isoglutamic acid (symbol D-isoGlu) is a gamma-amino acid formed from the amidation of the a-carboxyl of glutamic acid.

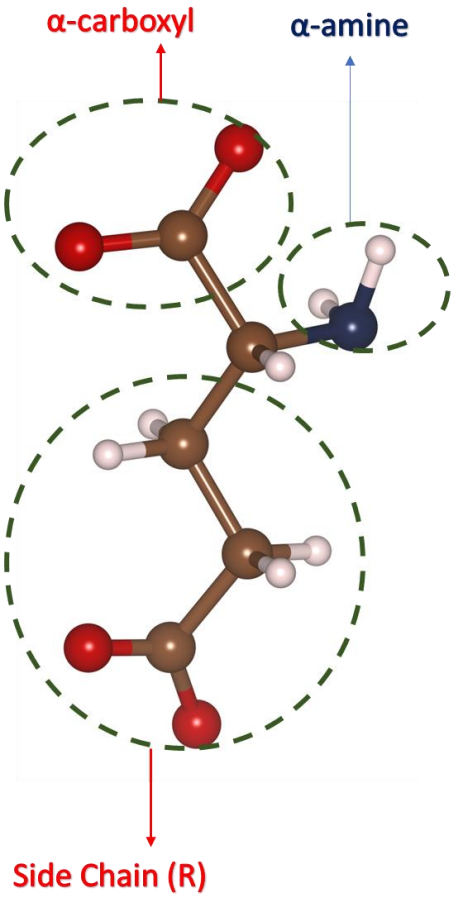

Figure 4.21 The model of the D-isoGlu amino acid, modelled with the Avogadro software and visualized in Vesta with carbon atoms in brown, nitrogen in blue, oxygen in red, and hydrogen in white.

Meso-diaminopimelic acid

- Meso-diaminopimelic acid (mA_2pm) is an epsilon-carboxy derivative of lysine. The amino acid lysine possesses three groups: an amino group, a carboxylic acid group, and a side chain lysyl group ($(CH_2)4NH_2$). Under biological conditions, the α-amino group is in the protonated $-NH_3^+$ form, whiles the α-carboxylic acid group is in the deprotonated $-COO^-$ form.

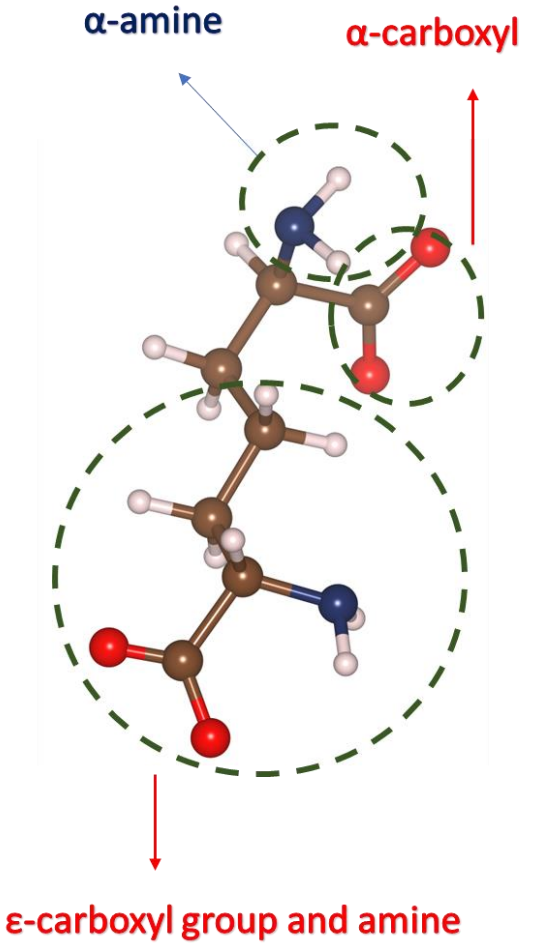

Figure 4.22 The Ma2pm amino acid model, modelled with the Avogadro software and visualized in Vesta with the carbon atoms in brown, nitrogen in blue, oxygen in red, and hydrogen in white.

4.2.2 Glycan Chains

N-acetylglucosamine

- N-acetylglucosamine (GlcNac), as the name implies, is the acetylated form of glucosamine. Glucosamine is a monosaccharide with an amino group replacing one of its hydroxyl groups. GlcNac is considered the second most abundant carbohydrate after cellulose.

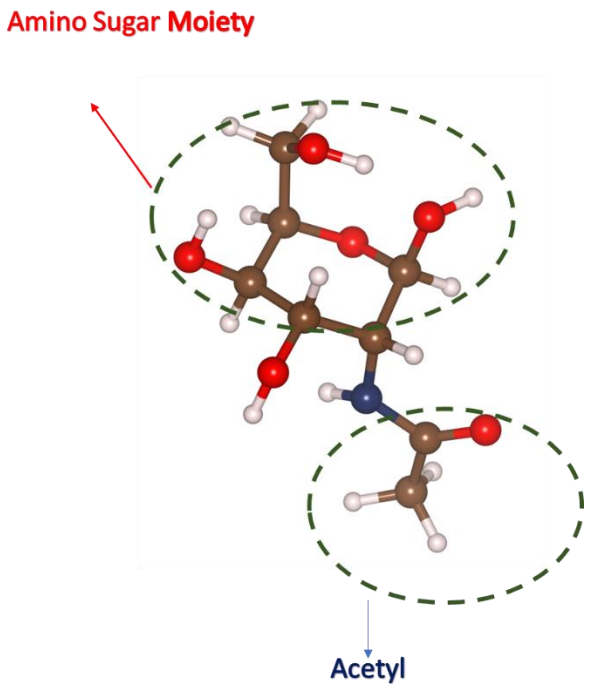

Figure 4.23 GlcNac model showing the amino sugar moiety and the acetyl group with the carbon atoms in brown, nitrogen in blue, oxygen in red, and hydrogen in white

N-acetylmuramic acid

- N-Acetylmuramic acid (MurNAc) is an amino sugar derived from GlcNac and lactic acid. It is a monosaccharide derivative of N-acetylglucosamine. The difference between GlcNac and MurNac is the carboxyl group attached to the amino sugar moiety.

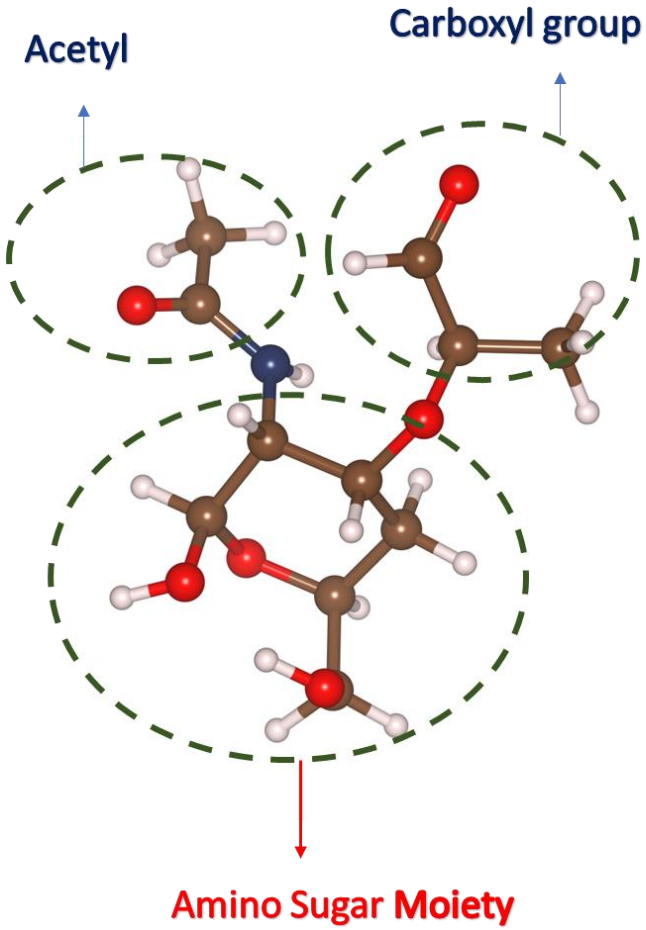

Figure 4.24 GlcNac model showing the amino sugar moiety, the acetyl group and the carboxyl group with the carbon atoms in brown, nitrogen in blue, oxygen in red, and hydrogen in white

The peptidoglycan layer's fragments (amino acids and sugars) are adsorbed on the various modelled surfaces, and the results have been described in the next section.

4.3 Interaction between the Peptidoglycan layer of Pelotomaculum thermopropionicum on DIET Accelerants (HfO_2 and WO_2)

The composition of the peptidoglycan layer is adsorbed on the various surfaces of the diet accelerants studied in this work: HfO_2 and WO_2. The interaction between peptidoglycan and the accelerants has been studied by calculating the equilibrium configuration, substrate-

adsorbate distances, adsorption energies, nature of adsorption (chemisorption or physisorption), charge densities and electronic properties (band structures and density of states) of the amino acids and glycan units adsorbed on the substrates. Three different geometric sites of the metal oxides were explored for the adsorption process: the top of the metal, the top of the oxygen atom and the bridge site between the metal and the oxygen atom (Figure 4.25). Each amino acid is adsorbed with different orientations based on their functional groups on different geometric sites of the metal oxides (Figure 4.26). Each sugar (GlcNac and MurNac) is adsorbed with different orientations based on their functional groups on different geometric sites of the metal oxides (Figure 4.27 and Figure 4.28). Nine amino acid orientations concerning the metal oxide surfaces and nine different carbohydrate orientations have been considered. This is aimed at determining the most preferable site for adsorption.

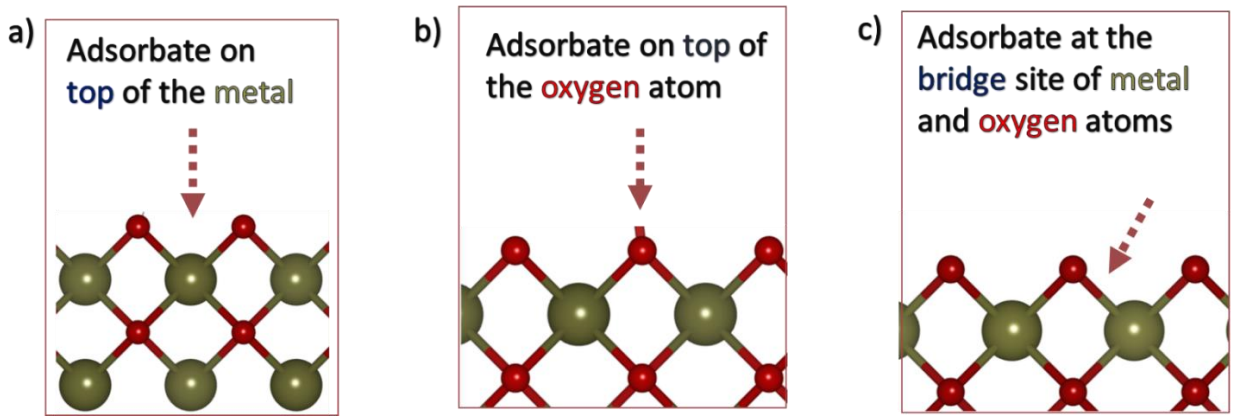

Figure 4.25 The various geometric sites of the metal oxides used for adsorption: a) adsorbate on the top side of the metal oxide (metal), b) adsorbate on the top side of the metal oxide(oxygen atom) and c) the adsorbate on the bridge site of the metal oxide

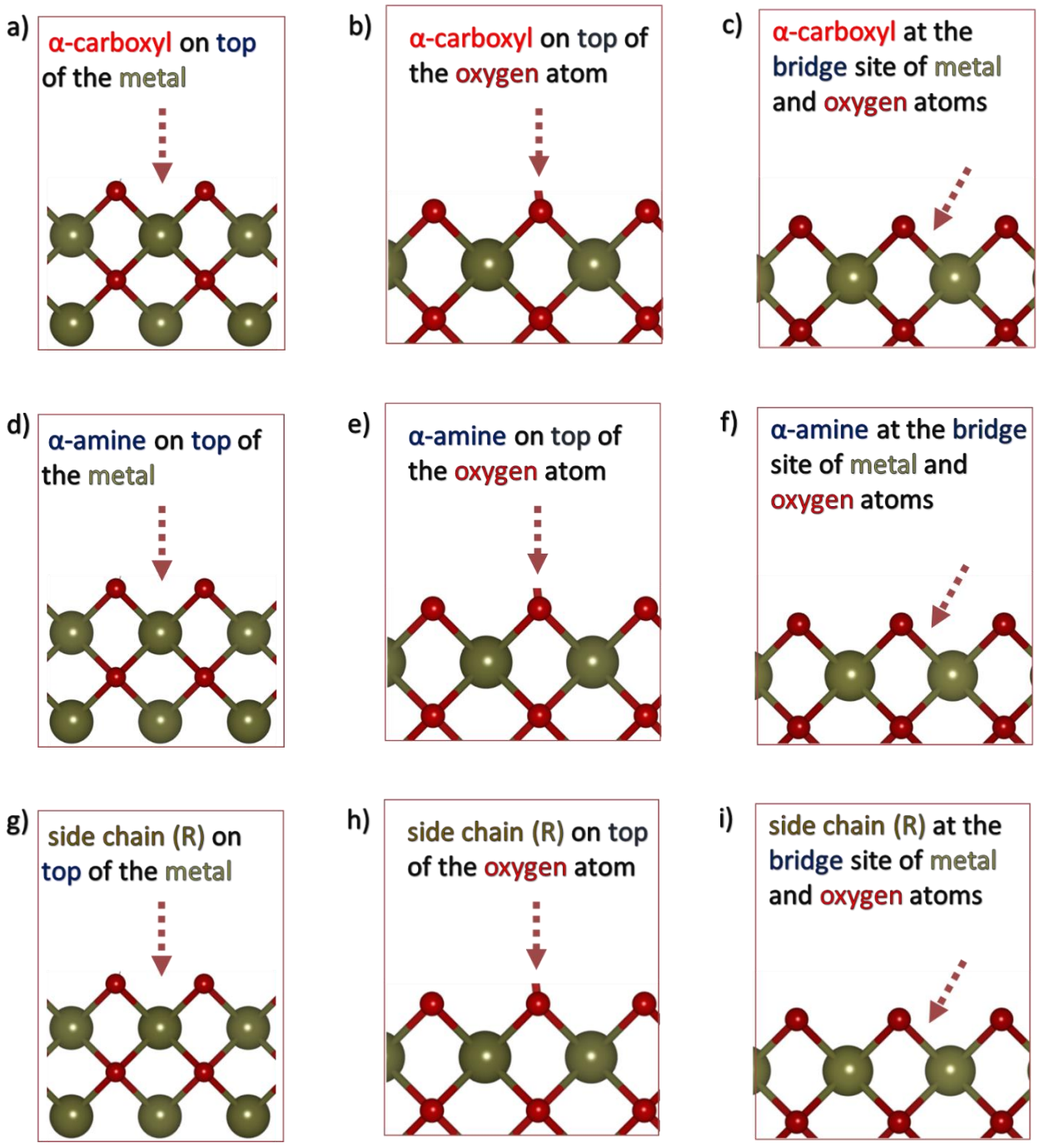

Figure 4.26 The various orientations of the amino acids used for adsorption: a) α-carboxyl on the top side of the metal oxide (metal), b) α-carboxyl on the top side of the metal oxide(oxygen atom), c) α-carboxyl on the bridge site of the metal oxide d) α-amine on the top side of the metal oxide (metal) e) α-amine on the top side of the metal oxide(oxygen atom), f) α-amine on the bridge site of the metal oxide g) side chain (R) on the top side of the metal oxide (metal) h) side chain (R) on the top side of the metal oxide(oxygen atom), i) side chain (R) on the bridge site of the metal oxide

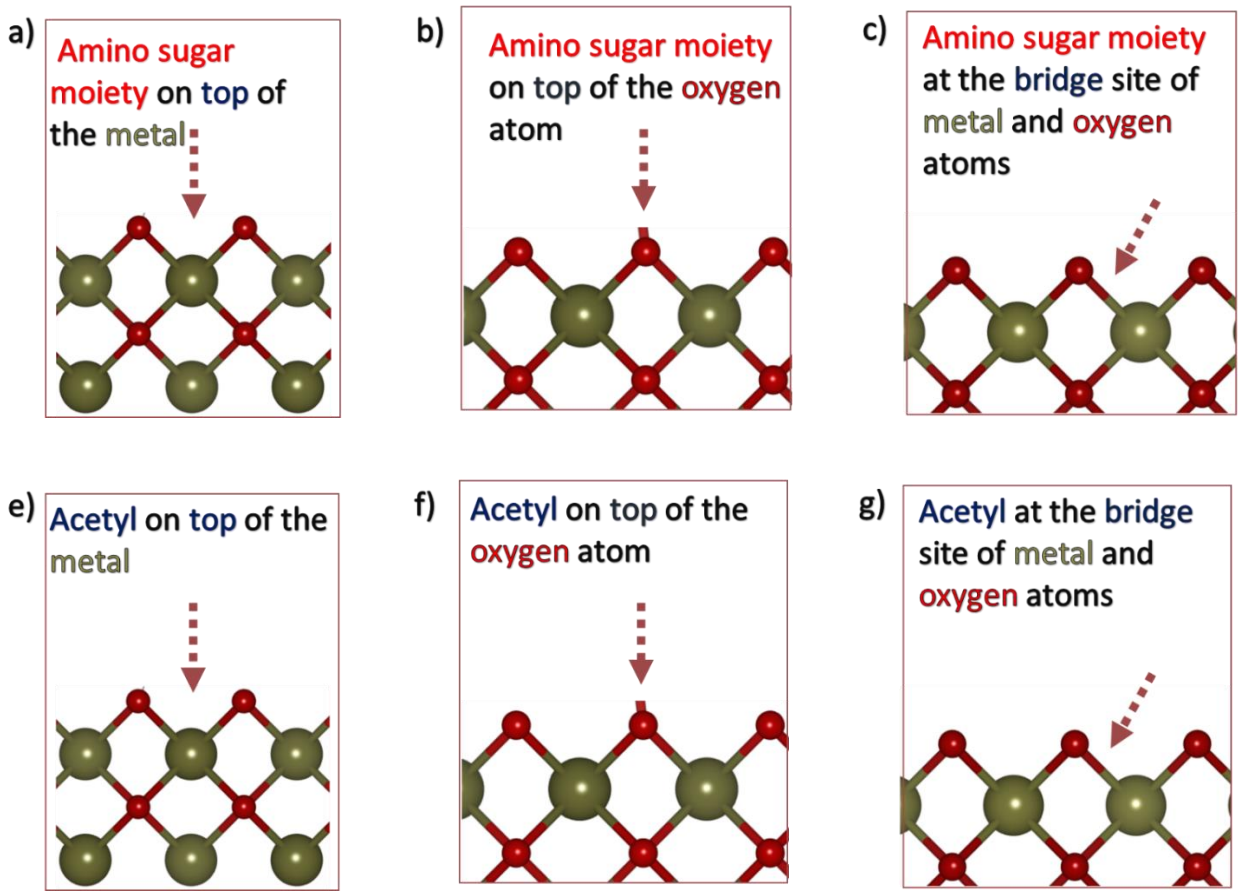

Figure 4.27 The various orientations of GlcNac used for adsorption: a) amino sugar on the top side of the metal oxide (metal), b amino sugar on the top side of the metal oxide(oxygen atom), c) amino sugar on the bridge site of the metal oxide d) acetyl on the top side of the metal oxide (metal) e) acetyl on the top side of the metal oxide(oxygen atom), f) acetyl on the bridge site of the metal oxide

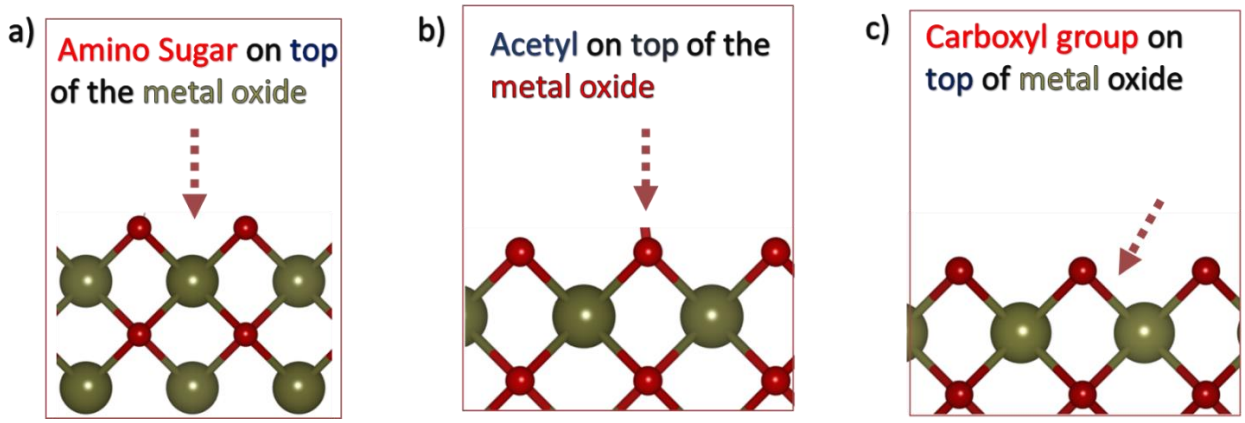

Figure 4.28 The various orientations of MurNac used for adsorption: a) amino sugar on the top side of the metal oxide, b) acetyl on top of the metal oxide, c) carboxyl on top of the metal oxide

The adsorption energies (E_{ads}) of the various complexes have been calculated according to the the following equation:

$$E_{ads} = ((E_{Surf} + E_{AA}) - E_{system})$$

Where E_{surf} and E_{AA} are the energies of the metal oxide supercells and peptidoglycan layer independently relaxed, E_{system} is the total energy of the fully optimized substrate-adsorbate. The adsorption energies in electronvolts and electronic properties (density of states) are presented and discussed below.

- **Adsorption of D-alanine (D-ala) on the monoclinic HfO_2 (100) surface.**

The optimized structures of the complexes (D-ala on the (100) surface of HfO_2) are shown in Figures 4.29 and 4.30. Adsorption energies calculated by DFT HSE range from 0.24 to 0.26 eV for the amine group and from 0.02 to 0.30 eV for the carboxyl end.

The data gathered shows that the most preferred orientation for the adsorption of D-alanine on this surface is when the carboxyl group is adsorbed on top of the hafnium atom geometric site of the system. Upon relaxation, no bonds were seen to be cleaved, and little or no distortion was observed in the lattice of the system (HfO_2) after the complex was formed.

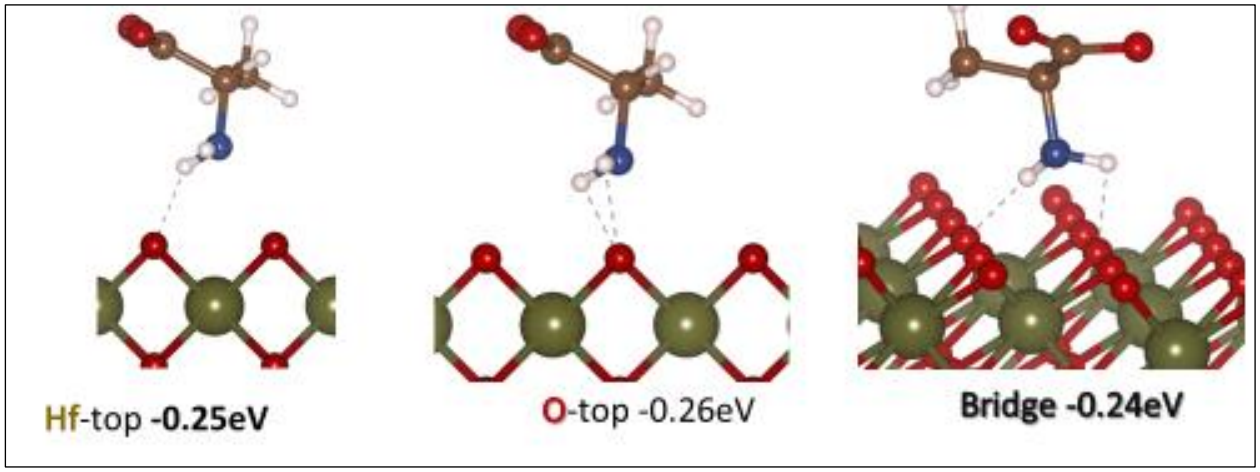

Figure 4.29 The optimized structures and adsorption energies of the amine group D-alanine on the metal top site, oxygen top site and the bridge between the metal and oxygen.

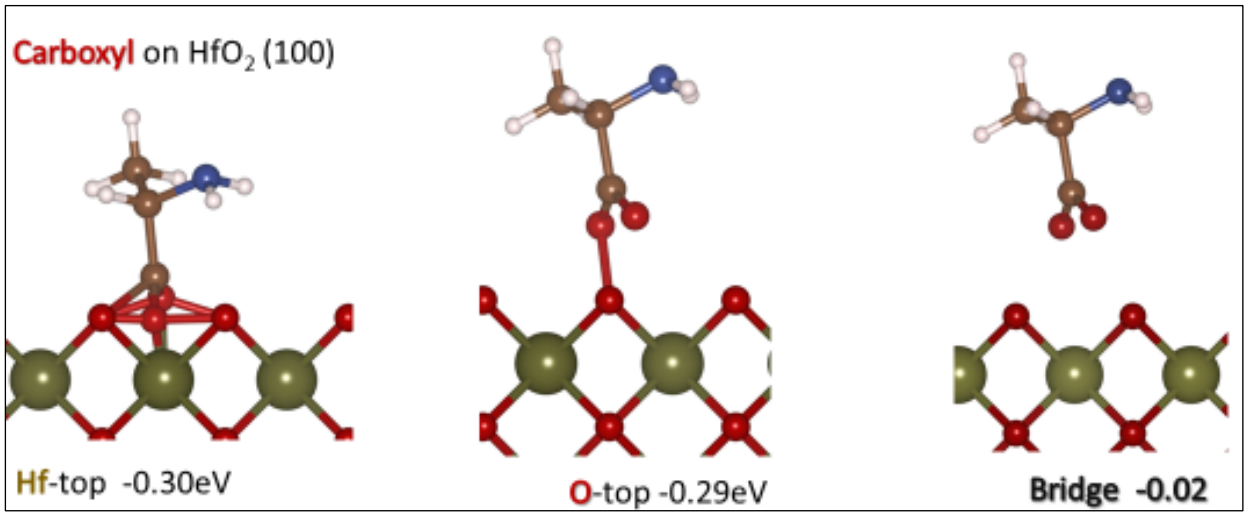

Figure 4.30 The optimized structures and adsorption energies of the carboxyl group of D-alanine on the metal top site, oxygen top site and the bridge between the metal and oxygen.

- **Adsorption of the Meso-diaminopimelic acid (Ma2pm) on the monoclinic HfO_2 (100) surface.**

The optimized structures and adsorption energies of the Ma2pm-HfO_2 complex are shown in Figures 4.31, 4.32, 4.33 and 4.34. It was found that no bonds were cleaved after relaxation. The

adsorption energies obtained for the complexes range from 0.16 to 0.56 eV. The adsorption of the amine group B on top of the hafnium atom is the most preferred, with an adsorption energy of 0.56 eV.

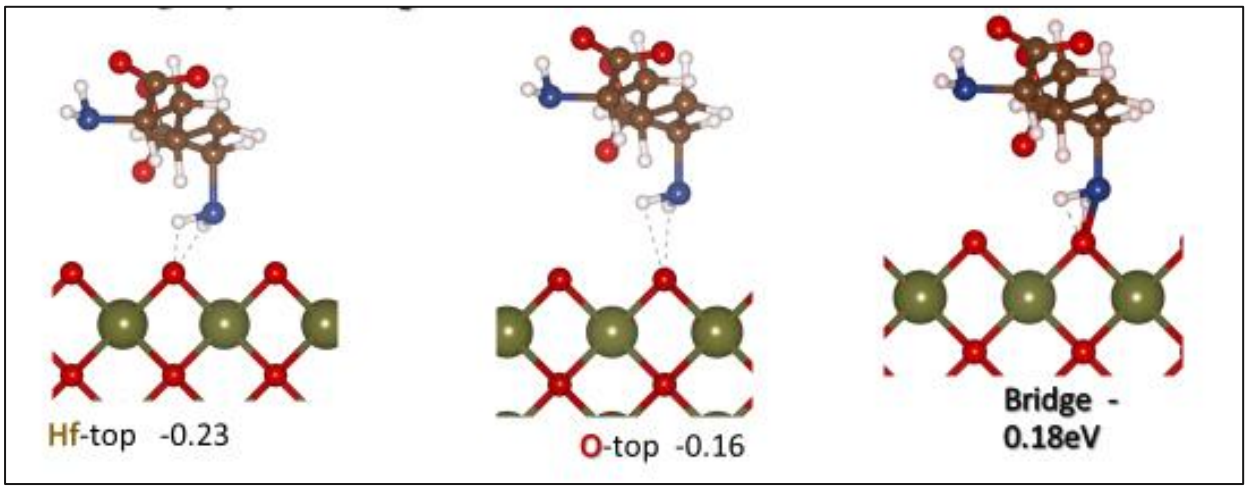

Figure 4.31: The optimized structures and adsorption energies of the amine A group of Ma2pm on the metal top site, oxygen top site and the bridge between the metal and oxygen

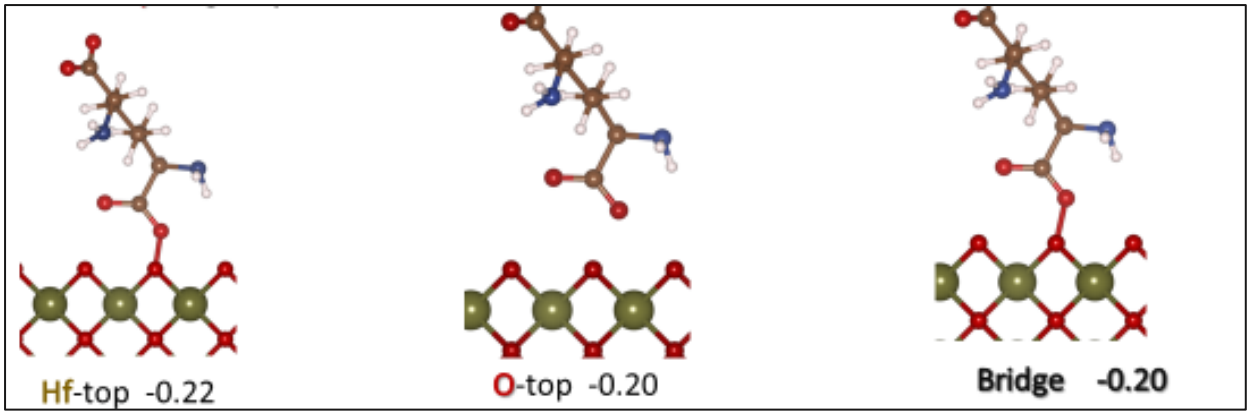

Figure 4.32: The optimized structures and adsorption energies of the carboxyl A group of Ma2pm on the metal top site, oxygen top site and the bridge between the metal and oxygen.

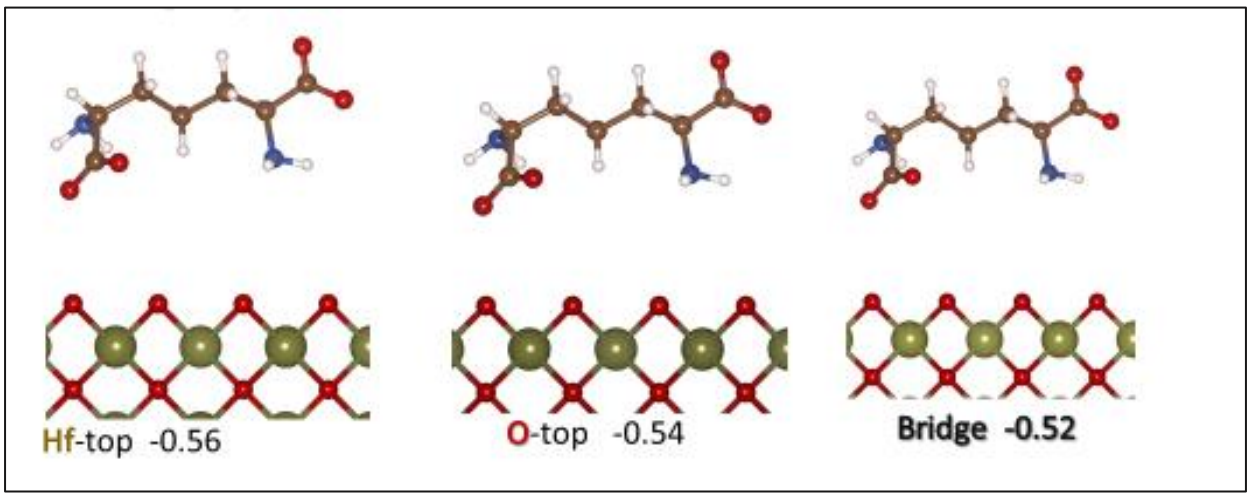

Figure 4.33: The optimized structures and adsorption energies of the amine B group of Ma2pm on the metal top site, oxygen top site and the bridge between the metal and oxygen

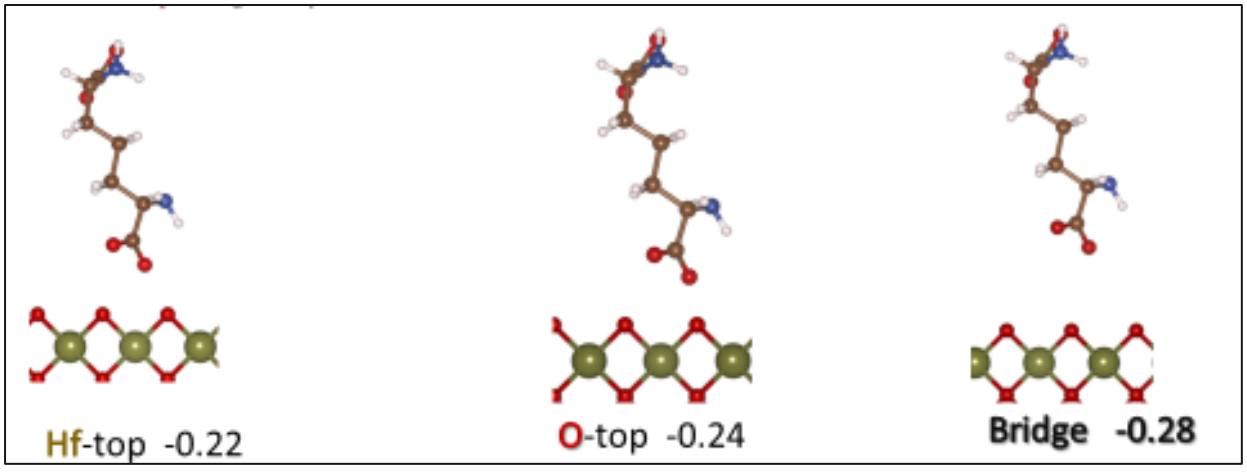

Figure 4.34: The optimized structures and adsorption energies of the carboxyl B group of Ma2pm on the metal top site, oxygen top site and the bridge between the metal and oxygen

- **Adsorption of N-Acetylglucosamine (GlcNac) on the monoclinic HfO_2 (100) surface.**

Figures 4.35 and 4.36 illustrate the GlcNac structures on the HfO_2 complex after relaxation and their corresponding adsorption energies. These energies range from -0.41 to -0.57 eV. The adsorption of the amino sugar moiety on top of the oxygen atom of the system is the most preferred.

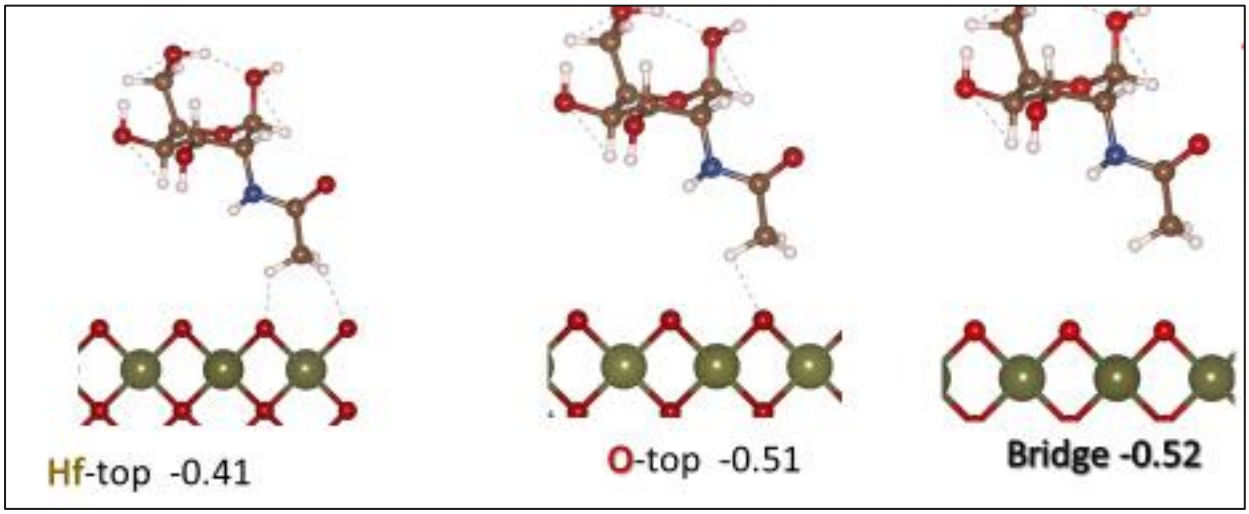

Figure 4.35: The optimized structures and adsorption energies of the Acetyl group of GlcNac on the metal top site, oxygen top site and the bridge between the metal and oxygen

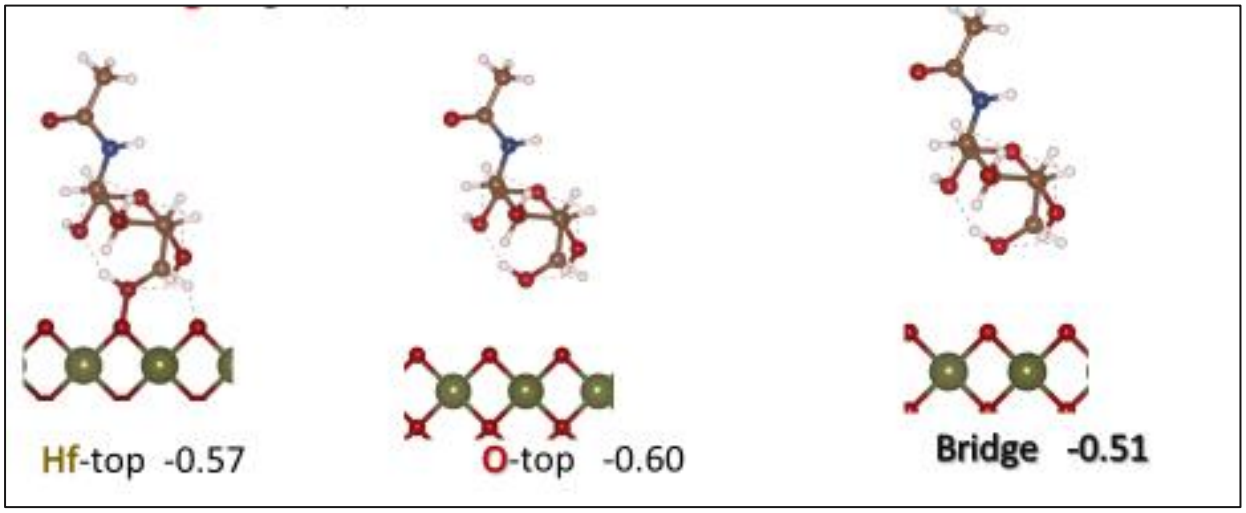

Figure 4.36: The optimized structures and adsorption energies of the Amino sugar of GlcNac on the metal top site, oxygen top site and the bridge between the metal and oxygen

- **Adsorption of N-acetylmuramic acid (NAM /MurNac) on the monoclinic HfO_2 (100) surface.**

The optimized structures of the complexes (NAM on the (100) surface of HfO_2) are shown in Figures 4.37 and 4.38. The calculated adsorption energies are attached to the images. These values range from 0.65 to 0.78 eV. The data gathered shows that the most preferred orientation for the adsorption of MurNac on this surface is that of the carboxyl group. From the calculations, no bonds were seen to be cleaved after adsorption.

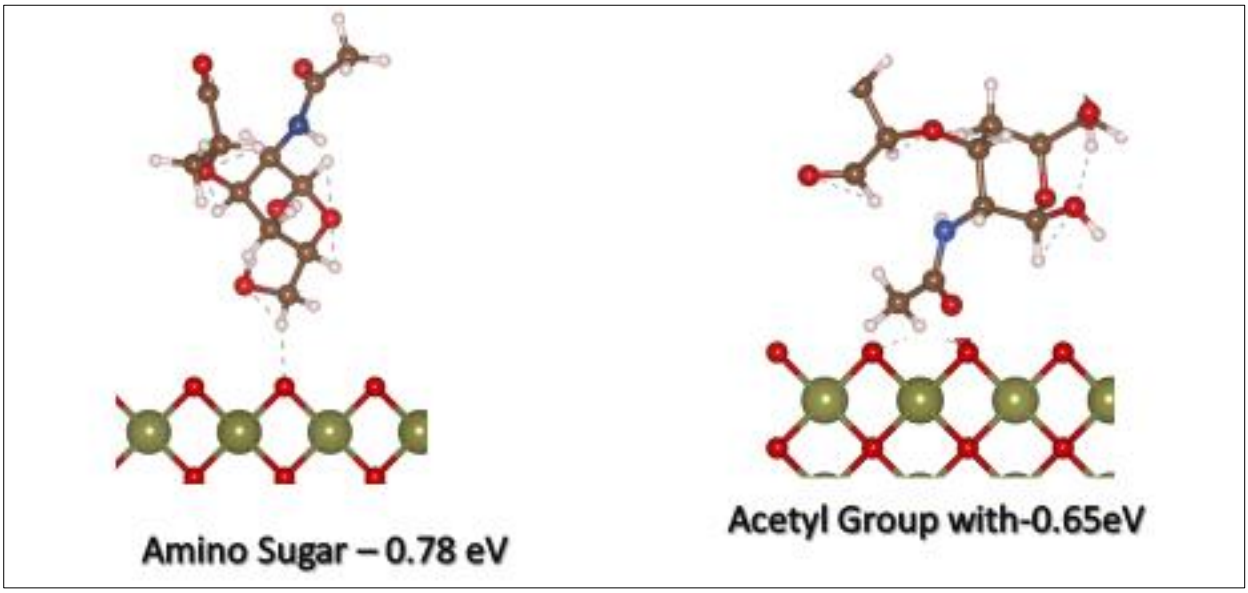

Figure 4.37: The optimized structures and adsorption energies of the Amino sugar and Acetyl group of MurNac on the top of the system

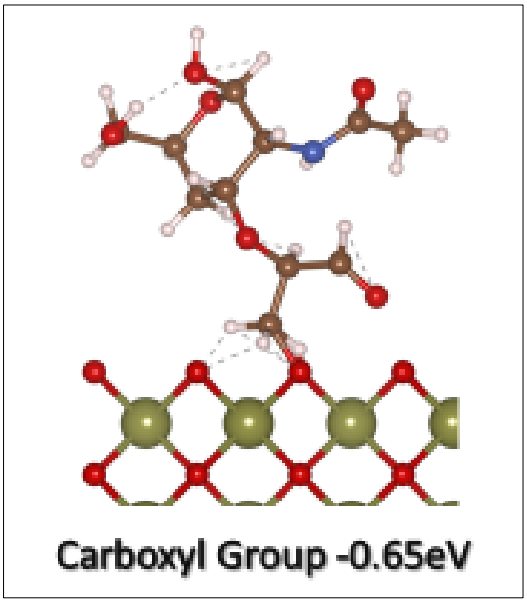

Figure 4.38: The optimized structure and adsorption energy of the carboxyl group of MurNac on the top of the system

- **Adsorption of D-ala on W-terminated (100) surface**

The optimized structures of the complexes (D-ala on the (100) surface of WO_2) are shown in Figures 4.39 and 4.40. The calculated adsorption energies range from 0.21 to 0.32 eV. The results show that the most preferred orientation for D-alanine adsorption on this surface is when the amine group is adsorbed on oxygen. Like the HfO_2 system, no bonds were seen to be cleaved after adsorption, and little or no distortion was observed in the lattice of the system (WO_2) after the complex was formed.

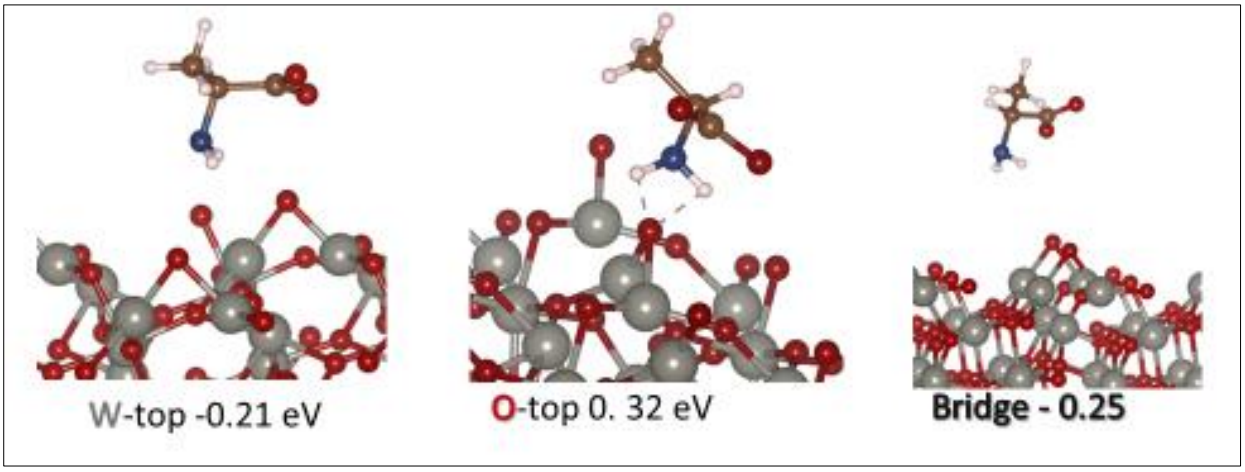

Figure 4.39: The optimized structures and adsorption energies of the amine group D-alanine on the metal top site, oxygen top site and the bridge between the metal and oxygen.

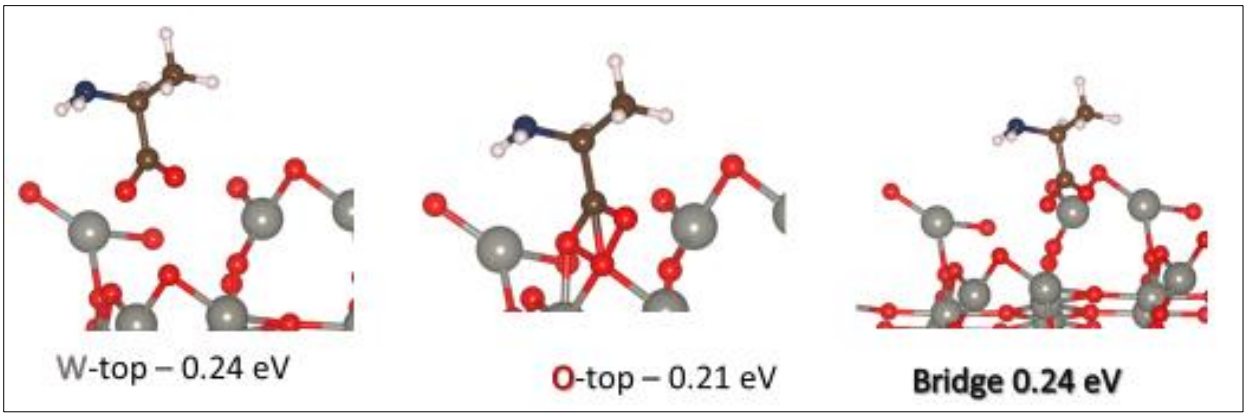

Figure 4.40: The optimized structures and adsorption energies of the carboxyl group D-alanine on the metal top site, oxygen top site and the bridge between the metal and oxygen.

- **Adsorption of D-isoGlu on W-terminated (100) surface**

D-isoGlu on the (100) surface of WO_2) has been optimized and shown in Figures 4.41-4.43. The calculated adsorption energies obtained range from 0.21 to 0.42 eV. The data gathered shows that the most preferred orientation for the adsorption of D-isoGlu on this surface is when the amine group is adsorbed on the oxygen atom of the metal oxide.

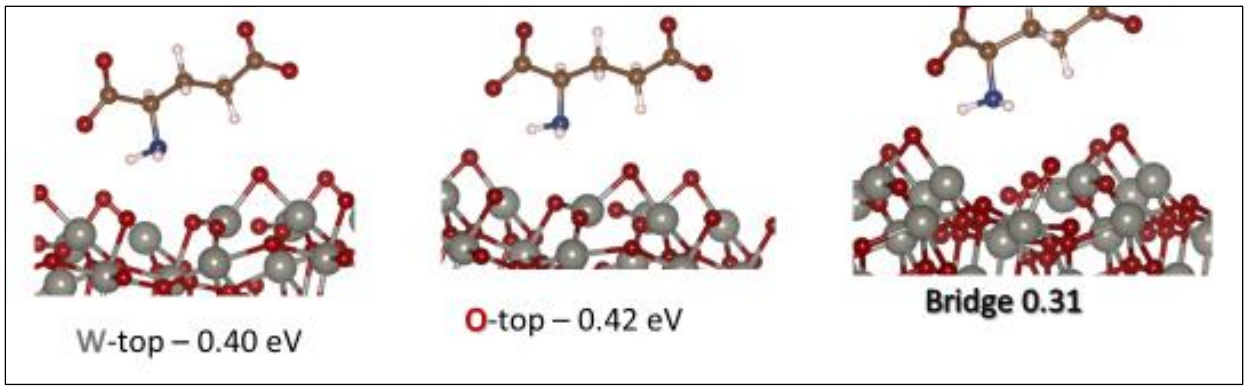

Figure 4.41: The optimized structures and adsorption energies of the amine group of D-isoGlu on the metal top site, oxygen top site and the bridge between the metal and oxygen

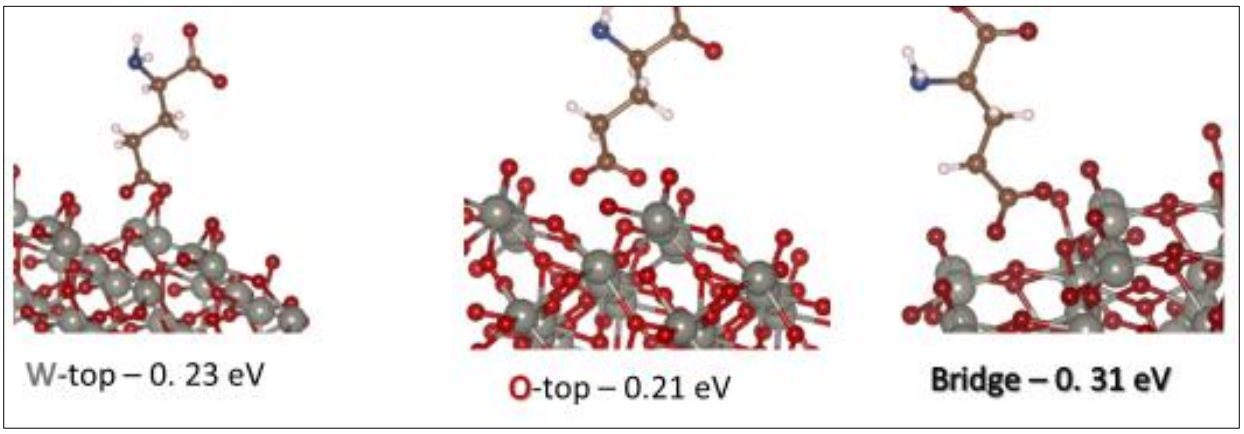

Figure 4.42: The optimized structures and adsorption energies of the carboxyl A group of D-isoGlu on the metal top site, oxygen top site and the bridge between the metal and oxygen

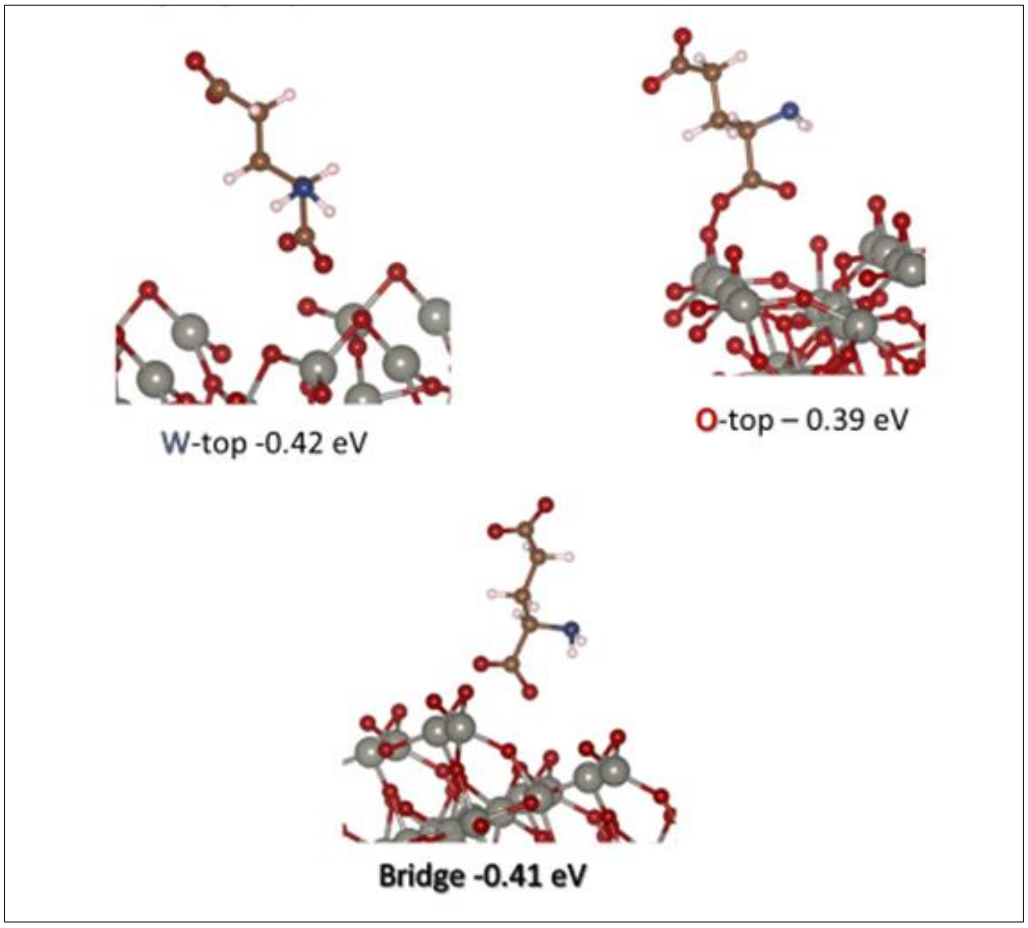

Figure 4.43: The optimized structures and adsorption energies of the carboxyl B group of D-isoGlu on the metal top site, oxygen top site and the bridge between the metal and oxygen

- **Adsorption of Ma2pm on W-terminated (100) surface**

Upon relaxation, the calculated adsorption energies obtained for the Ma2pm on the (100) surface of WO_2 ranged from 0.62 to 0.82 eV (see Figures 4.44-4.47). It is shown that the amino acid binds more strongly to the metal oxide via a carboxyl group on metal orientation.

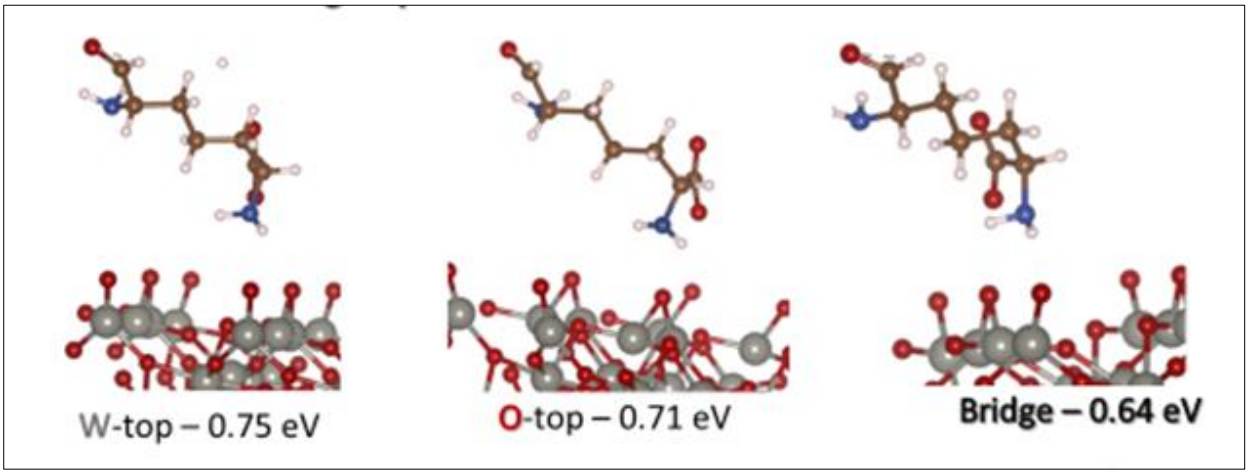

Figure 4.44: The optimized structures and adsorption energies of the amine A group of Ma2pm on the metal top site, oxygen top site and the bridge between the metal and oxygen

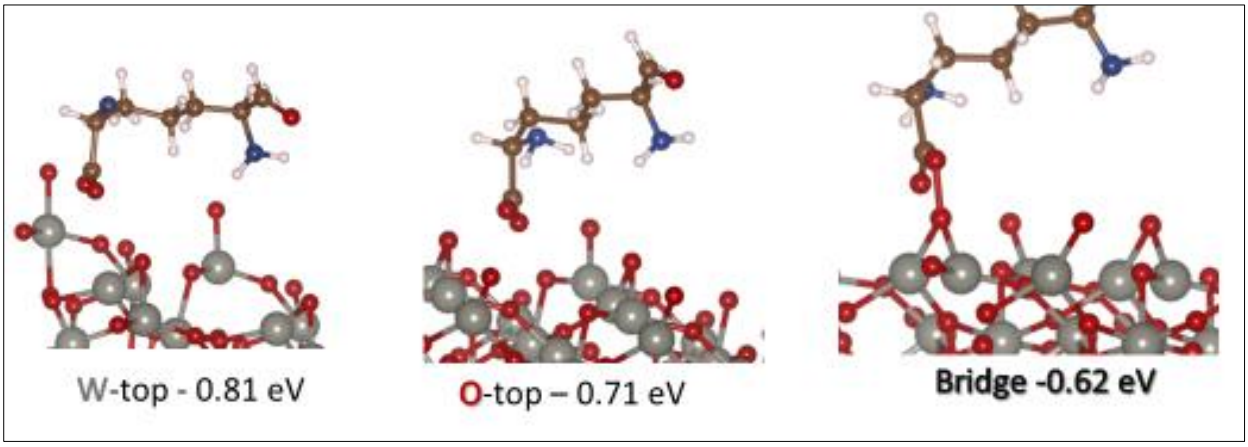

Figure 4.45: The optimized structures and adsorption energies of the carboxyl A group of Ma2pm on the metal top site, oxygen top site and the bridge between the metal and oxygen

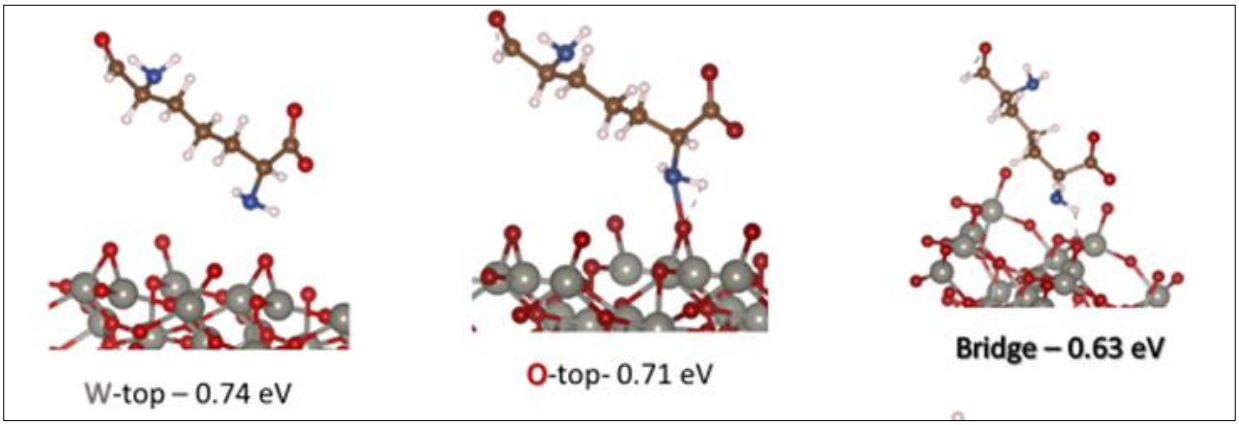

Figure 4.46: The optimized structures and adsorption energies of the amine B group of Ma2pm on the metal top site, oxygen top site and the bridge between the metal and oxygen

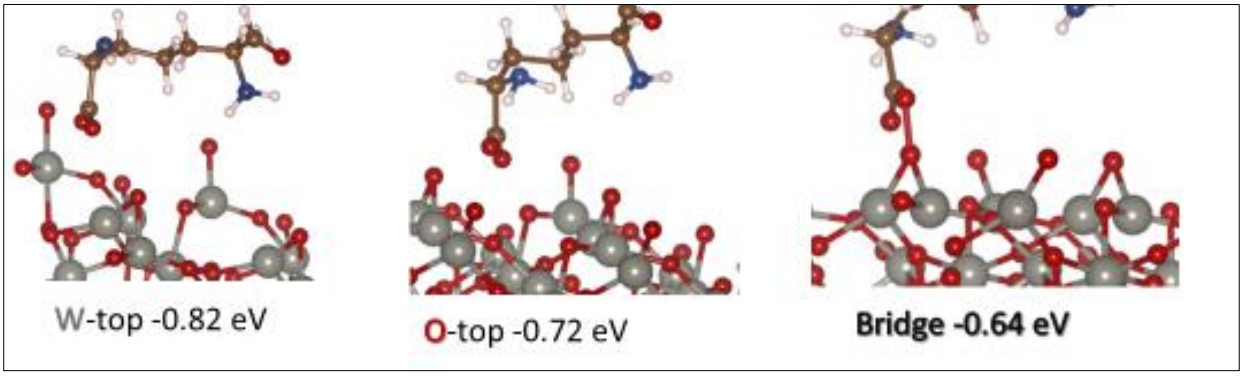

Figure 4.47: The optimized structures and adsorption energies of the carboxyl B group of Ma2pm on the metal top site, oxygen top site and the bridge between the metal and oxygen

- **Adsorption of GlcNac on W-terminated (100) surface**

The N-acetylglucosamine on W-terminated (100) surface complexes were analyzed using pure dft. The structures obtained after geometry optimization show that no visible bonds were cleaved upon forming all the complexes (Figures 4.48 and 4.49). The corresponding adsorption energies are calculated and shown in the images below. These energies range from 0.82 to 0.91

eV. It is observed that the adsorption of the carboxyl group on the tungsten atom of the system is the most preferred, with an adsorption energy of 0.91 eV.

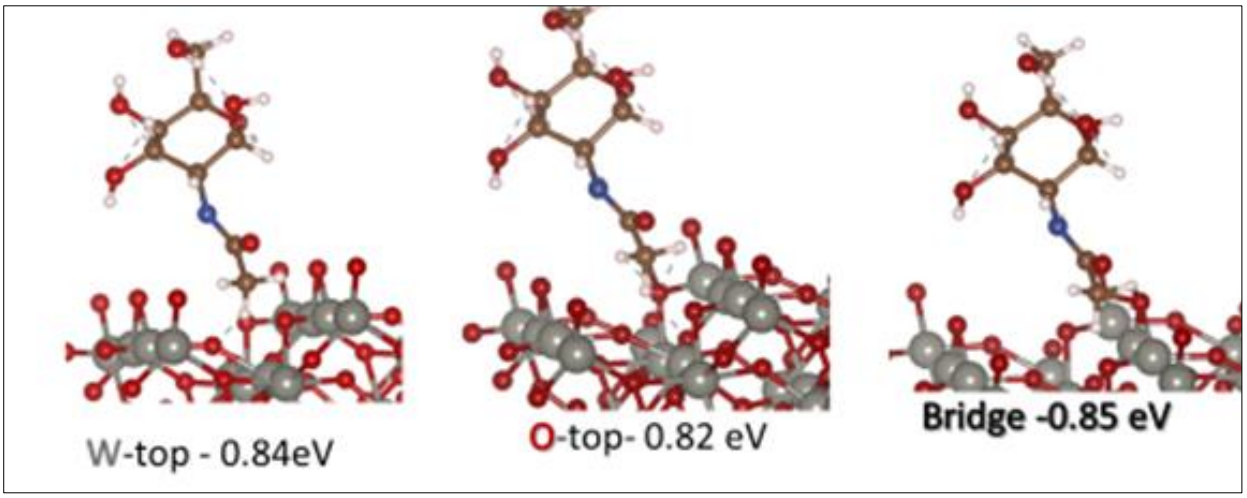

Figure 4.48: The optimized structures and adsorption energies of the Acetyl group of GlcNac on the metal top site, oxygen top site and the bridge between the metal and oxygen

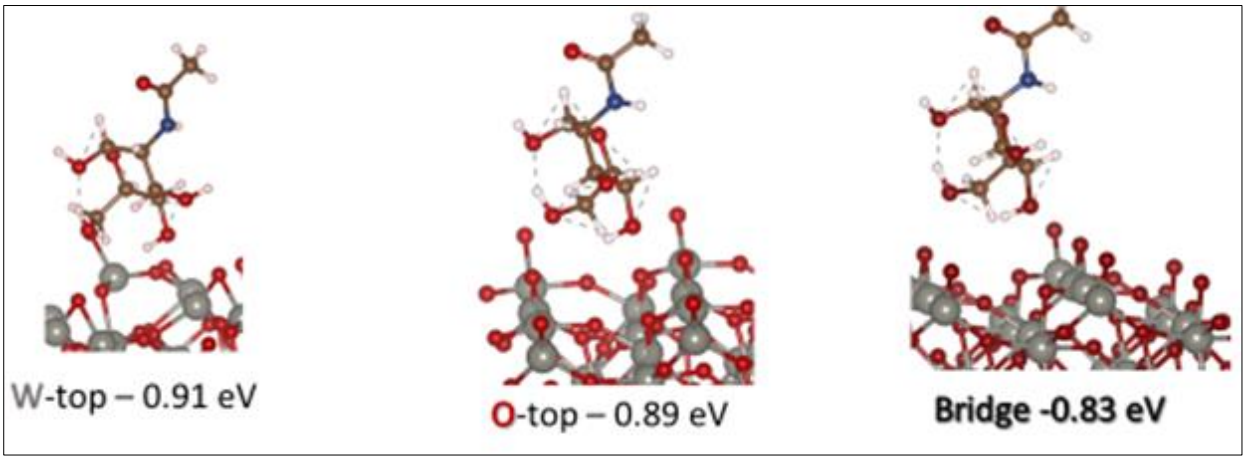

Figure 4.49: The optimized structures and adsorption energies of the carboxyl group of GlcNac on the metal top site, oxygen top site and the bridge between the metal and oxygen

- **Adsorption of MurNac/NAM on W-terminated (100) surface**

Adsorption of MurNac/NAM on the W-terminated (100) surface is optimized in Figures 4.50 and 4.51. The calculated adsorption energies of the complexes range from 0.71 eV to 1.1 eV. The amino sugar group is the most preferred orientation for the adsorption of MurNac/NAM on this surface, as the recorded adsorption energy is 1.10 eV. No bonds were observed to be cleaved in the complexes formed upon relaxation.

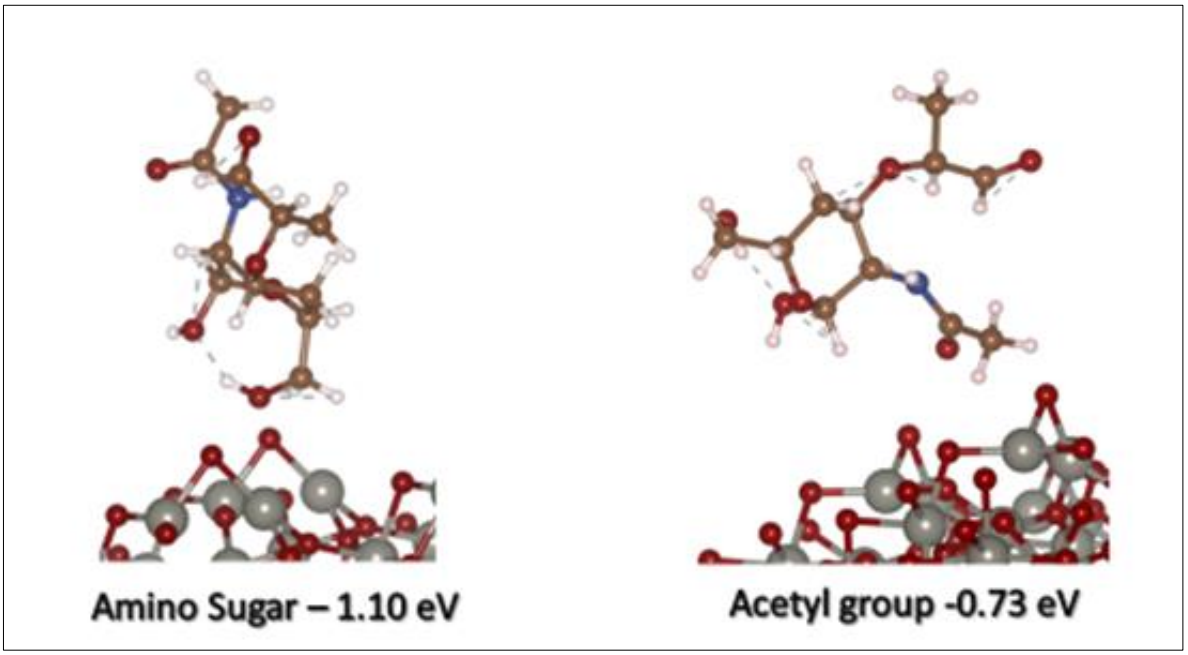

Figure 4.50: The optimized structures and adsorption energies of the Amino sugar and Acetyl group of MurNac on the top of the system.

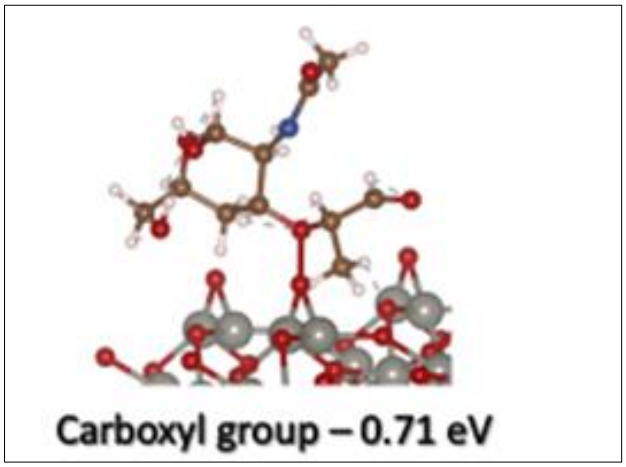

Figure 4.51: The optimized structure and adsorption energy of the carboxyl group of MurNac on the top of the system

- **Adsorption of D-ala on O-terminated (100) surface**

The D-alanine on the O-terminated (100) surface complex is optimized and shown in Figures 4.52 and 4.53. The corresponding adsorption energies are attached to these figures. The lowest adsorption energy is recorded as 0.46 eV, and the highest recorded is 0.56 eV. Thus, the most stable complex is the oxygen on the carboxyl group of D-alanine.

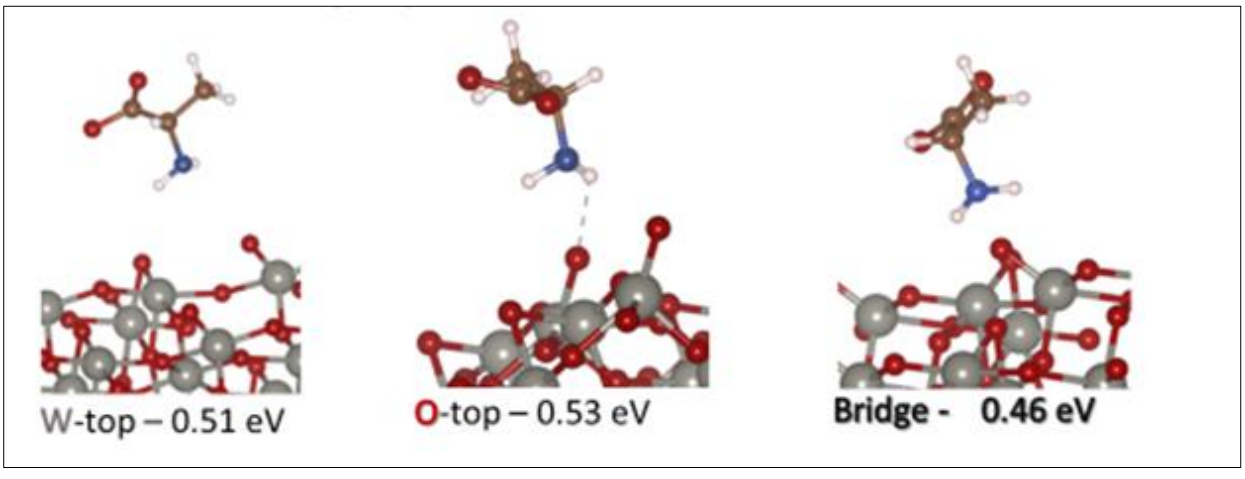

Figure 4.52:The optimized structures and adsorption energies of the amine group D-alanine on the metal top site, oxygen top site and the bridge between the metal and oxygen.

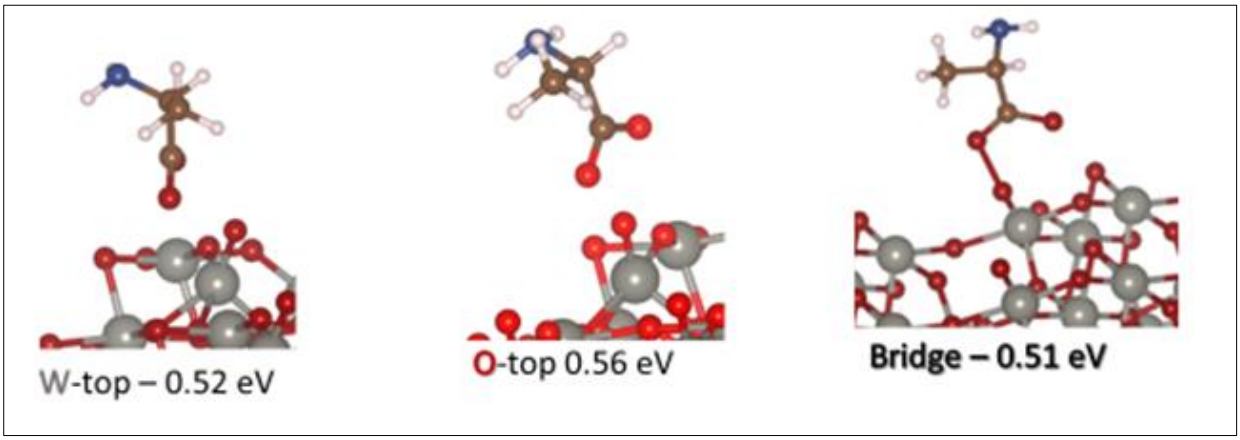

Figure 4.53:The optimized structures and adsorption energies of the carboxyl group D-alanine on the metal top site, oxygen top site and the bridge between the metal and oxygen.

- **Adsorption of D-isoGlu on O-terminated (100) surface**

Upon relaxation, the structures obtained for the D-isoGlu on the (100) surface of the WO_2 complex have been presented in Figures 4.54-4.56. The calculated adsorption energies obtained range from 0.21 eV to 0.67 eV. The data gathered shows that the most preferred orientation for the adsorption of D-isoGlu on this surface is when the carboxyl A group is adsorbed on the bridge geometric site.

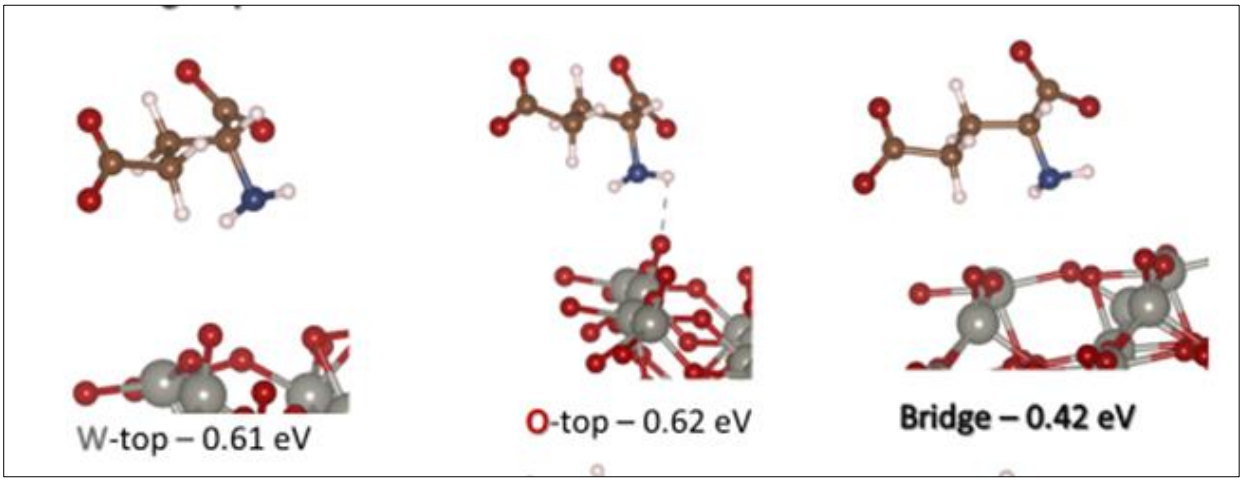

Figure 4.54:The optimized structures and adsorption energies of the amine group of D-isoGlu on the metal top site, oxygen top site and the bridge between the metal and oxygen

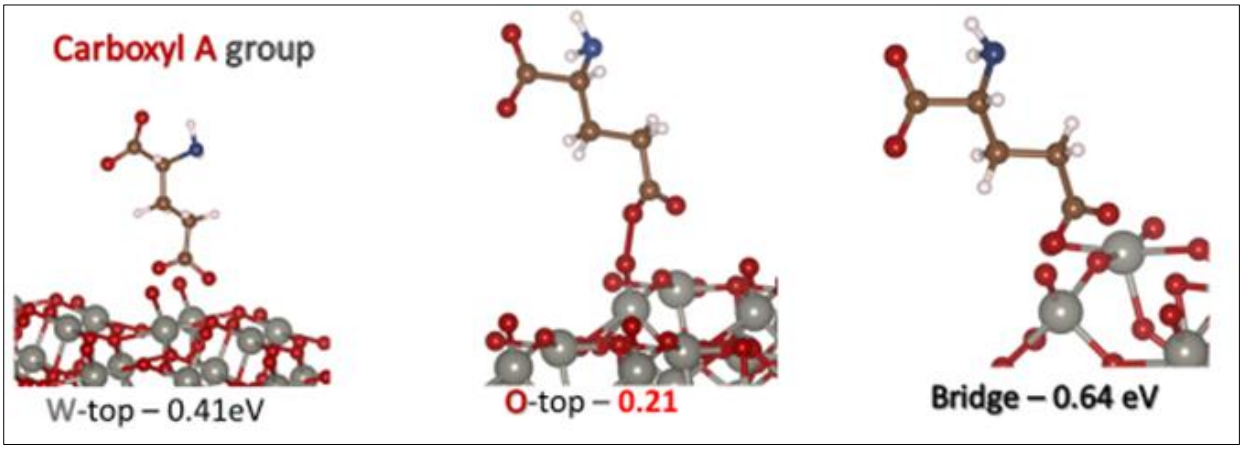

Figure 4.55: The optimized structures and adsorption energies of the carboxyl A group of D-isoGlu on the metal top site, oxygen top site and the bridge between the metal and oxygen

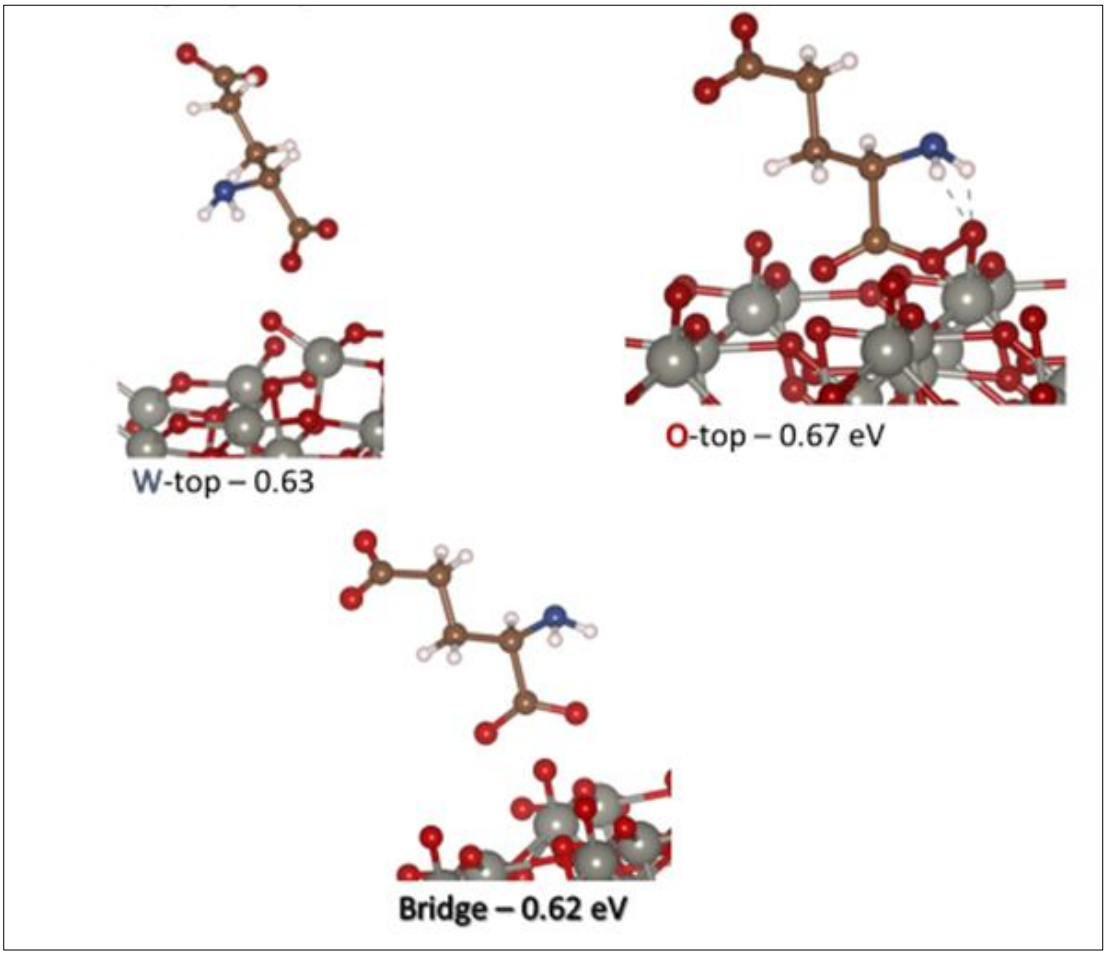

Figure 4.56:The optimized structures and adsorption energies of the carboxyl B group of D-isoGlu on the metal top site, oxygen top site and the bridge between the metal and oxygen

- **Adsorption of GlcNac on O-terminated (100) surface**

The N-acetylglucosamine fragment is adsorbed on the O-terminated (100) surface and optimized (Figures 4.48 and 4.49). The energies obtained upon adsorption range from 0.9 eV to 1.4 eV. The adsorption energies obtained show that the adsorption of the acetyl group on the top tungsten atom of the system is the most preferred.

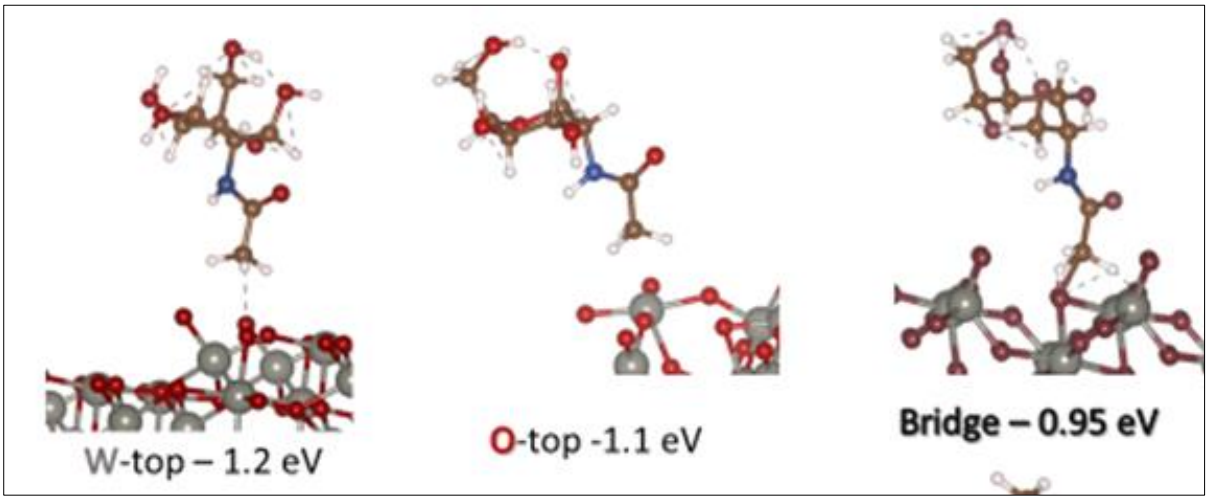

Figure 4.57: The optimized structures and adsorption energies of the Acetyl group of GlcNac on the metal top site, oxygen top site and the bridge between the metal and oxygen

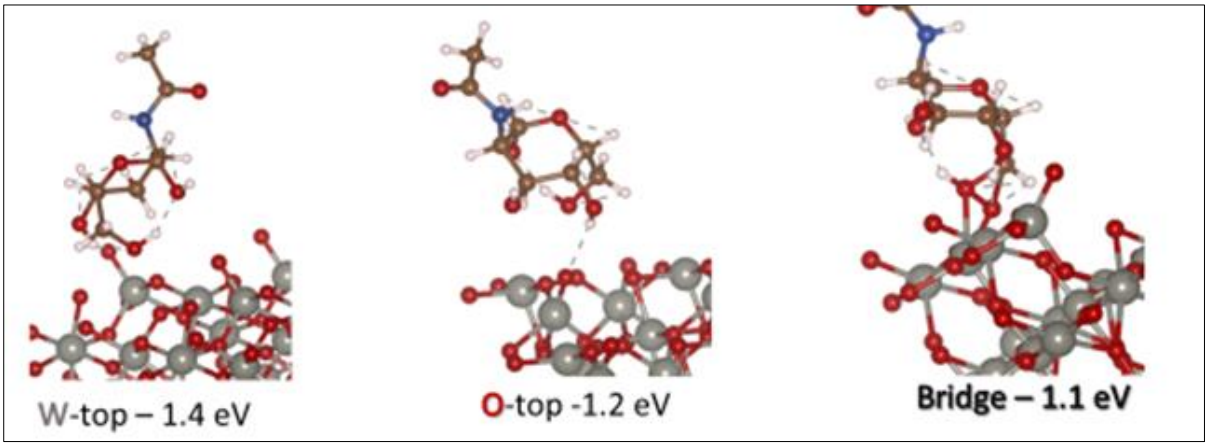

Figure 4.58: The optimized structures and adsorption energies of the carboxyl group of GlcNac on the metal top site, oxygen top site and the bridge between the metal and oxygen

- **Adsorption of MurNac on O-terminated (100) surface**

The structures of the complexes (NAM on the (100) surface of WO_2) obtained after geometry optimization are shown in Figures 4.59 and 4.60. The calculated adsorption energies (attached to the images) range from 0.8 eV to 1.4 eV. After adsorption and geometry optimization, no

bonds were observed to be cleaved. The results show that the most preferred orientation for the adsorption of MurNac/NAM on this surface is that of the acetyl group.

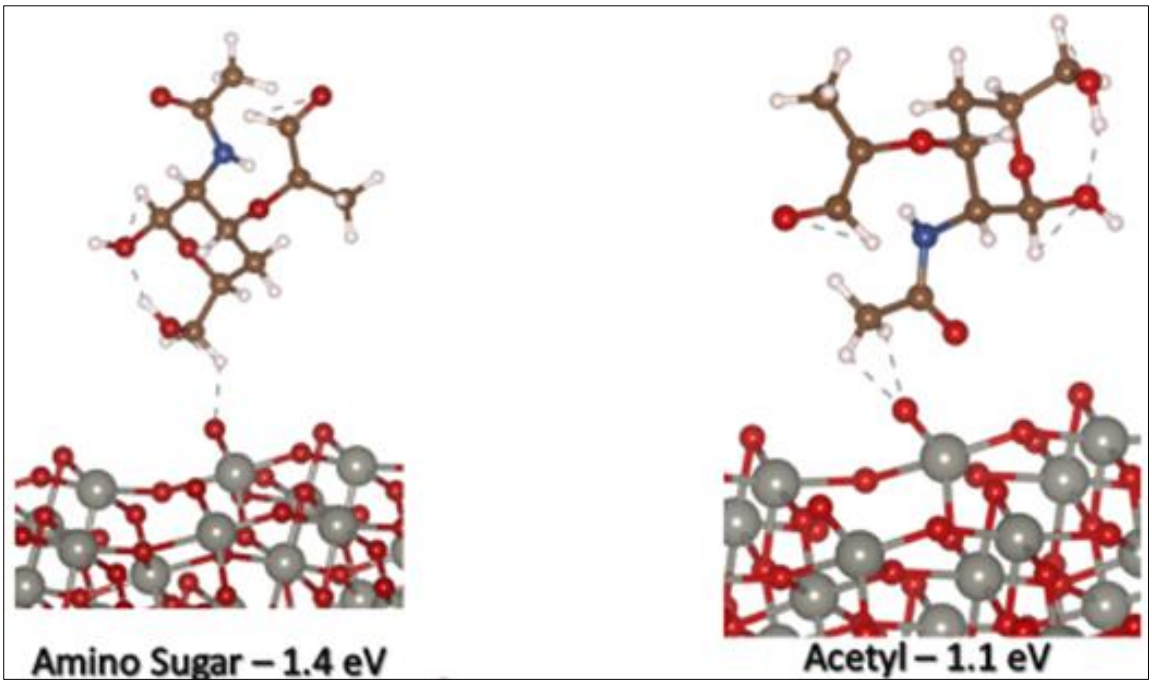

Figure 4.59: The optimized structures and adsorption energies of the Amino sugar and Acetyl group of MurNac on the top of the system.

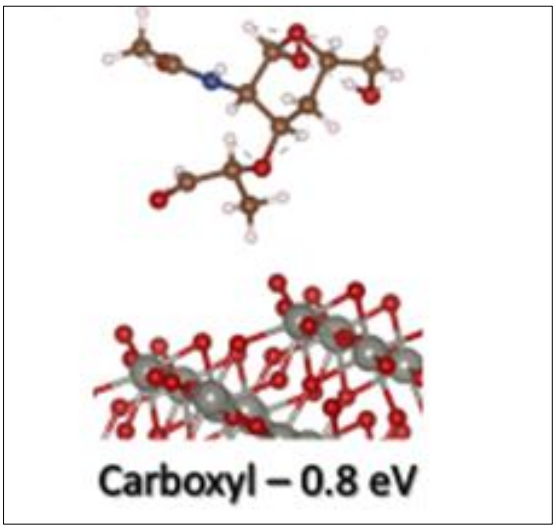

Figure 4.60: The optimized structure and adsorption energy of the carboxyl group of MurNac on the top of the system

4.4 Adsorption of Peptidoglycan Layer of Pelotomaculum thermopropionicum on DIET Inhibitors (ZnO and CuO)

- **Adsorption of D-ala on ZnO (10-10) surface**

D-alanine is adsorbed on the ZnO (10-10) surface and optimized in Figures 4.61 and 4.62. Upon relaxation, no noticeable bond cleavage has been observed. Approximately 0.9 to 1.7 eV are obtained as adsorption energies. The data gathered shows that the most preferred orientation for D-ala adsorption on this surface is when the amine group is adsorbed on the Zn atom.

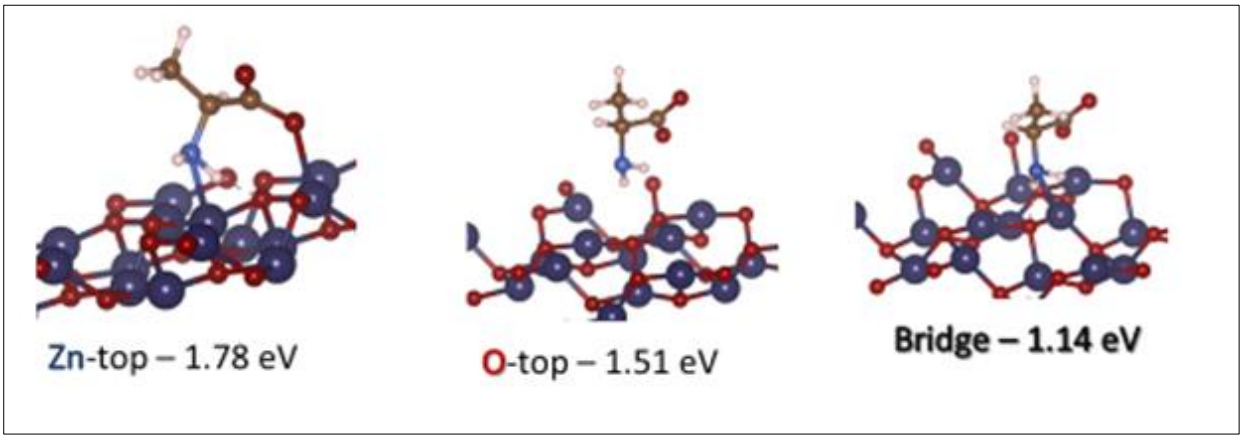

Figure 4.61: The optimized structures and adsorption energies of the amine group D-alanine on the metal top site, oxygen top site and the bridge between the metal and oxygen.

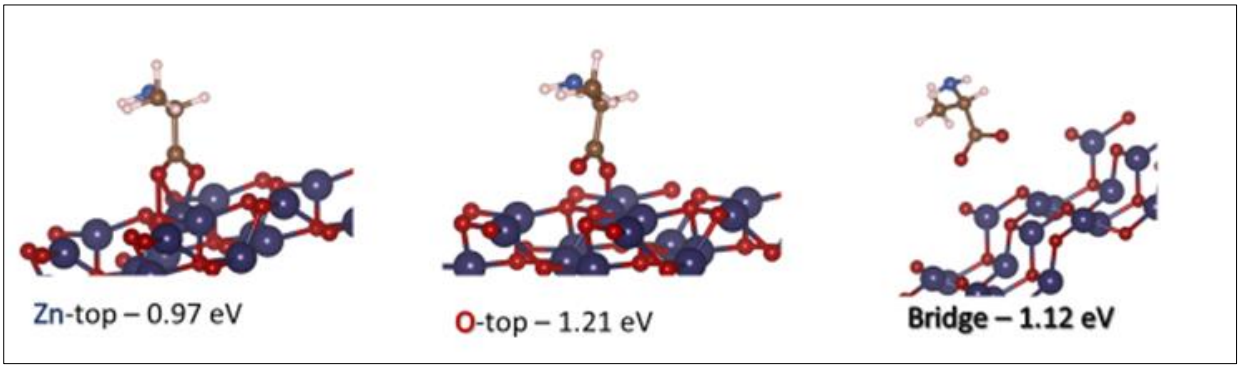

Figure 4.62: The optimized structures and adsorption energies of the carboxyl group D-alanine on the metal top site, oxygen top site and the bridge between the metal and oxygen.

- **Adsorption of D-isoGlu on ZnO (10-10) surface**

In Figures 4.63, 4.64 and 4.65, the structures obtained for the D-isoGlu on the (10-10) surface of the ZnO complex are shown upon relaxation. The calculated adsorption energies range was obtained between 1.2 eV and 1.9 eV. The data gathered shows that the most preferred orientation for the adsorption of D-isoGlu on this surface is when the carboxyl A group is adsorbed on the Zn atom.

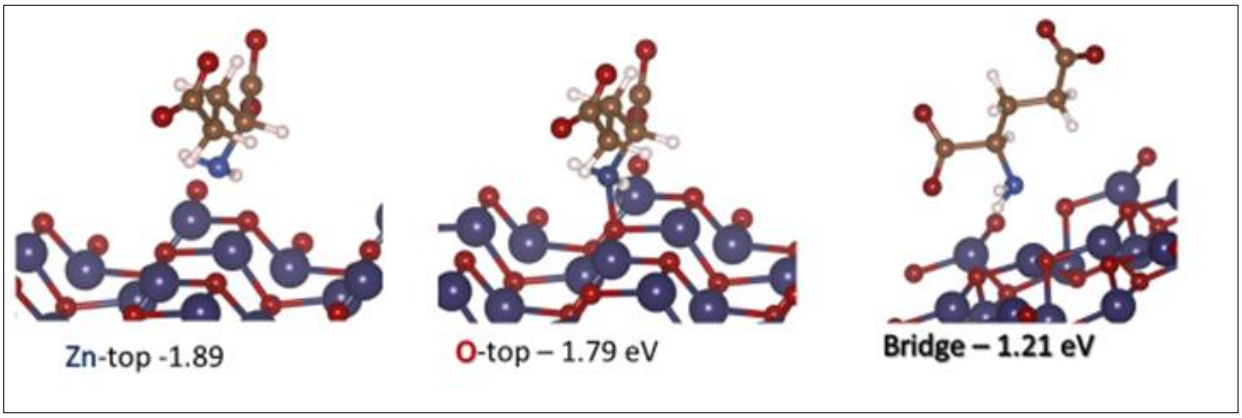

Figure 4.63: The optimized structures and adsorption energies of the amine group of D-isoGlu on the metal top site, oxygen top site and the bridge between the metal and oxygen

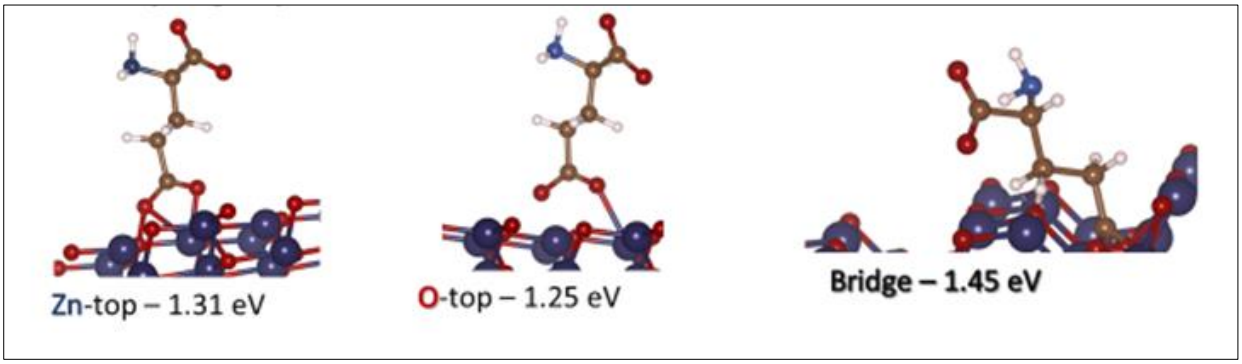

Figure 4.64: The optimized structures and adsorption energies of the carboxyl A group of D-isoGlu on the metal top site, oxygen top site and the bridge between the metal and oxygen

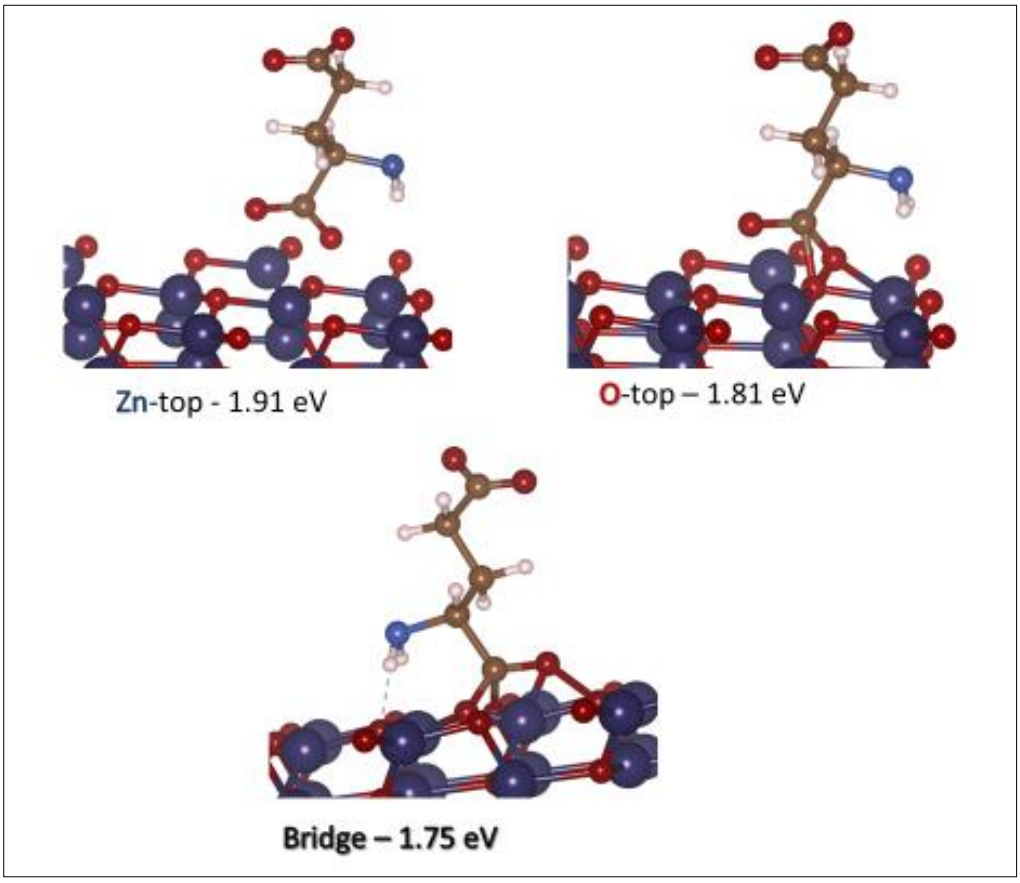

Figure 4.65: The optimized structures and adsorption energies of the carboxyl B group of D-isoGlu on the metal top site, oxygen top site and the bridge between the metal and oxygen

- **Adsorption of MurNac on ZnO (10-10) surface**

Optimized structures of the complexes (NAM on the (10-10) surface of ZnO) are shown in Figures 4.66 and 4.67. Adsorption energies have been calculated and are included with the images and range from 1.1 eV to 1.7 eV. It is worth knowing that the strongest adsorbate-to-absorbent interaction is observed in the amino sugar moiety adsorbed on the system.

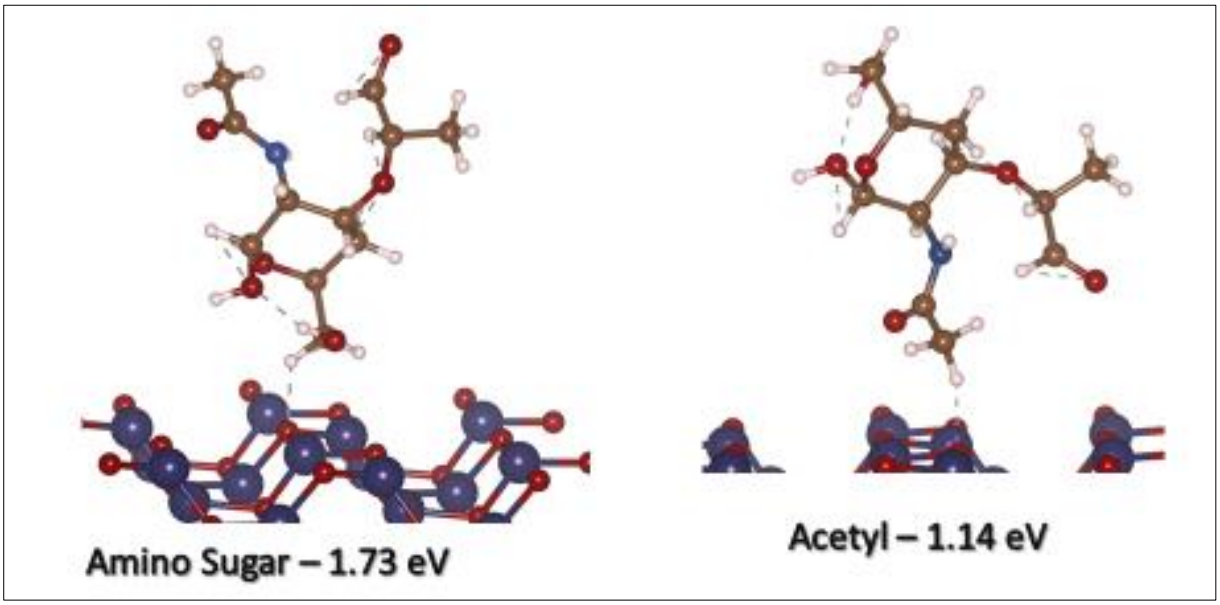

Figure 4.66: The optimized structures and adsorption energies of the Amino sugar and Acetyl group of MurNac on the top of the system.

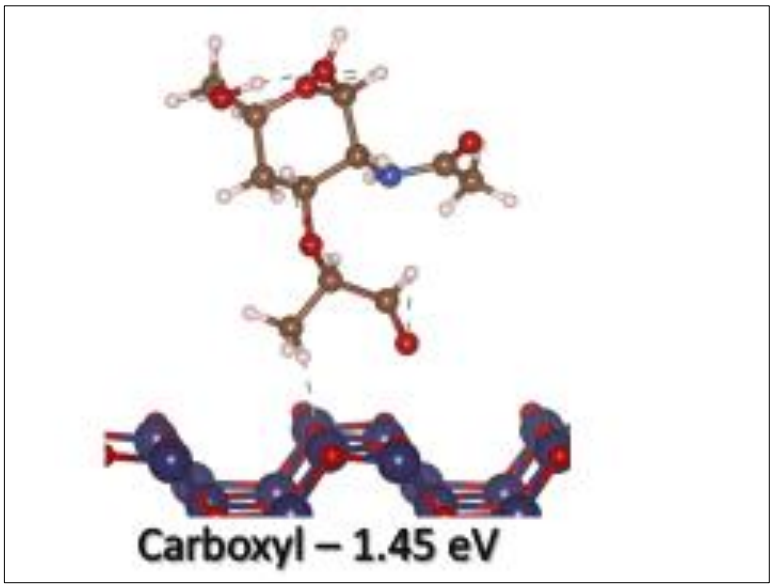

Figure 4.67: The optimized structure and adsorption energy of the carboxyl group of MurNac on the top of the system.

CHAPTER FIVE

5.0 GENERAL DISCUSSION

The electronic structure of the metal oxides plays a key role in the direct interspecies transfer of electrons in AD systems. The (100) surfaces of m-HfO_2 and m-WO_2 possess electronic structures that facilitate a simple transmission of electrons among the surfaces. A metal oxide like WO_2 allows easy transmission of electrons because of its zero-band gap. The bulk monoclinic HfO_2 system is a wide band gap insulator; the projected density of states of the modelled (100) O-terminated surface show occupancy close to the Fermi level. The nature of its electronic structure shows that the system may transmit electrons easily and thus promoting DIET. This observation could reasonably explain why this material increases biogas yield when added to AD systems.

One of the main objectives of this study was to study the interaction of the peptidoglycan layer with the metal oxides (HfO_2, WO_2, and ZnO). This was achieved by adsorbing the various components of the peptidoglycan layer of acetogenic bacteria on these metal oxides.

In all, the most favourable pathways observed for the components of the peptidoglycan layer adsorption on the active metal oxides are O-terminated surface-adsorbed systems. Particularly, the strongest binding nature was observed in the sugars (N-Acetylglucosamine and N-acetylmuramic acid) via the carboxyl group and amino sugar on the tungsten atom, whiles the weakest was observed in the carboxyl group of D-alanine on the bridge of the hafnium atom. D-alanine was the least interactive amino acid, whiles Meso-diaminopimelic acid (mA2pm) was the most interactive amino acid in all cases. Interestingly, adsorption energies increased as the number of atoms in the various adsorbates increased, and the positive adsorption energies calculated indicate the adsorption processes to be endothermic.

In inactive metal oxides (ZnO nanoparticles), the adsorption energies recorded were similar to that of the active metal oxides (0.51 eV to 1.91 eV). The inability of these materials to act as accelerants for DIET could be due to their mechano-bactericidal nature rather than their electronic nature(Gudkov *et al.*, 2021; Meghana *et al.*, 2015). These metal oxides might cause the bacteria to die off and thus inhibit DIET, reducing biogas production in practical AD settings.

In all cases, little or no distortion to the crystal lattice of the system is observed. The bonds of the materials remain intact after geometry optimization of the complexes formed.

CHAPTER SIX

6.0 CONCLUSIONS AND RECOMMENDATIONS

6.1 Conclusions

The interactions between the components of the peptidoglycan layer of Pelotomaculum thermopropionicum (acetogenic bacteria) and the transition metal oxides (HfO_2, WO_2, CuO and ZnO) have been studied using density functional theory with the HSE hybrid functional.

The results indicate that:

- The ability of a transition metal oxide to act as a direct interspecies electron transfer accelerant is based on its electronic structure. Transition metal oxides with bands close to the fermi level or with no energy gaps at the fermi level can easily transmit electrons, as seen in the case of the m-WO_2 and m-HfO_2 (110) surfaces.
- It is worth noting that the electronic structure of m-HfO_2 is different for the O-terminated surface. This feature may have contributed to its ability to transmit electrons easily to the acetogenic bacteria.
- As studied experimentally, ZnO inhibits DIET due to factors like its observed mechano-bactericidal properties. This material's electronic structure, properties, and affinity for the adsorbates may play little or no role in DIET. The nature of this material's adsorption and charge shuttling abilities may give better insights.
- The adsorption of the amino acids and sugars on the metal oxides increased with increasing number of atoms. Higher adsorption energies were recorded in N-acetylglucosamine and N-acetylmuramic acid, whiles relatively lower values were calculated for D-alanine on the metal oxides.

6.2 Recommendations

This work has provided insight into the interactions between the acetogenic bacteria's cell membrane (peptidoglycan layer) and the transition metal oxides (HfO_2, WO_2, CuO and ZnO) using density functional theory with the HSE hybrid functional. The findings from this work can be used as a guide when choosing the right transition metal oxides to boost biogas yield in an anaerobic digester or a non-ideal (real or practical) situation.

Electron conduction in bacteria may occur through direct contact using cell-surface proteins. Future studies can explore the electron transmission process in these proteins using DFT. These proteins include metalloproteins like the Multiheme c-type cytochromes (MHCs). As electron transfer proteins, multiple heme cofactors allow electrons to travel relatively long distances. Molecular docking and dynamics studies can also provide insights into the DIET process by studying the membrane-bound protein OmcZ behaviour. Interactions between the metal oxides and the S-layer of methanogens can also be explored to provide details about the DIET process.

REFERENCES

Abdelsalam, E., Samer, M., Attia, Y.A., Abdel-Hadi, M.A., Hassan, H.E. and Badr, Y. (2017), "Influence of zero valent iron nanoparticles and magnetic iron oxide nanoparticles on biogas and methane production from anaerobic digestion of manure", *Energy*, Vol. 120, pp. 842–853, doi: https://doi.org/10.1016/j.energy.2016.11.137.

Adamo, C. and Barone, V. (1999), "Toward reliable density functional methods without adjustable parameters: The PBE0 model", *Journal of Chemical Physics*, Vol. 110 No. 13, pp. 6158–6170, doi: 10.1063/1.478522.

Agne, M., Appel, L., Seelmann, C. and Boll, M. (2022), "Enoyl-Coenzyme A Respiration via Formate Cycling in Syntrophic Bacteria", *MBio*, American Society for Microbiology, Vol. 13 No. 1, doi: 10.1128/MBIO.03740-21.

Aklujkar, M., Krushkal, J., Dibartolo, G., Lapidus, A., Land, M.L. and Lovley, D.R. (2009), "The genome sequence of Geobacter metallireducens: Features of metabolism, physiology and regulation common and dissimilar to Geobacter sulfurreducens", *BMC Microbiology*, Vol. 9, pp. 1–22, doi: 10.1186/1471-2180-9-109.

Allmann, R., Hinek, R., Bergerhoff, G. and Brown, I.D. (2009), "ICSD—inorganic crystal structure database", *National Institute of Standards and Technology (NIST), FIZ Karlsruhe*.

Arena, U. (2012), "Process and technological aspects of municipal solid waste gasification. A review", *Waste Management*, Elsevier Ltd, Vol. 32 No. 4, pp. 625–639, doi: 10.1016/j.wasman.2011.09.025.

Baek, G., Kim, J., Kim, J. and Lee, C. (2018), "Role and potential of direct interspecies electron transfer in anaerobic digestion", *Energies*, Vol. 11 No. 1, doi: 10.3390/en11010107.

Balian, R., Bonche, P., Flocard, H. and Veneroni, M. (1981), "Time-dependent variational principle for predicting the expectation value of an observable", *Physical Reviews Letters*, Vol. 47 No. 19, pp. 1353–1356, doi: 10.1016/0375-9474(83)90686-3.

Baroni, S., De Gironcoli, S., Dal Corso, A. and Giannozzi, P. (2001), "Phonons and related crystal properties from density-functional perturbation theory", *Reviews of Modern Physics*, Vol. 73 No. 2, pp. 515–562, doi: 10.1103/RevModPhys.73.515.

Bartlett, R.J. (1981), "MANY-BODY PERTURBATION THEORY AND COUPLED CLUSTER THEORY FOR ELECTRON CORRELATION IN MOLECULES", *Physical Chemistry Chemical Physics*, Vol. 32, pp. 359–401.

Barua, S. and Dhar, B.R. (2017), "Advances towards understanding and engineering direct interspecies electron transfer in anaerobic digestion", *Bioresource Technology*, Elsevier, Vol. 244 No. August, pp. 698–707, doi: 10.1016/j.biortech.2017.08.023.

Bashyal, K., Pyles, C.K., Afroosheh, S., Lamichhane, A. and Zayak, A.T. (2018), "Empirical optimization of DFT+ U and HSE for the band structure of ZnO", *Journal of Physics: Condensed Matter*, IOP Publishing, Vol. 30 No. 6, p. 065501.

Becke, A.D. (1988), "Density-fnnctional exchange-energy approximation with correct asymptotic behavior", *Physical Review A*, Vol. 58 No. 6, pp. 3098–3100, doi: 10.1063/1.1749835.

Becke, A.D. (1993), "Density-functional thermochemistry. III. The role of exact exchange", *The Journal of Chemical Physics*, Vol. 98 No. 7, pp. 5648–5652, doi: 10.1063/1.464913.

Bonačić-Koutecký, V., Koutecký, J. and Fantucci, P. (1991), "Quantum Chemistry of Small Clusters of Elements of Groups Ia, Ib, and IIa: Fundamental Concepts, Predictions, and Interpretation of Experiments", *Chemical Reviews*, Vol. 91 No. 5, pp. 1035–1108, doi: 10.1021/cr00005a016.

Borroni-Bird, C.E. and King, D.A. (1991), "An ultrahigh vacuum single crystal adsorption microcalorimeter", *Review of Scientific Instruments*, Vol. 62 No. 9, pp. 2177–2185, doi: 10.1063/1.1142525.

Bose, S.K. (1998), "Electronic structure and related properties of metallic glasses: Linear muffin-tin orbital approach", *Metallurgical and Materials Transactions A: Physical Metallurgy and Materials Science*, Vol. 29 No. 7, pp. 1853–1863, doi: 10.1007/s11661-998-0010-8.

Broqvist, P., Alkauskas, A. and Pasquarello, A. (2009), "Hybrid-functional calculations with plane-wave basis sets: Effect of singularity correction on total energies, energy eigenvalues, and defect energy levels", *Physical Review B - Condensed Matter and Materials Physics*, Vol. 80 No. 8, pp. 1–13, doi: 10.1103/PhysRevB.80.085114.

Buah, W.K., Cunliffe, A.M. and Williams, P.T. (2007), "Characterization of products from the pyrolysis of municipal solid waste", *Process Safety and Environmental Protection*, Vol. 85 No. 5 B, pp. 450–457, doi: 10.1205/psep07024.

Cervantes, F.J., De Bok, F.A.M., Duong-Dac, T., Stams, A.J.M., Lettinga, G. and Field, J.A. (2002), "Reduction of humic substances by halorespiring, sulphate-reducing and methanogenic microorganisms", *Environmental Microbiology*, Vol. 4 No. 1, pp. 51–57, doi: 10.1046/j.1462-2920.2002.00258.x.

Chelikowsky, J.R. (2000), "Pseudopotential-density functional method applied to nanostructures", *Journal of Physics D: Applied Physics*, Vol. 33 No. 8, doi: 10.1088/0022-3727/33/8/201.

Chen, J.L., Steele, T.W.J. and Stuckey, D.C. (2018), "The effect of Fe 2 NiO 4 and Fe 4 NiO 4 Zn magnetic nanoparticles on anaerobic digestion activity", *Science of the Total Environment*, Elsevier B.V., Vol. 642, pp. 276–284, doi: 10.1016/j.scitotenv.2018.05.373.

Chen, S. and He, Q. (2015), “Persistence of Methanosaeta populations in anaerobic digestion during process instability”, *Journal of Industrial Microbiology and Biotechnology*, Springer Berlin Heidelberg, Vol. 42 No. 8, pp. 1129–1137, doi: 10.1007/s10295-015-1632-7.

Chen, Y.C. (2018), “Effects of urbanization on municipal solid waste composition”, *Waste Management*, Elsevier Ltd, Vol. 79, pp. 828–836, doi: 10.1016/j.wasman.2018.04.017.

Choi, O., Kim, T., Woo, H.M. and Um, Y. (2014), “Electricity-driven metabolic shift through direct electron uptake by electroactive heterotroph Clostridiumpasteurianum”, *Scientific Reports*, Vol. 4 No. 1, p. 6961, doi: 10.1038/srep06961.

Coester, F. and Kümmel, H. (1960), “Short-range correlations in nuclear wave functions”, *Nuclear Physics*, Vol. 17 No. C, pp. 477–485, doi: 10.1016/0029-5582(60)90140-1.

Combes, J.-M. (1977), “The Born-Oppenheimer Approximation”, *Rigorous Atomic and Molecular Physics*, pp. 139–159, doi: 10.1007/978-3-7091-7673-3_7.

Conklin, A., Stensel, H.D. and Ferguson, J. (2006), “Growth Kinetics and Competition Between Methanosarcina and Methanosaeta in Mesophilic Anaerobic Digestion”, *Water Environment Research*, Vol. 78 No. 5, pp. 486–496, doi: 10.2175/106143006x95393.

Cruz Viggi, C., Rossetti, S., Fazi, S., Paiano, P., Majone, M. and Aulenta, F. (2014), “Magnetite particles triggering a faster and more robust syntrophic pathway of methanogenic propionate degradation”, *Environmental Science and Technology*, Vol. 48 No. 13, pp. 7536–7543, doi: 10.1021/es5016789.

Cruz Viggi, C., Simonetti, S., Palma, E., Pagliaccia, P., Braguglia, C., Fazi, S., Baronti, S., *et al.* (2017), “Enhancing methane production from food waste fermentate using biochar: The added value of electrochemical testing in pre-selecting the most effective type of biochar”, *Biotechnology for Biofuels*, BioMed Central, Vol. 10 No. 1, pp. 1–13, doi: 10.1186/s13068-017-0994-7.

Desclaux, J.P. (1970), “Hartree Fock Slater self consistent field calculations”, *Computer Physics Communications*, Vol. 1 No. 3, pp. 216–222, doi: 10.1016/0010-4655(70)90008-1.

Farquhar, C.P. and Inglesfield, J.E. (1989), “An embedding method for interface electronic structure calculations”, *Journal of Physics: Condensed Matter*, Vol. 1 No. 3, pp. 599–610, doi: 10.1088/0953-8984/1/3/011.

Feng, Q., Song, Y.C., Li, J., Wang, Z. and Wu, Q. (2020), “Influence of electrostatic field and conductive material on the direct interspecies electron transfer for methane production”, *Environmental Research*, Elsevier Inc., Vol. 188 No. June, p. 109867, doi: 10.1016/j.envres.2020.109867.

Fernandez, H.C., Buffiere, P. and Bayard, R. (2022), “Understanding the role of mechanical pretreatment before anaerobic digestion: Lab-scale investigations”, *Renewable Energy*, Vol. 187, pp. 193–203, doi: 10.1016/j.renene.2022.01.067.

Fowkes, F.M. (1980), “Surface effects of anisotropic london dispersion forces in n-alkanes”, *Journal of Physical Chemistry*, Vol. 84 No. 5, pp. 510–512, doi: 10.1021/j100442a011.

Gerritse, J., Renard, V., Pedro Gomes, T.M., Lawson, P.A., Collins, M.D. and Gottschal, J.C. (1996), “Desulfitobacterium sp. strain PCE1, an anaerobic bacterium that can grow by reductive dechlorination of tetrachloroethene or ortho-chlorinated phenols”, *Archives of Microbiology*, Vol. 165 No. 2, pp. 132–140, doi: 10.1007/s002030050308.

Giannozzi, P., Baroni, S., Bonini, N., Calandra, M., Car, R., Cavazzoni, C., Ceresoli, D., *et al.* (2009), “QUANTUM ESPRESSO: a modular and open-source software project for quantum simulations of materials”, *Journal of Physics: Condensed Matter*, IOP Publishing, Vol. 21 No. 39, p. 395502.

Gilman, J.J. (1960), “Direct measurements of the surface energies of crystals”, *Journal of Applied Physics*, Vol. 31 No. 12, pp. 2208–2218, doi: 10.1063/1.1735524.

Giri, A. and Hopkins, P.E. (2020), “A Review of Experimental and Computational Advances in Thermal Boundary Conductance and Nanoscale Thermal Transport across Solid Interfaces”, *Advanced Functional Materials*, Vol. 30 No. 8, pp. 1–21, doi: 10.1002/adfm.201903857.

Gong, M. and Makowski, L. (1992), “Helical structure of P pili from Escherichia coli. Evidence from X-ray fiber diffraction and scanning transmission electron microscopy”, *Journal of Molecular Biology*, Vol. 228 No. 3, pp. 735–742, doi: 10.1016/0022-2836(92)90860-M.

Gottlieb, K., Wacher, V., Sliman, J. and Pimentel, M. (2016), “Review article: Inhibition of methanogenic archaea by statins as a targeted management strategy for constipation and related disorders”, *Alimentary Pharmacology and Therapeutics*, Vol. 43 No. 2, pp. 197–212, doi: 10.1111/apt.13469.

Greeley, J., Nørskov, J.K. and Mavrikakis, Manos. (2002), “ELECTRONIC STRUCTURE AND CATALYSIS ONMETAL SURFACES”, *Annual Review of Physical Chemistry*, Vol. 50 No. 1, pp. 79–115, doi: 10.1146/annurev.physchem.50.1.79.

Gudkov, S. V, Burmistrov, D.E., Serov, D.A., Rebezov, M.B., Semenova, A.A. and Lisitsyn, A.B. (2021), “A Mini Review of Antibacterial Properties of ZnO Nanoparticles”, *Frontiers in Physics*, Vol. 9.

Guo, L., Ji, Y.L., Xu, H., Simon, P. and Wu, Z. (2002), “Regularly shaped, single-crystalline ZnO nanorods with wurtzite structure”, *Journal of the American Chemical Society*, ACS Publications, Vol. 124 No. 50, pp. 14864–14865.

Ha, P.T., Lindemann, S.R., Shi, L., Dohnalkova, A.C., Fredrickson, J.K., Madigan, M.T. and Beyenal, H. (2017), “Syntrophic anaerobic photosynthesis via direct interspecies electron transfer”, *Nature Communications*, Nature Publishing Group, Vol. 8, pp. 1–7, doi: 10.1038/ncomms13924.

Hamann, D.R., Schlüter, M. and Chiang, C. (1979), "Norm-Conserving Pseudopotentials", *Physical Review Letters*, American Physical Society, Vol. 43 No. 20, pp. 1494–1497, doi: 10.1103/PhysRevLett.43.1494.

Hanwell, M.D., Curtis, D.E., Lonie, D.C., Vandermeersch, T., Zurek, E. and Hutchison, G.R. (2012), "Avogadro: an advanced semantic chemical editor, visualization, and analysis platform", *Journal of Cheminformatics*, Vol. 4 No. 1, p. 17, doi: 10.1186/1758-2946-4-17.

He, L., Liu, F., Hautier, G., Oliveira, M.J.T., Marques, M.A.L., Vila, F.D., Rehr, J.J., *et al.* (2014), "Accuracy of generalized gradient approximation functionals for density-functional perturbation theory calculations", *Physical Review B*, APS, Vol. 89 No. 6, p. 064305.

Hernandez, M.E. and Newman, D.K. (2001), "Extracellular electron transfer", *Cellular and Molecular Life Sciences*, Vol. 58 No. 11, pp. 1562–1571, doi: 10.1007/PL00000796.

Heyd, J., Scuseria, G.E. and Ernzerhof, M. (2003), "Hybrid functionals based on a screened Coulomb potential", *The Journal of Chemical Physics*, American Institute of Physics, Vol. 118 No. 18, pp. 8207–8215.

Hobbie, S.N., Li, X., Basen, M., Stingl, U. and Brune, A. (2012a), "Humic substance-mediated Fe(III) reduction by a fermenting Bacillus strain from the alkaline gut of a humus-feeding scarab beetle larva", *Systematic and Applied Microbiology*, Elsevier GmbH., Vol. 35 No. 4, pp. 226–232, doi: 10.1016/j.syapm.2012.03.003.

Hobbie, S.N., Li, X., Basen, M., Stingl, U. and Brune, A. (2012b), "Humic substance-mediated Fe(III) reduction by a fermenting Bacillus strain from the alkaline gut of a humus-feeding scarab beetle larva", *Systematic and Applied Microbiology*, Elsevier GmbH., Vol. 35 No. 4, pp. 226–232, doi: 10.1016/j.syapm.2012.03.003.

Hoz, S. (1982), "The a Effect: On the Origin of Transition-State Stabilization", *Journal of Organic Chemistry*, Vol. V No. 11, pp. 3545–3547.

Hybertsen, M.S. and Louie, S.G. (1985), "First-Principles Theory of Quasiparticles: Calculation of Band Gaps in Semiconductors and Insulators", *Physical Review Letters*, American Physical Society, Vol. 55 No. 13, pp. 1418–1421, doi: 10.1103/PhysRevLett.55.1418.

Hybertsen, M.S. and Louie, S.G. (1986), "Electron correlation in semiconductors and insulators: Band gaps and quasiparticle energies", *Physical Review B*, American Physical Society, Vol. 34 No. 8, pp. 5390–5413, doi: 10.1103/PhysRevB.34.5390.

Ishihara, A., Imai, H. and Ota, K.I. (2014), "Transition Metal Oxides, Carbides, Nitrides, Oxynitrides, and Carbonitrides for O2 Reduction Reaction Electrocatalysts for Acid PEM Fuel Cells", *Non-Noble Metal Fuel Cell Catalysts*, Vol. 9783527333, pp. 183–204, doi: 10.1002/9783527664900.ch5.

Jain, S., Jain, S., Wolf, I.T., Lee, J. and Tong, Y.W. (2015), "A comprehensive review on operating parameters and different pretreatment methodologies for anaerobic digestion of municipal solid waste", *Renewable and Sustainable Energy Reviews*, Elsevier Ltd, Vol. 52, pp. 142–154, doi: 10.1016/j.rser.2015.07.091.

Karzel, H., Potzel, W., Köfferlein, M., Schiessl, W., Steiner, M., Hiller, U., Kalvius, G.M., *et al.* (1996), "Lattice dynamics and hyperfine interactions in ZnO and ZnSe at high external pressures", *Physical Review B*, APS, Vol. 53 No. 17, p. 11425.

Kataky, R. and Knowles, E. (2018), "Biofilm formation on abiotic surfaces and their redox activity", *Current Opinion in Electrochemistry*, Elsevier B.V., Vol. 12, pp. 121–128, doi: 10.1016/j.coelec.2018.07.007.

Kohn, W. and Sham, L.J. (1965), "Self-consistent equations including exchange and correlation effects", *Physical Review*, APS, Vol. 140 No. 4A, p. A1133.

Kokalj, A. (1999), "XCrySDen--a new program for displaying crystalline structures and electron densities.", *Journal of Molecular Graphics & Modelling*, United States, Vol. 17 No. 3–4, pp. 176-179,215-216, doi: 10.1016/s1093-3263(99)00028-5.

Kramer, P. (2008), "A review of the time-dependent variational principle", *Journal of Physics: Conference Series*, Vol. 99 No. 1, doi: 10.1088/1742-6596/99/1/012009.

Kraus, S.J. and Glassman, L.H. (1974), " Scanning Electron Microscope Study of Neisseria gonorrhoeae ", *Applied Microbiology*, Vol. 27 No. 3, pp. 584–592, doi: 10.1128/am.27.3.584-592.1974.

Lee, C., Yang, W. and Parr, R.G. (1988), "Development of the Colle-Salvetti correlation-energy formula into a functional of the electron density", *Physical Review B*, Vol. 37 No. 2, pp. 785–789, doi: 10.1103/PhysRevB.37.785.

Lee, S.H., Kang, H.J., Lim, T.G. and Park, H.D. (2020), "Magnetite and granular activated carbon improve methanogenesis via different metabolic routes", *Fuel*, Elsevier, Vol. 281 No. June, p. 118768, doi: 10.1016/j.fuel.2020.118768.

Lei, Y., Sun, D., Dang, Y., Chen, H., Zhao, Z., Zhang, Y. and Holmes, D.E. (2016), "Stimulation of methanogenesis in anaerobic digesters treating leachate from a municipal solid waste incineration plant with carbon cloth", *Bioresource Technology*, Elsevier Ltd, Vol. 222, pp. 270–276, doi: 10.1016/j.biortech.2016.10.007.

Li, G.R., Song, J., Pan, G.L. and Gao, X.P. (2011), "Highly Pt-like electrocatalytic activity of transition metal nitrides for dye-sensitized solar cells", *Energy and Environmental Science*, Vol. 4 No. 5, pp. 1680–1683, doi: 10.1039/c1ee01105g.

Liang, Y. gan, Li, X. juan, Zhang, J., Zhang, L. gan and Cheng, B. (2017), "Effect of microscale ZVI/magnetite on methane production and bioavailability of heavy metals during anaerobic digestion of diluted pig manure", *Environmental Science and Pollution Research*, Environmental Science and Pollution Research, Vol. 24 No. 13, pp. 12328–12337, doi: 10.1007/s11356-017-8832-9.

Lin, J.Y., Tai, S.Y. and Chou, S.W. (2014), “Bifunctional one-dimensional hierarchical nanostructures composed of cobalt sulfide nanoclusters on carbon nanotubes backbone for dye-sensitized solar cells and supercapacitors”, *Journal of Physical Chemistry C*, Vol. 118 No. 2, pp. 823–830, doi: 10.1021/jp4092688.

Liu, F., Rotaru, A.E., Shrestha, P.M., Malvankar, N.S., Nevin, K.P. and Lovley, D.R. (2012), “Promoting direct interspecies electron transfer with activated carbon”, *Energy and Environmental Science*, Vol. 5 No. 10, pp. 8982–8989, doi: 10.1039/c2ee22459c.

Liu, F., Rotaru, A.E., Shrestha, P.M., Malvankar, N.S., Nevin, K.P. and Lovley, D.R. (2015), “Magnetite compensates for the lack of a pilin-associated c-type cytochrome in extracellular electron exchange”, *Environmental Microbiology*, Vol. 17 No. 3, pp. 648–655, doi: 10.1111/1462-2920.12485.

Liu, T., Cai, S., Zhao, G., Gao, Z., Liu, S., Li, H., Chen, L., *et al.* (2021), “Recycling valuable cobalt from spent lithium ion batteries for controllably designing a novel sea-urchin-like cobalt nitride-graphene hybrid catalyst: Towards efficient overall water splitting”, *Journal of Energy Chemistry*, Science Press, Vol. 62, pp. 440–450, doi: 10.1016/j.jechem.2021.03.052.

Luna-delRisco, M., Orupõld, K. and Dubourguier, H.C. (2011a), “Particle-size effect of CuO and ZnO on biogas and methane production during anaerobic digestion”, *Journal of Hazardous Materials*, Elsevier B.V., Vol. 189 No. 1–2, pp. 603–608, doi: 10.1016/j.jhazmat.2011.02.085.

Luna-delRisco, M., Orupõld, K. and Dubourguier, H.C. (2011b), “Particle-size effect of CuO and ZnO on biogas and methane production during anaerobic digestion”, *Journal of Hazardous Materials*, Vol. 189 No. 1–2, pp. 603–608, doi: 10.1016/j.jhazmat.2011.02.085.

Luna-delRisco, M., Orupõld, K. and Dubourguier, H.-C. (2011c), “Particle-size effect of CuO and ZnO on biogas and methane production during anaerobic digestion”, *Journal of Hazardous Materials*, Elsevier, Vol. 189 No. 1–2, pp. 603–608.

Maeder, D.L., Anderson, I., Brettin, T.S., Bruce, D.C., Gilna, P., Han, C.S., Lapidus, A., *et al.* (2006), “The Methanosarcina barkeri genome: Comparative analysis with Methanosarcina acetivorans and Methanosarcina mazei reveals extensive rearrangement within methanosarcinal genomes”, *Journal of Bacteriology*, Vol. 188 No. 22, pp. 7922–7931, doi: 10.1128/JB.00810-06.

Mahdy, A., Bi, S., Song, Y., Qiao, W. and Dong, R. (2020), “Overcome inhibition of anaerobic digestion of chicken manure under ammonia-stressed condition by lowering the organic loading rate”, *Bioresource Technology Reports*, Elsevier, Vol. 9 No. December 2019, p. 100359, doi: 10.1016/j.biteb.2019.100359.

Maliničová, L., Piknová, M., Pristaš, P. and Javorský, P. (2010), “Peptidoglycan hydrolases as novel tool for anti-enterococcal therapy”, *Current Research, Technology and Education Topics in Applied Microbiology and Microbial Biotechnology. The Formatex*

Microbiology Book Series, Formatex Research Center Badajoz, Spain, Vol. 1, pp. 463–472.

Manyi-Loh, C.E., Mamphweli, S.N., Meyer, E.L., Okoh, A.I., Makaka, G. and Simon, M. (2013), "Microbial anaerobic digestion (bio-digesters) as an approach to the decontamination of animal wastes in pollution control and the generation of renewable energy", *International Journal of Environmental Research and Public Health*, Vol. 10 No. 9, pp. 4390–4417, doi: 10.3390/ijerph10094390.

Martinez, C.M., Alvarez, L.H., Celis, L.B. and Cervantes, F.J. (2013), "Humus-reducing microorganisms and their valuable contribution in environmental processes", *Applied Microbiology and Biotechnology*, Vol. 97 No. 24, pp. 10293–10308, doi: 10.1007/s00253-013-5350-7.

Martins, G., Salvador, A.F., Pereira, L. and Alves, M.M. (2018), "Methane Production and Conductive Materials: A Critical Review", *Environmental Science and Technology*, Vol. 52 No. 18, pp. 10241–10253, doi: 10.1021/acs.est.8b01913.

Meghana, S., Kabra, P., Chakraborty, S. and Padmavathy, N. (2015), "Understanding the pathway of antibacterial activity of copper oxide nanoparticles", *RSC Adv.*, The Royal Society of Chemistry, Vol. 5 No. 16, pp. 12293–12299, doi: 10.1039/C4RA12163E.

Momma, K. and Izumi, F. (2008), " VESTA: a three-dimensional visualization system for electronic and structural analysis", *Journal of Applied Crystallography*, Vol. 41 No. 3, pp. 653–658, doi: 10.1107/S0021889808012016.

Monkhorst, H.J. and Pack, J.D. (1976), "Special points for Brillouin-zone integrations", *Phys. Rev. B*, American Physical Society, Vol. 13 No. 12, pp. 5188–5192, doi: 10.1103/PhysRevB.13.5188.

Montejo, C., Ramos, P., Costa, C. and Márquez, M.C. (2010), "Analysis of the presence of improper materials in the composting process performed in ten MBT plants", *Bioresource Technology*, Elsevier Ltd, Vol. 101 No. 21, pp. 8267–8272, doi: 10.1016/j.biortech.2010.06.024.

Moroni, E., Kresse, G., Hafner, J. and Furthmüller, J. (1997), "Ultrasoft pseudopotentials applied to magnetic Fe, Co, and Ni: From atoms to solids", *Physical Review B*, Vol. 56 No. 24, pp. 15629–15646, doi: 10.1103/PhysRevB.56.15629.

Morris, M.D. (1991), "Factorial sampling plans for preliminary computational experiments", *Technometrics*, Vol. 33 No. 2, pp. 161–174, doi: 10.1080/00401706.1991.10484804.

Mostefai, A., Berrah, S. and Abid, H. (2018), "Electronics Properties of Monoclinic HfO2", *Journal of Nano-and Electronic Physics*, Sumy State University, Journal of Nano-and Electronic Physics, Vol. 10 No. 6.

Van Mourik, T. (2004), "First-principles quantum chemistry in the life sciences", *Philosophical Transactions of the Royal Society A: Mathematical, Physical and Engineering Sciences*, Vol. 362 No. 1825, pp. 2653–2670, doi: 10.1098/rsta.2004.1469.

Munir, M.T., Mardon, I., Al-Zuhair, S., Shawabkeh, A. and Saqib, N.U. (2019), "Plasma gasification of municipal solid waste for waste-to-value processing", *Renewable and Sustainable Energy Reviews*, Elsevier Ltd, Vol. 116 No. April, p. 109461, doi: 10.1016/j.rser.2019.109461.

Nazerifard, R., Khani, L., Mohammadpourfard, M., Mohammadi-Ivatloo, B. and Akkurt, G.G. (2021), "Design and thermodynamic analysis of a novel methanol, hydrogen, and power trigeneration system based on renewable energy and flue gas carbon dioxide", *Energy Conversion and Management*, Vol. 233 No. February, doi: 10.1016/j.enconman.2021.113922.

Ordejn, P., Drabold, D.A., Martin, R.M. and Grumbach, M.P. (1995), "Linear system-size scaling methods for electronic-structure calculations", *Physical Review B*, Vol. 51 No. 3, pp. 1456–1476, doi: 10.1103/PhysRevB.51.1456.

Palmer, D.J. and Dickens, P.G. (1979), "Tungsten dioxide: structure refinement by powder neutron diffraction", *Acta Crystallographica Section B: Structural Crystallography and Crystal Chemistry*, International Union of Crystallography, Vol. 35 No. 9, pp. 2199–2201.

Perdew, J.P., Burke, K., Ernzerhof, M., of Physics, D. and Quantum Theory Group Tulane University, N.O.L. 70118 J. (1996), "Generalized Gradient Approximation Made Simple", *Physical Review Letters*, Vol. 77 No. 3, pp. 3865–3868, doi: 10.1103/PhysRevLett.77.3865.

Qiu, L., Deng, Y.F., Wang, F., Davaritouchaee, M. and Yao, Y.Q. (2019), "A review on biochar-mediated anaerobic digestion with enhanced methane recovery", *Renewable and Sustainable Energy Reviews*, Elsevier Ltd, Vol. 115 No. April, p. 109373, doi: 10.1016/j.rser.2019.109373.

Ray, S.C. (2001), "Preparation of copper oxide thin film by the sol–gel-like dip technique and study of their structural and optical properties", *Solar Energy Materials and Solar Cells*, Elsevier, Vol. 68 No. 3–4, pp. 307–312.

Reginatto, M. (1998), "Derivation of the equations of nonrelativistic quantum mechanics using the principle of minimum Fisher information", *Physical Review A - Atomic, Molecular, and Optical Physics*, Vol. 58 No. 3, pp. 1775–1778, doi: 10.1103/PhysRevA.58.1775.

Reines, F. and Sobel, H.W. (1974), "Test of the pauli exclusion principle for atomic electrons", *Physical Review Letters*, Vol. 32 No. 17, p. 954, doi: 10.1103/PhysRevLett.32.954.

Ren, N.Q., Chua, H., Chan, S.Y., Tsang, Y.F., Wang, Y.J. and Sin, N. (2007), "Assessing optimal fermentation type for bio-hydrogen production in continuous-flow acidogenic reactors", *Bioresource Technology*, Vol. 98 No. 9, pp. 1774–1780, doi: 10.1016/j.biortech.2006.07.026.

Rotaru, A.E., Shrestha, P.M., Liu, F., Markovaite, B., Chen, S., Nevin, K.P. and Lovley, D.R. (2014), "Direct interspecies electron transfer between Geobacter metallireducens and Methanosarcina barkeri", *Applied and Environmental Microbiology*, Vol. 80 No. 15, pp. 4599–4605, doi: 10.1128/AEM.00895-14.

Rotaru, A.E., Shrestha, P.M., Liu, F., Shrestha, M., Shrestha, D., Embree, M., Zengler, K., *et al.* (2014), "A new model for electron flow during anaerobic digestion: Direct interspecies electron transfer to Methanosaeta for the reduction of carbon dioxide to methane", *Energy and Environmental Science*, Vol. 7 No. 1, pp. 408–415, doi: 10.1039/c3ee42189a.

Sales, M.G., Jaszewski, S.T., Fields, S.S., Litwin, P.M., Ihlefeld, J.F. and McDonnell, S.J. (2021), "Thermal stability of hafnium zirconium oxide on transition metal dichalcogenides", *Applied Surface Science*, Elsevier B.V., Vol. 546 No. August 2020, p. 149058, doi: 10.1016/j.apsusc.2021.149058.

Salotto, A.W. and Burnelle, L. (1970), "Investigations on the unrestricted hartree-fock method as a tool for computing potential surfaces", *The Journal of Chemical Physics*, Vol. 52 No. 6, pp. 2936–2945, doi: 10.1063/1.1673420.

Sasaki, K., Tsuge, Y., Sasaki, D. and Kondo, A. (2014), "Increase in lactate yield by growing Corynebacterium glutamicum in a bioelectrochemical reactor", *Journal of Bioscience and Bioengineering*, Elsevier, Vol. 117 No. 5, pp. 598–601.

Shen, F., Jiang, W., Qian, G., Chen, W., Zhang, H., Luo, L. and Yin, S. (2020), "Strongly coupled carbon encapsulated Ni-WO2 hybrids as efficient catalysts for water-to-hydrogen conversion via urea electro-oxidation", *Journal of Power Sources*, Elsevier B.V., Vol. 458 No. January, p. 228014, doi: 10.1016/j.jpowsour.2020.228014.

Shofner, G.A., Campbell, A.J., Danielson, L.R., Righter, K., Fischer, R.A., Wang, Y. and Prakapenka, V. (2016), "The W-WO2 oxygen fugacity buffer (WWO) at high pressure and temperature: Implications for f O2 buffering and metal-silicate partitioning", *American Mineralogist*, Mineralogical Society of America, Vol. 101 No. 1, pp. 211–221.

Silva, L.J. de V.B. da, Santos, I.F.S. dos, Mensah, J.H.R., Gonçalves, A.T.T. and Barros, R.M. (2020), "Incineration of municipal solid waste in Brazil: An analysis of the economically viable energy potential", *Renewable Energy*, Vol. 149, pp. 1386–1394, doi: 10.1016/j.renene.2019.10.134.

Singh, O. V. and Harvey, S.P. (2010), *Sustainable Biotechnology: Sources of Renewable Energy*, *Sustainable Biotechnology: Sources of Renewable Energy*, doi: 10.1007/978-90-481-3295-9.

Singh, R.P., Tyagi, V. V., Allen, T., Ibrahim, M.H. and Kothari, R. (2011), "An overview for exploring the possibilities of energy generation from municipal solid waste (MSW) in Indian scenario", *Renewable and Sustainable Energy Reviews*, Elsevier Ltd, Vol. 15 No. 9, pp. 4797–4808, doi: 10.1016/j.rser.2011.07.071.

Sumpter, B.G., Tuzun, R.E. and Noid, D.W. (1998), "Computational Simulation and Modeling of Molecular-Based Materials", *Modern Methods for Multidimensional Dynamics Computations in Chemistry*, pp. 401–471, doi: 10.1142/9789812812162_0012.

Tahir, D. and Tougaard, S. (2012), "Electronic and optical properties of Cu, CuO and Cu2O studied by electron spectroscopy", *Journal of Physics: Condensed Matter*, IOP Publishing, Vol. 24 No. 17, p. 175002.

Talmi, I. (1962), "Effective interactions and coupling schemes in nuclei", *Reviews of Modern Physics*, Vol. 534 No. 4, pp. 704–723, doi: 10.1016/0375-9474(94)90298-4.

Tapavicza, E., Tavernelli, I. and Rothlisberger, U. (2007), "Trajectory surface hopping within linear response time-dependent density-functional theory", *Physical Review Letters*, Vol. 98 No. 2, pp. 1–4, doi: 10.1103/PhysRevLett.98.023001.

Tenodi, S., Krčmar, D., Agbaba, J., Zrnić, K., Radenović, M., Ubavin, D. and Dalmacija, B. (2020), "Assessment of the environmental impact of sanitary and unsanitary parts of a municipal solid waste landfill", *Journal of Environmental Management*, Vol. 258 No. November 2019, doi: 10.1016/j.jenvman.2019.110019.

Tetteh, E.K. and Rathilal, S. (2021), "Application of biomagnetic nanoparticles for biostimulation of biogas production from wastewater treatment", *Materials Today: Proceedings*, Elsevier, Vol. 45, pp. 5214–5220.

Thirumurthy, M.A., Hitchcock, A., Cereda, A., Liu, J., Chavez, M.S., Doss, B.L., Ros, R., *et al.* (2020), "Type IV Pili-Independent Photocurrent Production by the Cyanobacterium Synechocystis sp. PCC 6803", *Frontiers in Microbiology*, Vol. 11 No. June, pp. 1–11, doi: 10.3389/fmicb.2020.01344.

Touhami, A., Jericho, M.H., Boyd, J.M. and Beveridge, T.J. (2006), "Nanoscale characterization and determination of adhesion forces of Pseudomonas aeruginosa pili by using atomic force microscopy", *Journal of Bacteriology*, Vol. 188 No. 2, pp. 370–377, doi: 10.1128/JB.188.2.370-377.2006.

Toyoda, S., Okabayashi, J., Kumigashira, H., Oshima, M., Ono, K., Niwa, M., Usuda, K., *et al.* (2004), "Chemistry and band offsets of HfO2 thin films on Si revealed by photoelectron spectroscopy and x-ray absorption spectroscopy", *Journal of Electron Spectroscopy and Related Phenomena*, Vol. 137–140, pp. 141–144, doi: https://doi.org/10.1016/j.elspec.2004.02.083.

Troullier, N. and Martins, J.L. (1991), "Efficient pseudopotentials for plane-wave calculations. II. Operators for fast iterative diagonalization", *Physical Review B*, Vol. 43 No. 11, pp. 8861–8869, doi: 10.1103/PhysRevB.43.8861.

VanGessel, F., Peng, J. and Chung, P.W. (2018), "A review of computational phononics: the bulk, interfaces, and surfaces", *Journal of Materials Science*, Springer US, Vol. 53 No. 8, pp. 5641–5683, doi: 10.1007/s10853-017-1728-8.

Velghe, I., Carleer, R., Yperman, J. and Schreurs, S. (2011a), “Study of the pyrolysis of municipal solid waste for the production of valuable products”, *Journal of Analytical and Applied Pyrolysis*, Elsevier B.V., Vol. 92 No. 2, pp. 366–375, doi: 10.1016/j.jaap.2011.07.011.

Velghe, I., Carleer, R., Yperman, J. and Schreurs, S. (2011b), “Study of the pyrolysis of municipal solid waste for the production of valuable products”, *Journal of Analytical and Applied Pyrolysis*, Elsevier B.V., Vol. 92 No. 2, pp. 366–375, doi: 10.1016/j.jaap.2011.07.011.

Wang, T., Zhu, G., Kuang, B., Jia, J., Liu, C., Cai, G. and Li, C. (2021), “Novel insights into the anaerobic digestion of propionate via Syntrophobacter fumaroxidans and Geobacter sulfurreducens: Process and mechanism”, *Water Research*, Elsevier Ltd, Vol. 200, p. 117270, doi: 10.1016/j.watres.2021.117270.

Wang, W. and Lee, D.J. (2021), “Direct interspecies electron transfer mechanism in enhanced methanogenesis: A mini-review”, *Bioresource Technology*, Elsevier Ltd, Vol. 330 No. March, doi: 10.1016/j.biortech.2021.124980.

Wang, Z., Wang, T., Si, B., Watson, J. and Zhang, Y. (2021), “Accelerating anaerobic digestion for methane production: Potential role of direct interspecies electron transfer”, *Renewable and Sustainable Energy Reviews*, Elsevier Ltd, Vol. 145 No. April, p. 111069, doi: 10.1016/j.rser.2021.111069.

Wells, A.F. (1984), “The lanthanides and actinides”, *Structural Inorganic Chemistry. 5. Ed*.

Williams, T. and Kelley, C. (1998), *GNUplot: An Interactive Plotting Program*.

Wu, C.Y., Zhuang, L., Zhou, S.G., Li, F.B. and He, J. (2011), “Corynebacterium humireducens sp. nov., an alkaliphilic, humic acid-reducing bacterium isolated from a microbial fuel cell”, *International Journal of Systematic and Evolutionary Microbiology*, Vol. 61 No. 4, pp. 882–887, doi: 10.1099/ijs.0.020909-0.

Xia, X., Zhang, J., Song, T. and Lu, Y. (2019), “Stimulation of Smithella-dominating propionate oxidation in a sediment enrichment by magnetite and carbon nanotubes”, *Environmental Microbiology Reports*, Vol. 11 No. 2, pp. 236–248, doi: 10.1111/1758-2229.12737.

Yun, S., Xing, T., Han, F., Shi, J., Wang, Z., Fan, Q. and Xu, H. (2021a), “Enhanced direct interspecies electron transfer with transition metal oxide accelerants in anaerobic digestion”, *Bioresource Technology*, Elsevier Ltd, Vol. 320 No. PA, p. 124294, doi: 10.1016/j.biortech.2020.124294.

Yun, S., Xing, T., Han, F., Shi, J., Wang, Z., Fan, Q. and Xu, H. (2021b), “Enhanced direct interspecies electron transfer with transition metal oxide accelerants in anaerobic digestion”, *Bioresource Technology*, Elsevier, Vol. 320, p. 124294.

Zefirov, Y. V. (2001), “Van der Waals Radii and Current Problems of Their Application”, *Russian Journal of Inorganic Chemistry*, Vol. 46 No. 4, pp. 568–572.

Zhang, M. and Zang, L. (2019), “A review of interspecies electron transfer in anaerobic digestion”, *IOP Conference Series: Earth and Environmental Science*, Vol. 310 No. 4, pp. 15–20, doi: 10.1088/1755-1315/310/4/042026.

Zhao, Y., Schultz, N.E. and Truhlar, D.G. (2005), “Exchange-correlation functional with broad accuracy for metallic and nonmetallic compounds, kinetics, and noncovalent interactions”, *Journal of Chemical Physics*, Vol. 123 No. 16, doi: 10.1063/1.2126975.

Zheng, H., Wang, Y., Feng, X., Li, S., Leong, Y.K. and Chang, J.S. (2021), “Renewable biohydrogen production from straw biomass – Recent advances in pretreatment/hydrolysis technologies and future development”, *International Journal of Hydrogen Energy*, Elsevier Ltd, No. xxxx, doi: 10.1016/j.ijhydene.2021.10.020.